



저작자표시-비영리-변경금지 2.0 대한민국

이용자는 아래의 조건을 따르는 경우에 한하여 자유롭게

- 이 저작물을 복제, 배포, 전송, 전시, 공연 및 방송할 수 있습니다.

다음과 같은 조건을 따라야 합니다:



저작자표시. 귀하는 원저작자를 표시하여야 합니다.



비영리. 귀하는 이 저작물을 영리 목적으로 이용할 수 없습니다.



변경금지. 귀하는 이 저작물을 개작, 변형 또는 가공할 수 없습니다.

- 귀하는, 이 저작물의 재이용이나 배포의 경우, 이 저작물에 적용된 이용허락조건을 명확하게 나타내어야 합니다.
- 저작권자로부터 별도의 허가를 받으면 이러한 조건들은 적용되지 않습니다.

저작권법에 따른 이용자의 권리는 위의 내용에 의하여 영향을 받지 않습니다.

이것은 [이용허락규약\(Legal Code\)](#)을 이해하기 쉽게 요약한 것입니다.

[Disclaimer](#)

이학박사 학위논문

전기화학의 다면적 잠재력에 대한 탐구: 푸리에 변환
전기화학 임피던스 분광법과 이온트로닉스

Excavating the Puissance of Electrochemistry:
Fourier Transform Electrochemical Impedance
Spectroscopy and Iontronics

2021 년 2 월

서울대학교 대학원

화학부 전기분석화학 전공

한 석 희

A Ph. D. Dissertation entitled

Excavating the Puissance of Electrochemistry:
Fourier Transform Electrochemical Impedance
Spectroscopy and Iontronics

Seok Hee Han

February 2021

Supervisor: Professor Taek Dong Chung

Major: Electroanalytical chemistry

Department of Chemistry

Graduate School of

Seoul National University

Excavating the Puissance of Electrochemistry: Fourier Transform Electrochemical Impedance Spectroscopy and Iontronics

전기화학의 다면적 잠재력에 대한 탐구: 푸리에 변환 전
기화학 임피던스 분광법과 이온트로닉스

지도교수 정택동

이 논문을 이학박사 학위논문으로 제출함.

2021년 2월


서울대학교 대학원


화학부 전기분석화학 전공


한석희

한석희의 박사학위논문을 인준함.


2021년 2월

위원장 임종우  (인)

부위원장 정택동  (인)

위원 김지환  (인)

위원 선정윤  (인)

위원 장병용  (인)

Abstract

As one of the branch of chemistry, electrochemistry not only deals with the chemical change caused by the charge transfer between electrode and electroactive reactants in the solution, but also any other form of changes (e.g. physical, electrical, structural) that affect the system of interest in electrochemical manner. This is why electrochemistry encompasses a huge variety of phenomena such as electroanalytical sensors, batteries, fuel cells, corrosion, electroplating, and even many others that may not look like very chemical. Discovering the extensiveness of applications and potentials related to electrochemistry, this dissertation reports two very different researches, both of which belong to electrochemistry although the second one might be seemingly distant from the very field. In Part 1, we present the utilization of Fourier transform electrochemical impedance spectroscopy (FT-EIS) for in situ, real-time analysis of the system during the chemical process. In Part 2, we report on a noticeable development of iontronic devices based on charged hydrogels toward the futuristic, biomimetic ion-based information processing platform.

Part 1: Implementation of Fourier Transform Electrochemical Impedance Spectroscopy (FT-EIS) for Real-time Analysis

As a novel approach to the in situ real-time investigation of electrochemical systems, we implemented the step-excitation Fourier transform electrochemical impedance spectroscopy (FT-EIS). For demonstration, we chose the ITO film electrode being chemically etched under $\text{FeCl}_3\text{-HCl}$ -based etchant, which is one of

the most frequently used etchants in lithographic processes. The equivalent circuit parameters (e.g. R_{ct} , C_{dl}) continuously obtained by the FT-EIS measurements during the entire etching process showed an electrode activation at the initial period as well as the completion of etching. The FT-EIS results were further validated by cyclic voltammograms and impedance measurements of partially etched ITO films using ferri- and ferrocyanide solution in combination with FESEM imaging, EDS, XRD analyses, and COMSOL simulation. We also demonstrated that this technique can be further utilized to obtain intact interdigitated array (IDA) electrodes in a reproducible manner, which is generally considered to be quite tricky due to delicacy of the pattern. Given that the FT-EIS allows for instantaneous snapshots of the electrode at every moment, this work may hold promise for in situ real-time examination of structural, electrokinetic, or mass transfer-related information of electrochemical systems undergoing constantly changing, transient processes not to mention etching, which would be impossible with conventional electroanalytical techniques.

Part 2: Development of New Iontronic Platform for Biomimetic Ion-based Information Processing

Iontronics, which was coined from ‘ion’ and ‘electronics’, ultimately aims at actualizing ion-based information processing system just like the biological system by employing aqueous ionic circuits with components that control the flow of ions. Nevertheless, conventional iontronic devices including ionic diodes, capacitors,

transistors and logic circuits have had discrepancies from biological units or have lacked versatilities in terms of substrate material. Herein, we report two major steps forward in iontronic devices conforming to its essential goals. First, we fabricated ionic circuits powered by reverse electro dialysis (RED) for the first time without employing any electronic components just as neurons, which participate in signal transmission with its own power generated by itself. The RED-driven polyelectrolyte diode successfully shows rectification behavior which is verified by monitoring dynamic ion distribution through fluorescence in real-time. We can also turn on and off the voltage applied to the circuit, and apply an arbitrary voltage by precisely manipulating the pressure imposed to an elastic connection tube filled with electrolyte. Furthermore, this new concept containing ionic power source advances to a more sophisticated ionic OR logic gate. The proposed system paves the way to develop not only passive iontronic devices (e.g. resistor, diode), but active ones requiring a source of energy, particularly such as a neuron-like information processor powered by fully ionic systems, and thereby aqueous computers. Secondly, we report a new method for fabricating the hydrogel-based ionic circuit on polydimethylsiloxane (PDMS) microchip. We employed a long duration of UV/ozone oxidation, proper surface functionalizations of PDMS substrate together with a novel PDMS-PDMS bonding technique using thiol-epoxy click reaction in order to photopolymerize the hydrogel that can be robustly attached to the PDMS microchannel surface for the eventual operation in electrolyte as an ionic circuit. The ionic diode constructed on PDMS microchip showed a fine rectification ratio even under tensile stress as well as a stability for long-term storage. We also materialized

an ionic regulator on PDMS microchip based on mechanical switch, which allowed us to embody an iontronic signal transmission mimicking excitatory and inhibitory synapses. As a biocompatible iontronic platform, the hydrogel-based iontronics on PDMS microchip not only diversifies many related fields requiring aqueous, ionic, elastic and stretchable system, but also renders new opportunities for bioinspired applications.

Keywords: Fourier transform electrochemical impedance spectroscopy (FT-EIS), Indium tin oxide (ITO), Chemical Etching, Iontronics, Polyelectrolyte gel (hydrogel), Ionic circuits, Reverse electrodialysis (RED), Biomimetic information processing

Student number: 2014-22416

Table of contents

Abstract	i
Table of contents	v
List of Schemes	viii
List of Figures.....	x
List of Tables	xxiv
Part 1. Implementation of Fourier Transform Electrochemical Impedance Spectroscopy (FT-EIS) for Real-time Analysis	1
1.1 Introduction.....	1
1.2. Experimental Section.....	5
1.2.1. Materials.....	5
1.2.2. Fabrication of PR-coated ITO micropatterns.....	5
1.2.3. FT-EIS measurements and fitting of the impedance data	6
1.2.4. Electrochemical measurements.....	7
1.2.5. COMSOL simulation	7
1.2.6. Investigation of near-surface characteristics of etched ITO samples	8
1.3. Results and Discussion	9
1.3.1. FT-EIS measurement of the ITO sample being etched.....	9

1.3.2. The initial period of etching	16
1.3.3. Monitoring termination of etching process via FT-EIS analysis...	22
1.3.4. Validation of FT-EIS results using conventional electroanalytical techniques	30
1.3.5. Electrochemical monitoring of ITO etching process using conventional electroanalytical techniques.....	34
1.4. Conclusion	42
1.5. References.....	45
Part 2. Development of New Iontronic Platform for Biomimetic Ion-based Information Processing	49
2.1 Introduction.....	49
2.2. Experimental Section.....	53
2.2.1. Materials.....	53
2.2.2. Preparation of RED stack	53
2.2.3. Microchip fabrication.....	54
2.2.4. Fabrication of polyelectrolyte ionic diode on microchip.....	55
2.2.5. Connection of RED to the ionic circuit	56
2.2.6. Voltage and current measurements in RED-powered ionic circuit	56
2.2.7. Optical measurement.....	58
2.2.8. PDMS microchip fabrication.....	58

2.2.9. Photopolymerization of hydrogels on PDMS microchip.....	60
2.2.10. Hydrogel stability test on two-dimensional surface under electrolyte solution	60
2.2.11. Tensile test of PDMS microfluidic ionic diode (PMID).....	61
2.2.12. Electrical characterization of PDMS microfluidic ionic circuits	61
2.3. Results and Discussion	63
2.3.1. Electrical characterization of RED.....	63
2.3.2. Ionic diode powered by RED	63
2.3.3. Voltage switching and regulation upon ionic circuit	68
2.3.4. Ionic OR gate driven by RED.....	72
2.3.5. Preparation of PDMS microchip for subsequent hydrogel formation	74
2.3.6. Validation of robustness of hydrogel-PDMS interface in aqueous environment	81
2.3.7. Flexible and stretchable ionic diode on PDMS microchip	90
2.3.8. PDMS microfluidic ionic regulator (PMIR) based on mechanical switch.....	96
2.4. Conclusion	103
2.5. References.....	106
국문초록	110

List of Schemes

Scheme 1-1. Schematic illustration of FT-EIS analysis of 5×5 ITO microdisk patterns coated with AZ4620 photoresist under chemical etching process in 3 M FeCl_3 , 1 M HCl etchant at 47 °C. The distance between two nearest microdisks was 200 μm . The PR thickness was about 5 μm . The diameter of teflon cell hole through which the ITO pattern was exposed to etchant was 6 mm.....9

Scheme 2-1. Step-by-step reaction scheme for preparation of PDMS microchip. (A) Initial pristine PDMS substrates, (B) substrates after hydrophilic activation using 3 h of UV/ozone oxidation and (C) surface silanizations using MPTMS and GPTMS for the top and the bottom substrates, respectively. (D) Robustly bonded PDMS microchip after 2 days of thiol-epoxy click reaction mediated by mechanical pressure. (Inset: Chemical structure of PDMS-PDMS interface and channel surface marked with dashed circle) (E) Final PDMS microchip; microchannel surface is entirely modified with thiol functional groups after 2 h of base-catalyzed thiol-epoxy reaction with injection of methanol solution containing 1,2-ethanedithiol (EDT) and 1,8-diazabicyclo[5.4.0]undec-7-ene (DBU). (Inset: Chemical structure of the inner microchannel surfaces)

Chemical structures of (F) pDADMAC-anchored, and (G) pSS-
anchored microchannel surfaces. 79

List of Figures

Fig. 1-1. (A) The square wave signal used in the FT-EIS measurement in Scheme 1-1. (B) Cyclic voltammograms measured immediately after the immersion of ITO macroelectrode (0.5 mm diam., red solid line) and the ITO microdisk array electrode depicted in Scheme 1-1 (black solid line) into the etchant. The scan rate was 0.1 V/s. 11

Fig. 1-2. (A) Accumulated Nyquist plots obtained from the FT-EIS measurement during the etching process in 3 M FeCl₃, 1 M HCl etchant at 47 °C. The EIS frequency range was 50 kHz ~ 1 Hz with 2 s of time resolution. (B) Equivalent circuit used for fitting of the impedance data shown in (A). R_s indicates solution resistance, C_{dl} double layer capacitance, R_{ct} charge transfer resistance, and $W_{inf,sph}$ Warburg element of semi-infinite spherical diffusion. (C) Temporal change of the fitted R_{ct} , C_{dl} parameters, and (D) $R_{ct}C_{dl}$ value. (E, F) Magnified versions of (C, D) in the time range of 0 to 4 min. The inset shows the $R_{ct}C_{dl}$ value change during the initial 1 min. 12

Fig. 1-3. Model geometries of the ITO microdisk electrode for COMSOL simulation for one-electron transfer reaction, $Ox + e \leftrightarrow Red$, with 2D axisymmetric configuration (A) when etching is still in process, and (B) when etching is finished. Red solid line indicates the ITO electrode surface. The 5 μ m-wall stands for the PR insulation layer.

The scale of the length might be different from the real dimension. Concentration profiles of Ox species at E_{eq} ($= 0$ V) on cathodic scan when $C_{Ox}^* = C_{Red}^* = 10$ mM (C) for geometry of (A), and (D) for geometry of (B). ($k^0 = 2.37 \times 10^{-6}$ m/s, $C_{dl} = 11.21 \mu\text{F}/\text{cm}^2$, $\alpha = 0.5$, $D_{Ox} = 7.2 \times 10^{-10}$ m²/s, $D_{Red} = 6.7 \times 10^{-10}$ m²/s, Scan rate = 50 mV/s)..... 13

Fig. 1-4. (A) Nyquist plot of the ITO microdisk under 3 M FeCl₃, 1 M HCl etchant at 47 °C obtained from FT-EIS measurement during the etching process ($t = 1$ min, frequency range = 50 kHz ~ 1Hz). (B) Nyquist plots obtained from COMSOL simulation under the geometry of Fig. 1-3A at E_{eq} . Red symbol : $C_{Ox}^* = 20$ mM, $C_{Red}^* = 0$ mM, Black symbol : $C_{Ox}^* = C_{Red}^* = 10$ mM. (C) Cyclic voltammograms and (D) Nyquist plots obtained from COMSOL simulation with varying PR thickness under the geometry of Fig. 1-3A. Vertical blue dashed line at $E = 0$ V indicates E_{eq} in (C). (scan rate = 50 mV/s, frequency range = 100 kHz ~ 1 Hz) The same electrochemical parameters (k^0 , C_{dl} , α , D_{Ox} , D_{Red}) were used as in Fig. 1-3. 16

Fig. 1-5. Field emission scanning electron microscopy (FESEM) images of partially etched ITO microdisk array samples at several time points. The images represent the center area of a microdisk marked with yellow dashed rectangle area at (A) 0 min, (B) 1 min, (C) 2 min, (D) 3 min, and (E) the beginning, (F) the midpoint, (G) the late stage of

the rapid transition period, and (H) at the end of the etching process. For each sample, the etching process was terminated as soon as the sample had reached the desired $R_{ct}C_{dl}$ monitored from FT-EIS analyzer. 19

Fig. 1-6. (A) The XRD spectrum of partially etched ITO thin film samples whose durations of etching are marked in blue color at the left. The corresponding crystalline facets are marked above each XRD peak. (B) Change of the XRD peak intensity ratio I_{222}/I_{400} with the time duration of etching. The ITO samples were prepared by cutting the ITO-coated slide glass into individual rectangular pieces (1 cm × 1 cm) with a diamond cutter. 21

Fig. 1-7. (A) FESEM image of a PR-covered ITO microdisk with 5.00 kX magnification when the etching process was completed, and (B) the magnified image of the edge area marked with yellow dashed rectangle with 50.00 kX magnification ratio. 23

Fig. 1-8. (A) Nyquist plot of the ITO microdisk under 3 M FeCl₃, 1 M HCl etchant at 47 °C obtained from FT-EIS measurement after the etching is completed. ($t = 6$ min, frequency range = 50 kHz ~ 1Hz). (B) Nyquist plots obtained from COMSOL simulation under the geometry of Fig. 1-3B at E_{eq} . Red symbol : $C_{Ox}^* = 20$ mM, $C_{Red}^* = 0$ mM, Black symbol : $C_{Ox}^* = C_{Red}^* = 10$ mM. (C) Cyclic voltammograms and (D) Nyquist plots obtained from COMSOL

simulation with varying PR thickness under the geometry of Fig. 1-3B. The vertical blue dashed line at $E = 0V$ indicates E_{eq} in (C). (scan rate = 50 mV/s, frequency range = 100 kHz ~ 1 Hz) The same electrochemical parameters (k^0 , C_{dl} , α , D_{Ox} , D_{Red}) were used as in Fig. 1-3. 24

Fig. 1-9. Nyquist plots of ITO microdisk electrode of the model geometries in Figs. 1-4B and 1-8B, computed from COMSOL simulation before (black symbols) and after (red symbols) the etching process is completed, where (A) $C_{Ox}^* = C_{Red}^* = 10$ mM, and (B) $C_{Ox}^* = 20$ mM, $C_{Red}^* = 0$ mM..... 25

Fig. 1-10. (A) FESEM image of an etched ITO microdisk whose PR layer was removed with acetone after the etching process. FESEM images of the edge area of the same sample with magnification ratio of (B) 50.00kX and (C) 100.00kX. (D) Tilted FESEM image for focusing on the remaining sidewall area. 26

Fig. 1-11. (A) Simplified illustration of the ITO interdigitated array (IDA) electrode. The width and length of each microelectrode was 5 μm and 1.2 mm respectively. The microelectrodes were located 10 μm apart from each other. The aspect ratio of the sketched image is different from the actual one. (B) $R_{ct}C_{dl}$ values of five IDA samples monitored in situ via FT-EIS analyzer during the chemical etching in 3 M FeCl_3 , 1 M HCl solution at 47 °C. The end points of each sample indicate

where the etching process was terminated. Optical microscopic images of (C) one of the five IDA sample chemically etched with FT-EIS monitoring, and (D) one of the other five that were chemically etched for 10 min without FT-EIS monitoring. The images in (C) and (D) were taken after removal of photoresist (PR) after the etching process. All the images of two sets of five etched ITO IDA samples with or without FT-EIS monitoring are presented in Fig. 1-12..... 28

Fig. 1-12. Optical microscopic images of (A) the five ITO interdigitated array (IDA) samples chemically etched with simultaneous FT-EIS monitoring, and (B) the other five chemically etched for 10 min without FT-EIS monitoring. The etching was carried out with 3 M FeCl_3 with 1 M HCl solution at 47 °C. All the images were taken after removal of photoresist (PR) after the etching process. The red dashed circles indicate the areas with damaged or broken patterns..... 29

Fig. 1-13. (A) Cyclic voltammograms of the etched ITO samples measured with 30 s of time interval from the initial state. The solution contained 10 mM $\text{K}_3[\text{Fe}(\text{CN})_6]$, 10 mM $\text{K}_4[\text{Fe}(\text{CN})_6]$ with 100 mM phosphate buffer (pH = 7.4) as supporting electrolyte. Black dashed vertical line indicates the formal potential of the system. The scan rate was 50 mV/s. (B) Nyquist plots obtained from conventional EIS near $E^{0'}$ for the same samples, solution in (A). The inset is magnified image of the Nyquist plots for the time range of 0 to 4 min. (C) R_{ct} , C_{dl}

parameters fitted from the EIS data of (B), and (D) temporal change of $R_{ct}C_{dl}$ value. The inset shows the magnified version for the time range of 0 to 4 min. 32

Fig. 1-14. (A) Chronoamperometric response during the ITO etching process under 3 M FeCl₃, 1 M HCl solution at 47 °C. The continuous square wave applied is described in Fig. 1-1A. The ITO sample used was identical to that in Scheme 1-1. Sampling rate was 2 kS/s. (B) Chronoamperogram for the time range of 3.8 min to 4.5 min from (A). 37

Fig. 1-15. Cyclic voltammograms consecutively accumulated during the ITO etching process using 3 M FeCl₃, 1 M HCl solution at 47°C. The first 12 cycles (black) were measured before the etching completion, and the succeeding cycles (red, from the 13th cycle) after the etching completion. The red arrow indicates that the limiting current of the CV decreased as the etching proceeded. Scan rate was 0.1 V/s. The other experimental conditions were identical to those in Fig. 1-14. 38

Fig. 1-16. (A) The first 5 CVs from Fig. 1-15, which are marked with black (1st), red (2nd), blue (3rd), magenta (4th), and green (5th) solid line, respectively. The black arrow indicates a slight shift of the onset potential toward positive direction. (B) The 5th (black, before etching) and last (red, after etching) cyclic voltammograms normalized so that their limiting current level would be the same. 39

Fig. 1-17. (A) Temporal change of total system impedance and (B) phase shift of the ITO film electrode, recorded by single frequency electrochemical impedance spectroscopy (EIS). The frequencies of AC signal used were 50 kHz (black), 25 kHz (red), 10 kHz (blue), 1 kHz (magenta), and 100 Hz (green), respectively. Sample interval was 2 s for EIS measurements using 50 kHz, 25 kHz, and 10 kHz-sinewaves, or 1 s for those using 1 kHz and 100 Hz-sinewaves. Bias potential was 0.490 V (vs. Ag/AgCl in 3 M NaCl reference electrode) 40

Fig. 1-18. (A) Simplified equivalent circuit of the system with pure R-C parallel component. R_{app} and C_{app} indicate the apparent resistive, and capacitive components. (B) R_{app} , (C) C_{app} , and (D) $R_{app}C_{app}$ values calculated from impedance data of Fig. 1-17. The frequencies of AC signal used were 50 kHz (black), 25 kHz (red), 10 kHz (blue), 1 kHz (magenta), and 100 Hz (green), respectively. Sample interval was 2 s for EIS measurements using 50 kHz, 25 kHz, and 10 kHz-sinewaves, or 1 s for those using 1 kHz and 100 Hz-sinewaves. Bias potential was 0.490 V (vs. Ag/AgCl in 3 M NaCl reference electrode) 41

Fig. 1-19. Conceptual illustration of in situ real-time FT-EIS analysis applied to the chemical etching process of ITO film electrode. 44

Fig. 2-1. Experimental scheme of voltage and current measurements using data acquisition (DAQ) device. AIs indicate analog input channels of

the device, each pair of which is composed of + and – terminals. The electrical potential difference between these two points was recorded constantly during the experiment. 57

Fig. 2-2. Illustrative schematic of ionic circuit powered by RED. Voltage generated from RED is applied to microfluidic polyelectrolyte diode directly via tubes filled with electrolyte. (CEM: Cation exchange membrane, AEM: Anion exchange membrane, H(L) NaCl solution: High(low) concentration NaCl solution) 65

Fig. 2-3. Time vs. voltage and ionic current plot of RED-powered ionic diode under (A) forward bias, and (B) reverse bias voltage. Note that the sign of voltage and current is inversed under reverse bias condition. (Black solid line: voltage generated from RED, Red solid line: voltage drop across the diode, Blue solid line: ionic current). 66

Fig. 2-4. Temporal fluorescence images of n-type pDADMAC gel in ionic diode using anionic fluorescein under (A) forward bias potential, and (B) reverse bias potential. The white numbers in the middle of each pair of images represent the elapsed time in second after connection of RED to the circuit. 66

Fig. 2-5. Comparison between temporal fluorescence images of pDADMAC gel under no external bias and reverse bias potential. The

white numbers in the middle of each pair of images indicate the elapsed time in second from the initial state..... 67

Fig. 2-6. Comparison between temporal fluorescence images of pDADMAC gel under no external bias and reverse bias potential. The white numbers in the middle of each pair of images indicate the elapsed time in second from the initial state..... 67

Fig. 2-7. Time vs. voltage and ionic current plot for repetitive voltage switching upon ionic diode through mechanical pressure on flexible connection tube filled with electrolyte under (A) forward, and (B) reverse bias condition. The bold O and C on the graph indicate the open(on) and closed(off) tube states, Note that the sign of voltage and current is inversed under reverse. (Black solid line: voltage generated from RED, Red solid line: voltage drop across the diode, Blue solid line: ionic current)..... 70

Fig. 2-8. I - V plot for forward-biased ionic diode at steady state with fluorescence images of n-type pDADMAC gel for each state during the voltage adjustment. The voltage drop across the circuit (V) and ionic current (I) were measured 120 s after steady state had been formed. 71

Fig. 2-9. (A) Microchip pattern of ionic OR logic circuit, (B) Truth table of the voltages from RED and output signals from the circuit, (C)

Fluorescence images for each state of the logic gate. Input voltage from RED was maintained at 3.1 V..... 73

Fig. 2-10. Surface anchoring reaction between the hydrogel monomers and the methacrylate groups on the TMSMA-coated glass substrate with presence of UV illumination..... 77

Fig. 2-11. General fabrication procedure of the hydrogel-based ionic circuit in glass microfluidic chip via UV-mediated photopolymerization in combination with a photomask. 78

Fig. 2-12. (A) Brief scheme of hydrogel stability test under aqueous condition of the hydrogel photopolymerized on the open PDMS surface, which is chemically modified. Volume of gel monomer (precursor) solution was controlled at 10 μ l. As fabricated hydrogel was immediately immersed in 10 mM KCl (aq) for 3 min. Simplified illustration of (B) hydrogel robustly attached onto the surface, and (C) hydrogel without effective adhesion to the surface, in electrolyte solution..... 84

Fig. 2-13. Photographs of (A) pDADMAC and (B) pSS gels formed on PDMS substrates prepared by following the surface modification procedures depicted in Scheme 2-1A to E. Top and bottom rows indicate whether the PDMS substrate was treated with MPTMS or GPTMS after the UV/ozone oxidation stage in Scheme 2-1A and B.

(left column: hydrogels as photopolymerized, right column: after the gel stability test procedure) 85

Fig. 2-14. (A) Photograph of the pDADMAC gel photopolymerized on the PDMS surface that was chemically modified by following the consecutive procedures enumerated in Scheme 2-1A to E; i) UV/ozone oxidation 3 hr, ii) MPTMS (in MeOH) treatment 2 hr, iii) 2 days at room temperature, and iv) EDT/DBU (in MeOH) treatment 2 hr. (B) Photograph of the bended hydrogel-PDMS hybrid in (A). 86

Fig. 2-15. Photographs obtained from the hydrogel stability test of (A) the pDADMAC and (B) pSS gels formed on PDMS substrates prepared by following the series of treatments: i) air plasma 1.5 min, and ii) silanization (TMSMA or MPTMS) 2 hr. The top and bottom rows indicate whether the PDMS substrate was treated with TMSMA or MPTMS after the plasma treatment. (left column: hydrogels as photopolymerized, right column: after the gel stability test procedure) 87

Fig. 2-16. Photographs obtained from the hydrogel stability test of the pDADMAC gels formed on PDMS substrates prepared by following the series of treatments: i) UV/ozone oxidation (A) 20 min or (B) 40 min, and ii) silanization (TMSMA or MPTMS) 2 hr. The top and bottom rows indicate whether the PDMS substrate was treated with

TMSMA or MPTMS after the UV/ozone oxidation. (left column: hydrogels as photopolymerized, right column: after the gel stability test procedure) 88

Fig. 2-17. Photographs obtained from the hydrogel stability test of (A) the pDADMAC and (B) pSS gels formed on PDMS substrates prepared by following the series of treatments: i) UV/ozone oxidation 3 hr, and ii) silanization (TMSMA or MPTMS) 2 hr. The top and bottom rows indicate whether the PDMS substrate was treated with TMSMA or MPTMS after the UV/ozone oxidation. (left column: hydrogels as photopolymerized, right column: after the gel stability test procedure) 89

Fig. 2-18. (A) Schematic illustration of a PDMS microfluidic ionic diode (PMID) composed of pSS and pDADMAC hydrogels. (Inset: optical microscope image of the diode junction with a photograph of the bended PMID) (B) Cyclic voltammogram of the PMID as fabricated. (scan rate = 10 mV/s, rectification ratio = 16.10) (C) Cyclic voltammograms of the PMID with varying scan rates; 0.1, 0.05, 0.02 and 0.01 V/s. Black arrows in (B) and (C) indicate that the voltage sweep started from 1.0 V toward negative potential. Solution filled inside the PMID was 10 mM KCl (aq)..... 92

Fig. 2-19. Cyclic voltammograms of a PMID measured immediately (black solid line), 1 day (red solid line), 1 month (blue solid line) after

the fabrication. The rectification ratios were 23.78, 22.60, 22.98, respectively. The solution filled inside the PMID was 10 mM KCl (aq). (Scan rate = 10 mV/s) 93

Fig. 2-20. (A) Photographs of the PMID before and after elongation, and (B) PMID stress-strain curve. (C) Cyclic voltammograms measured at several stretched states of the PMID; initial (0%), 10%, 20%, 30%, and recovered state. (D) Rectification ratio values for each diode CV in (C); 10.29 (initial, black), 5.85 (10%, red), 5.42 (20%, blue), 5.17 (30%, cyan), and 10.35 (recovered, magenta). Solution filled inside the PMID was 10 mM KCl (aq). (Scan rate = 20 mV/s)..... 94

Fig. 2-21. Photographs of the ruptured PMID after the tensile test. 95

Fig. 2-22. (A) Schematic illustration of the working principle of mechanical pressure-based switch integrated on PDMS microchip. (B) Ionic current recorded under constant voltage (= 1 V) applied to the PDMS microchannel with ca. 3 s of five switch actions. The microchannel was filled with 10 mM KCl solution. The channel length and width were 16 mm and 1.3 mm, respectively. The inset image represents the PDMS microchip used for the test..... 99

Fig. 2-23. (A) Schematic illustration of the PDMS microfluidic ionic regulator (PMIR) device. Area marked with blue dashed rectangle indicates an ionic circuit of interest to be driven by PMIR. S_1 and S_2

represent the ionic switch for each corresponding microchannel. V_1 and V_2 are two external voltages, V_{out} the voltage applied to the targeted ionic circuit, and I_{tot} the total ionic current. (B) Conceptual illustration of iontronic synaptic signal transmission triggered by external mechanical pressure imposed upon switches S_1 and S_2 on PMIR. Circuit diagram represents the antiparallel diodes and succeeding output load (Z_L) driven by PMIR. (C) V_{out} and I_{tot} recorded with individual switch operation. Duration of each switch action was approximately 3 s. V_1 and V_2 were maintained at 1.0 V and -2.0 V, respectively. 100

Fig. 2-24. Full equivalent circuit diagram of the PMIR device presented in Fig. 2-23A. R_1 and R_2 indicate the resistances of the two microchannels connected to each input voltage, respectively. S_1 and S_2 represent the mechanical ionic switches, Z the total resistive component of the ionic circuit of interest, V_{out} the voltage drop across Z , i_1 and i_2 the partial ionic currents flowing through R_1 and R_2 , respectively, I_{tot} the total ionic current flowing through Z 101

Fig. 2-25. Primary features of current iontronics expressed as a Venn diagram..... 105

List of Tables

Table 1-1. Near-surface atomic composition of Sn and In obtained from EDS analysis for ITO films with various etch durations.....	20
Table 1-2. Near-surface atomic composition of Sn and In obtained from EDS analysis for ITO films with various etch durations.....	29
Table 2-1. V_{out} and I_{tot} values when $R_1=R_2=R$, or Z is excessively greater than R ($=R_1=R_2$) in Fig. 2-24.....	102
Table 2-2. V_{out} and I_{tot} values when $R_1=R_2=R$, and $V_2=nV_1$ in Fig. 2-24.	102

1. Implementation of Fourier Transform Electrochemical Impedance Spectroscopy (FT-EIS) for Real-time Analysis

1.1 Introduction

Electrochemical impedance spectroscopy (EIS) has been deemed a powerful technique which gives a full knowledge of the faradaic components as well as the non-faradaic ones at the electrode surface.¹ Conventional EIS methods rely on phase sensitive detection (PSD) or frequency response analyzer (FRA) which normally takes a long time from several minutes to hours depending on the frequency range of interest.² Instead, Fourier transform electrochemical impedance spectroscopy (FT-EIS) uses excitation signals containing all the frequencies of interest is used as an excitation signal, and its current response is mathematically treated, i.e. Fourier transformed, for an immediate impedance calculation, which makes them a perfect electroanalytical tool for time-resolved impedance studies about transient phenomena. In the case of step-excitation FT-EIS being so-called the second generation FT-EIS (2G FT-EIS)^{3,4}, a step voltage, the integrated form of Dirac- δ function that contains sinusoidal waves of all frequencies with identical phase and magnitude, is applied to the electrochemical system for perturbation. The first derivative of the chronoamperometric data is then Fourier-transformed for impedance calculation.^{3,5-7} Owing to a dramatic decrease of the measurement time, one can monitor the electrochemical system in situ and in real-time while tracking the change of the system impedance. We chose the wet chemical etching process of

ITO film electrode in order to demonstrate the usefulness of the step-excitation FT-EIS.

As one of the transparent conducting oxide (TCO) materials, indium tin oxide (ITO) film has been widely used in a variety of applications such as liquid crystal displays (LCD)^{8,9}, light-emitting diodes (LEDs)^{10,11}, thin-film transistors (TFTs)^{12,13}, thin-film photovoltaics (PV)^{14,15} due to its good electrical conductivity and optical transparency.¹⁶ The majority of the aforementioned usages require the patterning of ITO film electrodes which is easily accomplished by chemical wet etching process because of its high throughput and inexpensiveness.^{17,18} Among many of the examples using patterned ITO electrodes are light-emitting diodes (LEDs) with ITO layer or patterns^{10,11,19}, LCD devices⁸, and numerous bioanalytical sensing platforms²⁰⁻²⁴ including 3D interdigitated ITO electrode array (IDA)²⁵⁻²⁷, enzyme-modified ITO microelectrode array²⁸. In consideration of its versatility as electrode material and a huge scale of industrial uses, it is undeniable that a thorough understanding of electrical and electrochemical aspects of ITO electrode in relation to its etching process is necessary for further development of relevant devices and material itself.

Alongside the extensive utilization of thin film ITO electrode in numerous devices, the wet chemical etching process of ITO film has also received considerable attention in terms of its physical, (electro)chemical properties, mechanism, kinetics and so on.²⁹⁻³² In general, the wet etching of ITO has been performed under acidic aqueous solutions such as phosphoric acid³⁰, aqua regia^{33,34}, oxalic acid³⁵⁻³⁸, and solutions based on halogen acids.^{17,18,30,34,39-41} In particular, halogen acid or its mixture with

ferric chloride is considered as one of the most widespread chemical etchants, and there even exist some commercialized products of HCl and FeCl₃ solution such as ITO etchant TE-100, CE-100, CE-200 (Transene, USA). Consecutive works conducted by Van den Meerakker demonstrated that undissociated halogen acid molecules (HXs) participate in the chemical dissolution of ITO, and the addition of I₂ or Fe³⁺ as oxidizing agents significantly increases the ITO etch rate with improvement of etched edge characteristics. They also proposed a chemical mechanism of ITO etching process in HCl solution containing FeCl₃.^{18,39} Su *et al.* examined the change of Sn/In ratio during the ITO etching under FeCl₃-HCl solution, and suggested the wet etching mechanism in the aspect of crystalline structure.¹⁷

In spite of several efforts focusing on the examination of chemical etching of ITO, there has been few researches on real-time electrochemical change of ITO film during the process. Although Brumbach *et al.* reported the acid activation phenomenon with ITO samples and differences in kinetic parameter from voltammograms⁴¹, the observed electrochemical change was a point-to-point comparison that had only resulted from the very initial stage (< 10 s) of acid treatment. Our work aims to fully investigate the electrochemical change of ITO film electrode in situ during the entire etching process in real-time manner, and provide property-based criteria to monitor and control the etching, whereas the general etching procedure has only been controlled by its time duration that highly relies on the manufacturing method of ITO and the etching environment.

In this dissertation, we report on the utilization of step-excitation FT-EIS for the in situ, real-time electrochemical analysis of ITO film electrode during the entire wet

etching process under HCl solution mixed with FeCl₃. We observed the electrode activation during the chemical etching, the progress and completion of the ITO etching process by constantly monitoring the fluctuation of equivalent circuit parameters (e.g. charge transfer resistance (R_{ct}), double layer capacitance (C_{dl})) that were simultaneously calculated from the FT-EIS data, which was also examined with field emission scanning electron microscopy (FESEM) images, energy dispersive X-ray spectroscopy (EDS), high resolution X-ray diffraction (HRXRD) and COMSOL simulation. We further applied this technique in order to procure undamaged interdigitated array (IDA) electrodes by preventing an excessive etching of ITO films with sophisticated pattern, and screening abnormal samples. The cyclic voltammograms and EIS measurements were carried out with partially etched ITO samples and solution containing [Fe(CN)₆]^{3-/4-} redox couple to validate the observed FT-EIS results.

1.2. Experimental Section

1.2.1. Materials

All chemicals were used without further purification. ITO coated glass (TIXZ003, 200 nm thick ITO on 0.7 mm thick borosilicate glass, ~10 ohms/sq of surface resistivity) fabricated by magnetron sputtering at 300 °C was purchased from Techinstro. Hydrochloric acid (HCl, 37%), ferric chloride hexahydrate ($\text{FeCl}_3 \cdot 6\text{H}_2\text{O}$, 97%), potassium hexacyanoferrate(III) ($\text{K}_3[\text{Fe}(\text{CN})_6]$), potassium hexacyanoferrate(II) trihydrate ($\text{K}_4[\text{Fe}(\text{CN})_6] \cdot 3\text{H}_2\text{O}$) were purchased from Aldrich.

1.2.2. Fabrication of PR-coated ITO micropatterns

The PR-coated ITO micropatterns (i.e. microdisk array, interdigitated array pattern) were fabricated by following a general photolithography procedure. TIXZ003 ITO coated glasses (75 mm × 25 mm, 0.7 mm thick, Techinstro, USA) were used as substrates. The substrate was rinsed with acetone, ethanol, and deionized (DI) water (NANOpure Diamond, Barnstead, USA) several times. After removing the moisture on the surface with an air blower, the cleaned ITO coated glass was dehydrated on a hot plate at 150 °C for 10 min and then cooled to room temperature. The slide was then spin-coated (YS-100MD, Won Corp., Korea) with hexamethyldisilazane (HMDS; Clariant, Switzerland) at 6000 rpm for 30 s. After soft baking the PR on a hot plate at 120 °C for 90 s, it was then coated with a photoresist (PR; AZ4620, Clariant, Switzerland) at 6000 rpm for 30 s. After soft baking the PR on a hot plate at 100 °C for 90 s, the substrate was cooled to room

temperature and aligned under a pattern mask. The PR on the slide was exposed to UV light (365 nm) with an intensity of 21 mW cm^{-2} for 13 s (MDE-4000, Midas, Korea) and AZ 400 K developer (Clariant, Switzerland) for 150 s. The PR-coated substrate was then washed with DI water, and the PR was hard-baked on a hot plate at $120 \text{ }^{\circ}\text{C}$ for 15 min.

1.2.3. FT-EIS measurements and fitting of the impedance data

The step-excitation FT-EIS measurements were conducted by using our homemade fast-rise potentiostat, which had a rise time of $<50 \text{ ns/V}$. The 15 mV continuous square wave voltage was generated from a NI PXIe-5412 14-bit arbitrary waveform generator (NI, USA) and was applied to the electrochemical cell, which was followed by the data acquisition via NI PXIe-5922 24-bit high-speed digitizer (NI, USA) with 200 kS/s of sampling rate. The acquired voltage and current data were computed to be first derivatives, and then transformed to Nyquist plots in the frequency domain via discrete Fourier transform (DTFT) method⁷ with frequencies ranging from $1/t_{\text{pulse}}$ (1 Hz) to $S/4$ (50 kHz), where S means the scope sampling rate. The obtained EIS plots were simultaneously fitted by complex non-linear least square method (CNLS) for calculating the equivalent circuit parameters (e.g. R_{ct} and C_{dl}). All these operations were controlled by our customized LabVIEW program. The data acquisition system was interfaced to the PXIe-1082 express chassis (NI, USA) equipped with PXIe-8135 Core i7-3610QE controller (NI, USA).

1.2.4. Electrochemical measurements

All electrochemical measurements except the FT-EIS were performed with a CH Instruments (Austin, TX, USA) model 660E electrochemical analyzer. A conventional three-electrode cell assembly was employed in the experiments with ITO microdisk pattern electrode as a working electrode, Ag/AgCl reference electrode in 3 M NaCl (RE-5B, BASi, UK), and platinum wire as a counter electrode. All potentials were reported versus Ag/AgCl reference electrode. In the case of experiments at room temperature, the ITO microdisk substrate was mounted in a custom-made teflon cell so that the ITO micropattern could be exposed through a 6 mm-diameter hole. When the solution temperature had to be heated, a specially designed glassware connected to a circulating water bath (SH-WB-11CDN, SH Scientific, Korea) was utilized as an electrochemical cell.

1.2.5. COMSOL simulation

The finite element analysis software, COMSOL Multiphysics[®] v 5.4 was used to model the cyclic voltammograms and EIS plots on an ultramicroelectrode (UME) at E_{eq} . The electroanalysis interface in electrochemistry module was used to simulate the desired model system. Redox couple, the reduced species (Red) and oxidized species (Ox) represent ferrocyanide ($[\text{Fe}(\text{CN})_6]^{4-}$), and ferricyanide ($[\text{Fe}(\text{CN})_6]^{3-}$) respectively. Their diffusion coefficients, D_{Ox} and D_{Red} , were chosen to be 7.2×10^{-10} and 6.7×10^{-10} m²/s from one of the relevant literatures.⁴² The transfer coefficient, α , was assumed to be 0.5. The standard rate constant (k^0) and electrode capacitance

(C_{dl}) were calculated from the impedance measurement at E_{eq} carried out on macroscale ITO electrode with 0.5 mm of diameter in 10 mM $[\text{Fe}(\text{CN})_6]^{3-/4-}$ with 100 mM phosphate buffer (pH = 7.4) solution. According to eqn (1-1) and (1-2) below, k^0 is calculated from R_{ct} and bulk concentration of the redox species C^* , where $R = 8.3145 \text{ J K}^{-1} \text{ mol}^{-1}$, $T = 293.15 \text{ K}$. As the measured R_s , R_{ct} , and C_{dl} were 508.19 Ω , 56.171 k Ω , and 22.015 nF, respectively, k^0 and C_{dl} can be calculated as $2.37 \times 10^{-6} \text{ m/s}$ and 11.21 $\mu\text{F/cm}^2$.

$$i_0 = \frac{RT}{FR_{ct}} = F A k^0 C_{Ox}^{*(1-\alpha)} C_{Red}^{*\alpha} = F A k^0 C^* \quad (\text{where } C_{Ox}^* = C_{Red}^* = C^*) \quad (1-1)$$

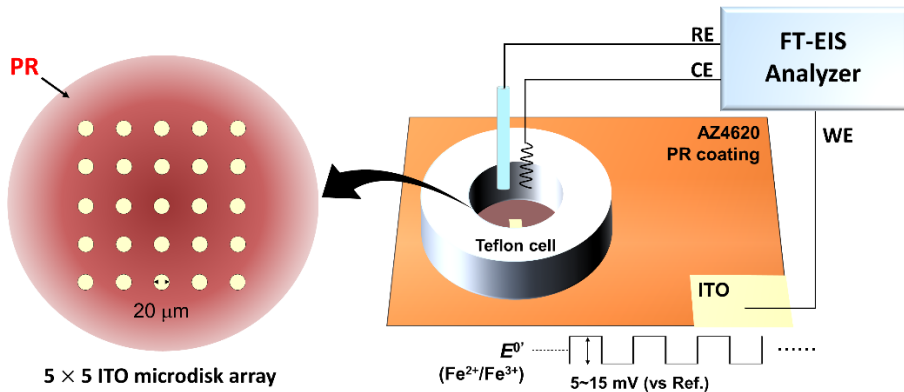
$$k^0 = \frac{RT}{F^2 R_{ct} A C^*} \quad (1-2)$$

1.2.6. Investigation of near-surface characteristics of etched ITO samples

Field emission scanning electron microscopy (FESEM) (SUPRA 55VP, Carl Zeiss, Germany) was used for observing surface morphologies of ITO substrates at several points during the chemical etching process. High resolution X-ray diffraction (HRXRD) (SmartLab, Rigaku, Japan) and energy-dispersive X-ray spectroscopy (EDS) (SUPRA 55VP, Carl Zeiss, Germany) were used to examine the crystallographic change and atomic composition of the etched ITO surface.

1.3. Results and Discussion

1.3.1. FT-EIS measurement of the ITO sample being etched



Scheme 1-1. Schematic illustration of FT-EIS analysis of 5×5 ITO microdisk patterns coated with AZ4620 photoresist under chemical etching process in 3 M FeCl_3 , 1 M HCl etchant at 47 °C. The distance between two nearest microdisks was 200 μm . The PR thickness was about 5 μm . The diameter of teflon cell hole through which the ITO pattern was exposed to etchant was 6 mm.

As depicted in Scheme 1-1, we designed an ITO micropattern composed of 25 (5×5 configuration) microdisks with a diameter of 20 μm in order to investigate the electrochemical change in real-time during the whole etching process. The pattern was fabricated through a common photolithographic procedure using AZ4620 as positive photoresist (PR) for the formation of insulation layer on ITO substrates. While these ITO microdisks undergo the chemical etching in HCl- FeCl_3 etchant, they also act as working electrode for the in situ FT-EIS measurement in 3-electrode

configuration. Fig. 1-1A shows that the continuous square wave signal with small amplitude was applied to the working electrode for the FT-EIS measurement as each impedance plot (Nyquist plot) was recorded at every rising and falling step.^{1,3,5-7} We only chose the impedance data from rising steps to extract Nyquist plots with controlled measurement condition. It is unnecessary to add additional redox material into the etchant for impedance analysis because the electrochemical reduction of inherent ferric ions can already occur. The concentration of ferric ion in etchant, $[\text{Fe}^{3+}]$, is kept constant throughout the entire process because the etching is Fe^{3+} -catalyzed chemical reaction at the ITO surface according to the reported mechanism.¹⁸ The FT-EIS analysis at a constant potential using square wave signals for the purpose of monitoring temporal changes differs from many other reported applications, most of which have been based on the staircase voltammetry FT-EIS (SCV FT-EIS) with changing potential.⁴³⁻⁵⁴

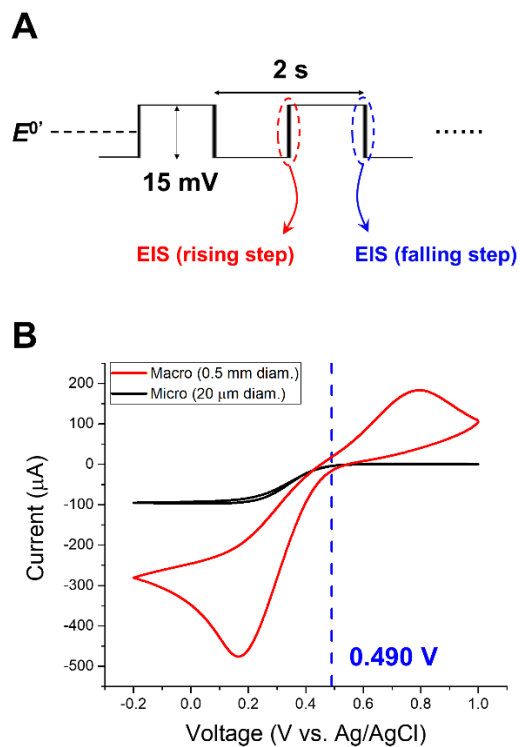


Fig. 1-1. (A) The square wave signal used in the FT-EIS measurement in Scheme 1-1. **(B)** Cyclic voltammograms measured immediately after the immersion of ITO macroelectrode (0.5 mm diam., red solid line) and the ITO microdisk array electrode depicted in Scheme 1-1 (black solid line) into the etchant. The scan rate was 0.1 V/s.

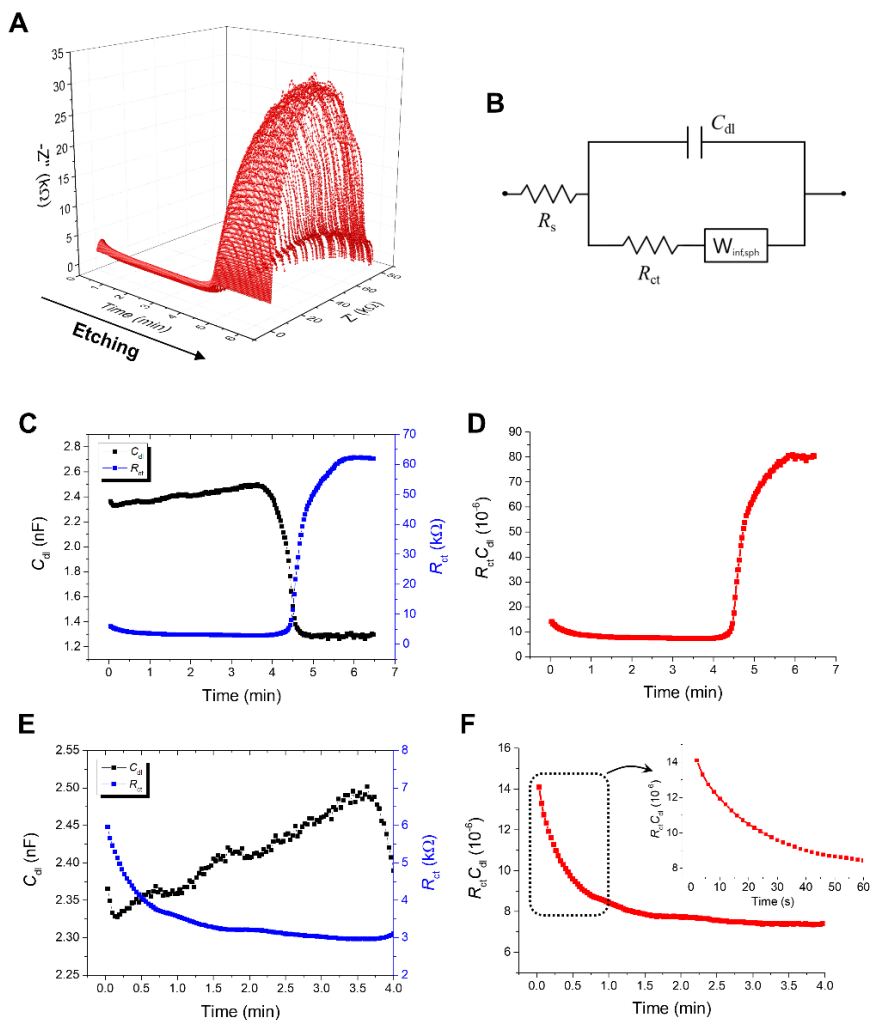


Fig. 1-2. (A) Accumulated Nyquist plots obtained from the FT-EIS measurement during the etching process in 3 M FeCl_3 , 1 M HCl etchant at 47 °C. The EIS frequency range was 50 kHz ~ 1 Hz with 2 s of time resolution. (B) Equivalent circuit used for fitting of the impedance data shown in (A). R_s indicates solution resistance, C_{dl} double layer capacitance, R_{ct} charge transfer resistance, and $W_{inf,sph}$ Warburg element of semi-infinite spherical diffusion. (C) Temporal change of the fitted R_{ct} , C_{dl} parameters, and (D) $R_{ct}C_{dl}$ value. (E, F) Magnified versions of (C, D) in the time range of 0 to 4 min. The inset shows the $R_{ct}C_{dl}$ value change during the initial 1 min.

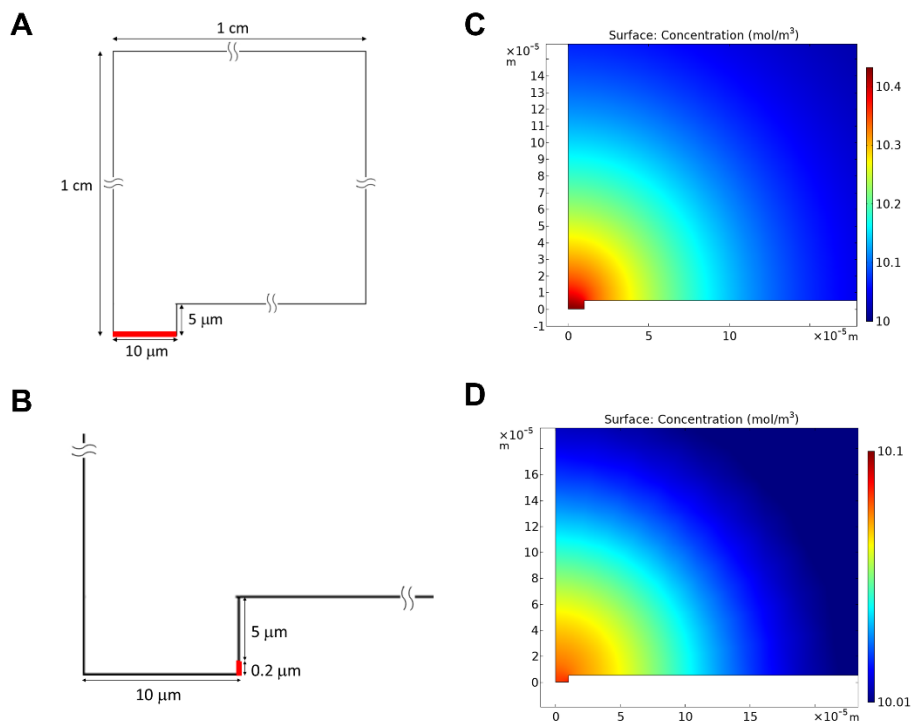


Fig. 1-3. Model geometries of the ITO microdisk electrode for COMSOL simulation for one-electron transfer reaction, $\text{Ox} + \text{e} \leftrightarrow \text{Red}$, with 2D axisymmetric configuration **(A)** when etching is still in process, and **(B)** when etching is finished. Red solid line indicates the ITO electrode surface. The 5 μm-wall stands for the PR insulation layer. The scale of the length might be different from the real dimension. Concentration profiles of Ox species at $E_{\text{eq}} (= 0 \text{ V})$ on cathodic scan when $C_{\text{Ox}}^* = C_{\text{Red}}^* = 10 \text{ mM}$ **(C)** for geometry of **(A)**, and **(D)** for geometry of **(B)**. ($k^0 = 2.37 \times 10^{-6} \text{ m/s}$, $C_{\text{dl}} = 11.21 \text{ μF/cm}^2$, $\alpha = 0.5$, $D_{\text{Ox}} = 7.2 \times 10^{-10} \text{ m}^2/\text{s}$, $D_{\text{Red}} = 6.7 \times 10^{-10} \text{ m}^2/\text{s}$, Scan rate = 50 mV/s)

The square wave applied to the ITO electrode in FT-EIS measurements is a signal biased at E^0 ($\text{Fe}^{3+}/\text{Fe}^{2+}$) with 15 mV of amplitude and 2 s of period (see Fig. 1-1A). The E^0 was experimentally determined to be approximately 0.490 V, the middle point of the two peak potentials of cyclic voltammogram (CV) of $\text{Fe}^{3+}/\text{Fe}^{2+}$ redox couple on macro ITO electrode as seen in Fig. 1-1B. According to Fig. 1-1B, the estimated E^0 is located in the vicinity of the onset potential of Fe^{3+} reduction current in the CV of ITO microdisk array, rather than at the half-wave potential. This may be ascribed to a relatively sluggish kinetics of $\text{Fe}^{3+}/\text{Fe}^{2+}$ couple in comparison with the well-known (quasi)reversible redox compounds. Therefore, the FT-EIS measurements on ITO microdisk array was conducted near the onset potential of Fe^{3+} reduction. As only the FT-EIS data calculated from rising steps were monitored, the time resolution of analysis is identical to the step period. The etchant composed of 3 M FeCl_3 , 1 M HCl aqueous solution was used with the operating temperature maintained at 47 °C, which conforms to a general etching condition in most photolithography processes. The 3D impedance plot in Fig. 1-2A demonstrates the temporal change of Nyquist plots. The impedance plots were simultaneously fitted with the equivalent circuit in Fig. 1-2B by using Levenberg-Marquardt algorithm^{2,55} to give R_{ct} and C_{dl} parameters in Fig. 1-2C to 2F. The equivalent circuit contains the semi-infinite spherical diffusional Warburg impedance that corresponds to the concentration profiles at E_{eq} obtained from COMSOL simulation in Fig. 1-3. It is improbable that the diffuse layers of the individual microdots overlap because the dots were isolated 200 μm apart from each other, which is acceptable to the criterion of microelectrode array design by Fletcher and Horne.⁵⁶ In Fig. 1-2D, the $R_{ct}C_{dl}$ value was also plotted as an indicator of electrochemical activity of ITO electrode.

According to eqn (1-3), the forward rate constant of an electrochemical redox reaction between Ox and Red, k_f , is related to standard rate constant, k^0 , where α is the charge transfer coefficient, F the Faraday constant, R the gas constant, T the absolute temperature, and E the potential applied.⁵⁷

$$k_f = k^0 \exp \left[-\frac{\alpha n F}{RT} (E - E^{0'}) \right] \quad (1-3)$$

Here, k_f can also be expressed as the following equation (eqn (1-4))^{45,58},

$$k_f = \frac{RT}{2n^2 F^2 A R_p C_O^*} \left[1 + \exp \left(-\frac{nF}{RT} (E - E^{0'}) \right) \right] \quad (1-4)$$

$$k^0 = \frac{RT}{2n^2 F^2 A R_p C_O^*} \left[\exp \left(\frac{\alpha n F}{RT} (E - E^{0'}) \right) + \exp \left(-\frac{(1-\alpha)nF}{RT} (E - E^{0'}) \right) \right] \quad (1-5)$$

where R_p is the polarization resistance obtained from impedance measurement, A the electrode area, C_O^* the bulk concentration of oxidized species Ox. The R_p becomes identical to R_{ct} when the impedance is measured at the formal potential, $E^{0'}$. Thus, the k^0 which represents the electrochemical kinetics is inversely proportional to R_p and A when the other parameters (C_O^* , E , $E^{0'}$) are fixed (see eqn (1-5)), which implies that the $R_{ct}C_{dl}$ values obtained from the FT-EIS analysis indicate the electrochemical activity of the electrode surface because all the measurements are carried out at the constant potential without significant change in chemical composition of the etchant.

1.3.2. The initial period of etching

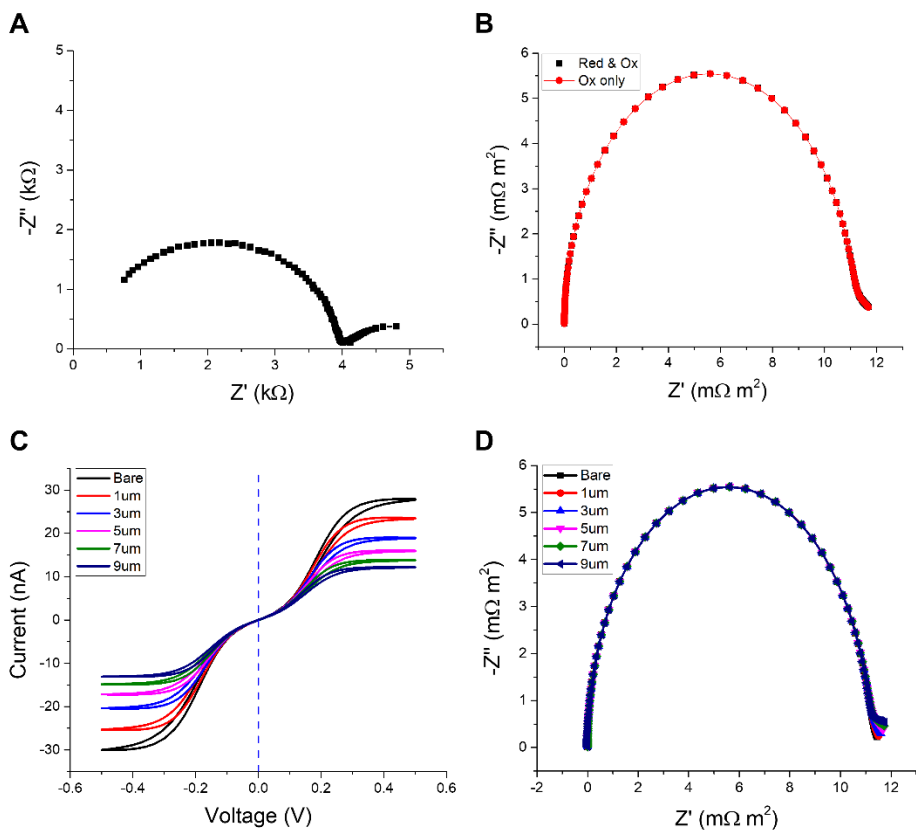


Fig. 1-4. (A) Nyquist plot of the ITO microdisk under 3 M FeCl_3 , 1 M HCl etchant at 47 °C obtained from FT-EIS measurement during the etching process ($t = 1$ min, frequency range = 50 kHz ~ 1Hz). (B) Nyquist plots obtained from COMSOL simulation under the geometry of Fig. 1-3A at E_{eq} . Red symbol : $C_{\text{Ox}}^* = 20$ mM, $C_{\text{Red}}^* = 0$ mM, Black symbol : $C_{\text{Ox}}^* = C_{\text{Red}}^* = 10$ mM. (C) Cyclic voltammograms and (D) Nyquist plots obtained from COMSOL simulation with varying PR thickness under the geometry of Fig. 1-3A. Vertical blue dashed line at $E = 0$ V indicates E_{eq} in (C). (scan rate = 50 mV/s, frequency range = 100 kHz ~ 1 Hz) The same electrochemical parameters (k^0 , C_{dl} , α , D_{Ox} , D_{Red}) were used as in Fig. 1-3.

Fig. 1-2D shows the activation behavior of ITO that was observed immediately after the immersion of the sample into the etchant, and it lasted for more than 4 min until the sharp increase of $R_{ct}C_{dl}$ occurred. When focusing on the early activation period up to around 4 min, the typical Nyquist plot is composed of a RC semicircle and a small proportion of diffusional Warburg impedance as shown in Fig. 1-4A, which is similar to the simulation result in Fig. 1-4B in that the RC semicircles are dominant in the EIS plot. Although there only exists the Ox species (Fe^{3+}) in the etchant, the simulation results in the presence of both Red and Ox species are also valid in EIS analysis near E_{eq} because the simulation gives identical EIS plots in both the cases (see Fig. 1-4B). One can see that R_{ct} decreases while C_{dl} slightly increases in a gradual manner, and that the activation effect is remarkable for the first 1 min and becomes saturated for the rest of the period as depicted in Fig. 1-2E and F. The height of insulation layer does not affect the RC semicircle in EIS plots but only alters limiting current levels in CV when etching is still in progress (see the COMSOL simulation results in Fig. 1-4C and D). Thus, the changes of R_{ct} , C_{dl} should not be caused by a subtle change of thickness of the ITO film resulted from etching, but by electrochemical and morphological changes of the electrode itself. A mild increase of C_{dl} before the rapid transition period in Fig. 1-2E may be attributed to the exposure of the roughened ITO surface as a result of chemical etching, which is in accordance with the change in surface morphology observed by FESEM as seen in Fig. 1-5. The decrease of R_{ct} should be partially ascribed to the increase of electrode area (C_{dl}) (see Fig. 1-5A to D), but primarily to the electrochemical activation of ITO because $R_{ct}C_{dl}$ dropped more severely than C_{dl} increased. Being analogous to the observation reported by Su *et al.*, the EDS analysis of the partially etched ITO thin

films in Table 1-1 shows an increase of Sn/In ratio near surface region as the etching proceeded.¹⁷ Though a higher rate constant of dimethylferrocene redox couple (DMFc/DMFc⁺) was observed on ITO electrodes that had been manufactured to be intrinsically higher in Sn/In ratio,⁴¹ it is not yet clear if the activated electrochemical kinetics is related to the atomic composition of Sn and In near the ITO surface. The X-ray diffraction pattern for (2 1 1), (2 2 2), (4 0 0), (4 3 1), (4 4 0) and (6 2 2) crystalline planes in Fig. 1-6A matches well with the indium oxide reference peaks at body-centered cubic (BCC) (JCPDS file No. 06-0416). A consistent decrease of XRD peaks along the etching procedure except the (2 2 2) facet of relatively slight intensity decrease implies that the etching proceeds with weakening of surface crystallinity, and that the (2 2 2) facet becomes dominant as the intensity ratio I_{222}/I_{400} increases (see Fig. 1-6B), which accords with the observation in the related literature.⁵⁹ Although the predominance of (2 2 2) facet on etched ITO surface might be related to the change of electrochemical activity, more detailed investigations are required for unraveling their correlation. The time duration required for this initial activation might be increased or decreased depending on the temperature or the chemical composition of etchant, which could be easily monitored through the FT-EIS by properly modulating its time resolution. Accordingly, the usage of this FT-EIS technique in combination with etching process could be enlarged to procure ITO samples with desired electrochemical activity.

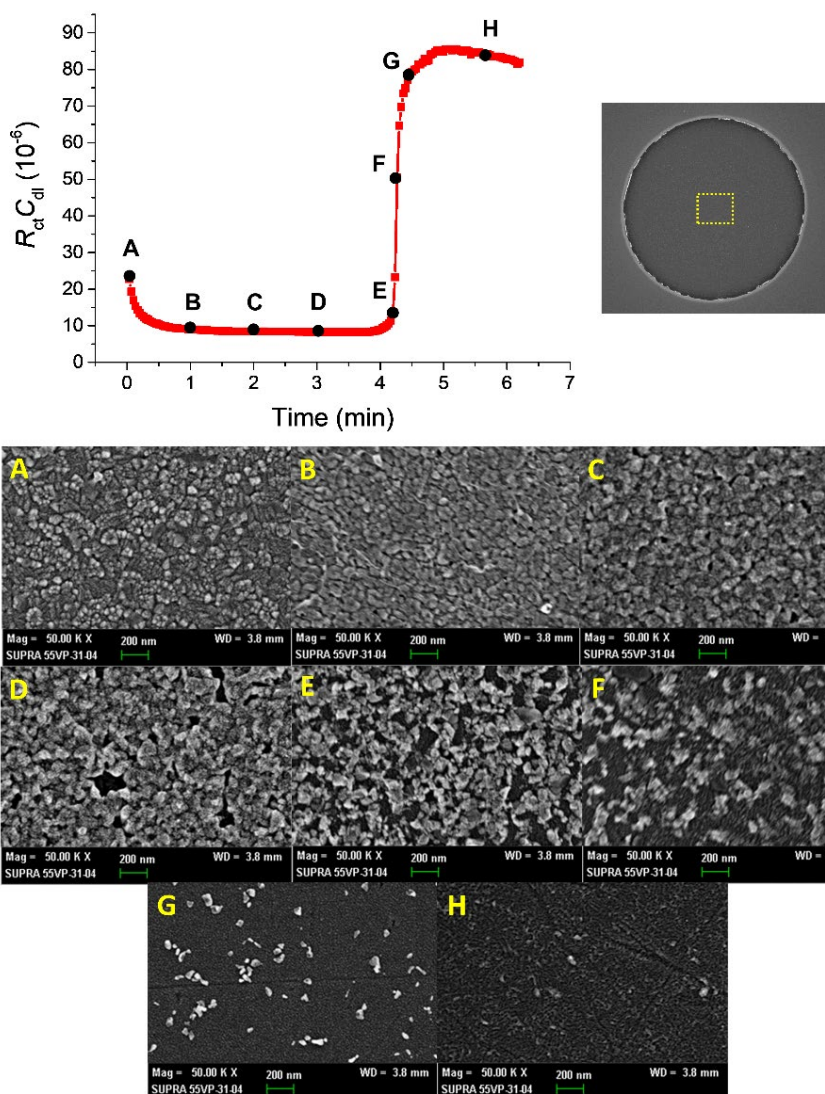


Fig. 1-5. Field emission scanning electron microscopy (FESEM) images of partially etched ITO microdisk array samples at several time points. The images represent the center area of a microdisk marked with yellow dashed rectangle area at **(A)** 0 min, **(B)** 1 min, **(C)** 2 min, **(D)** 3 min, and **(E)** the beginning, **(F)** the midpoint, **(G)** the late stage of the rapid transition period, and **(H)** at the end of the etching process. For each sample, the etching process was terminated as soon as the sample had reached the desired $R_{ct}C_{dl}$ monitored from FT-EIS analyzer.

	Etch duration (min)					
	0	0.5	1	1.5	2	2.5
Relative composition (%)						
In	23.27	21.01	18.56	16.77	10.70	7.70
Sn	2.23	2.02	1.80	1.67	1.09	0.81
Sn/In	0.0958	0.0961	0.0970	0.0996	0.1019	0.1052

Table 1-1. Near-surface atomic composition of Sn and In obtained from EDS analysis for ITO films with various etch durations.

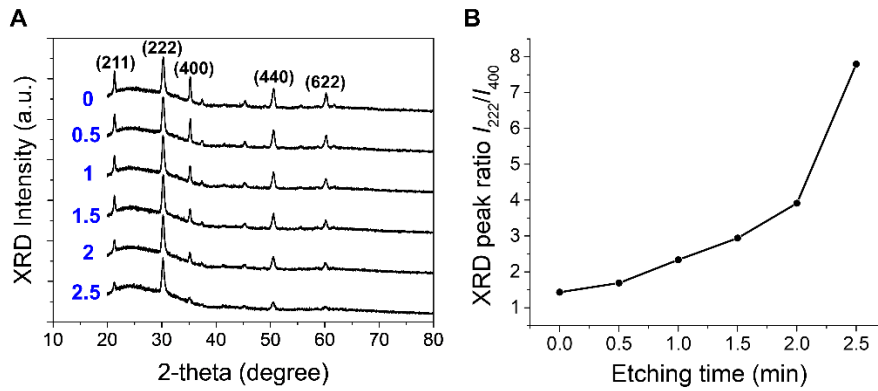


Fig. 1-6. (A) The XRD spectrum of partially etched ITO thin film samples whose durations of etching are marked in blue color at the left. The corresponding crystalline facets are marked above each XRD peak. **(B)** Change of the XRD peak intensity ratio I_{222}/I_{400} with the time duration of etching. The ITO samples were prepared by cutting the ITO-coated slide glass into individual rectangular pieces (1 cm \times 1 cm) with a diamond cutter.

1.3.3. Monitoring termination of etching process via FT-EIS analysis

After the etching process proceeds for more than 4 min, $R_{ct}C_{dl}$ leaps as R_{ct} rapidly increases whereas C_{dl} decreases as observed in Fig. 1-2C and D. In view of the FESEM images in Fig. 3E-H, this transitional period is represented by a sudden loss of the effective area of ITO which can function as electrode. All the FESEM images in Fig. 1-5 throughout the entire process indicate that ITO grains are eroded quite uniformly from the whole exposed area until the majority of the area is etched, leaving only a small sidewall of ITO (Fig. 1-7). The RC semicircle is predominant in Nyquist plots after the transitional period with very small contribution of Warburg component as displayed in Fig. 1-8A just as the COMSOL simulation showed a similar result with the Nyquist plot almost without Warburg component (Fig. 1-8B). In common with the geometry before completion of etching, the effect of electrode depth, i.e. PR thickness, is negligible for RC semicircle in EIS plots despite the change of limiting current level (Fig. 1-8C and D). More importantly, the $R_{ct}C_{dl}$ should remain constant even with the geometry change after the termination of etching process if the standard rate constant, k^0 , of the electrode reaction is unchanged (Fig. 1-9). Therefore, the sharp rise of $R_{ct}C_{dl}$ observed in the etching may imply that the sidewall ITO that has undergone the chemical etching has a smaller k^0 for the same electrochemical reaction than that of the initial ITO surface. It appears that the morphological and crystallographic nature of the etched sidewall ITO differs from that of the pristine ITO surface as shown in the tilted FESEM image of the same ITO microdisk whose PR layer was removed with acetone after the etching

process (Fig. 1-10). However, further sophisticated investigations are necessary to verify if this ‘deactivation effect’ exists at the moment of the termination of ITO etching because the exact geometry of PR-covered etched samples is hard to be defined for an accurate simulation. Once the $R_{ct}C_{dl}$ had increased after the termination of etching process, the value was almost maintained as shown at the end of the period (> 6 min) in Fig. 1-2D.

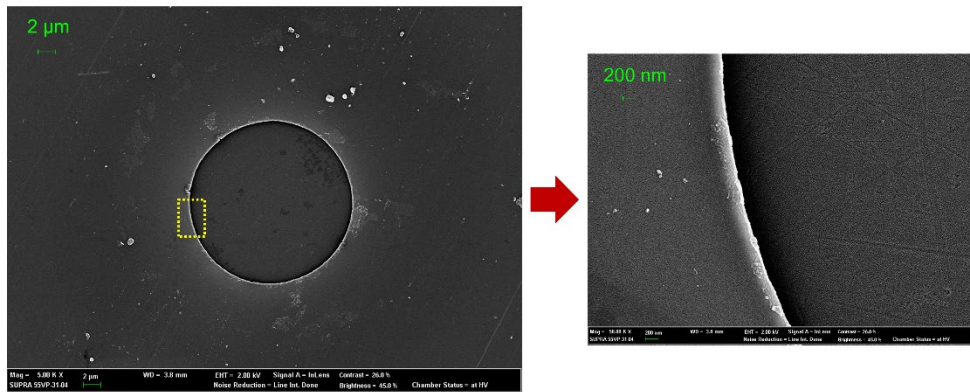


Fig. 1-7. (A) FESEM image of a PR-covered ITO microdisk with 5.00 kX magnification when the etching process was completed, and (B) the magnified image of the edge area marked with yellow dashed rectangle with 50.00 kX magnification ratio.

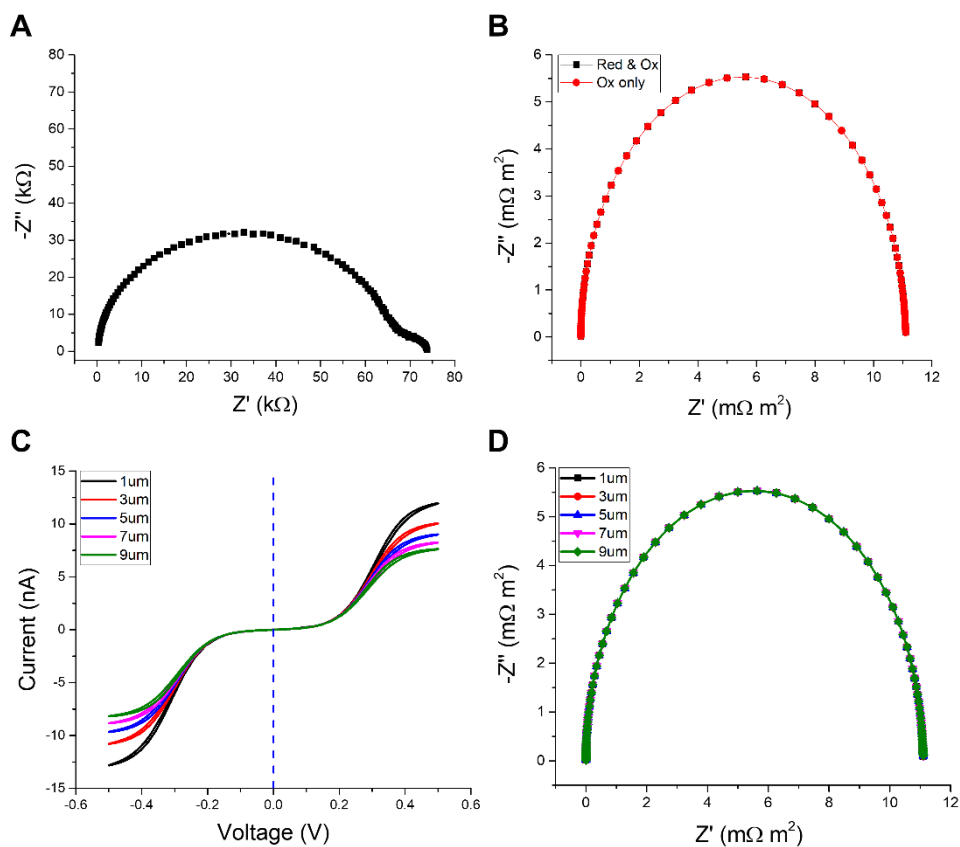


Fig. 1-8. (A) Nyquist plot of the ITO microdisk under 3 M FeCl_3 , 1 M HCl etchant at 47 °C obtained from FT-EIS measurement after the etching is completed. ($t = 6$ min, frequency range = 50 kHz ~ 1Hz). (B) Nyquist plots obtained from COMSOL simulation under the geometry of Fig. 1-3B at E_{eq} . Red symbol : $C_{\text{Ox}}^* = 20$ mM, $C_{\text{Red}}^* = 0$ mM, Black symbol : $C_{\text{Ox}}^* = C_{\text{Red}}^* = 10$ mM. (C) Cyclic voltammograms and (D) Nyquist plots obtained from COMSOL simulation with varying PR thickness under the geometry of Fig. 1-3B. The vertical blue dashed line at $E = 0\text{V}$ indicates E_{eq} in (C). (scan rate = 50 mV/s, frequency range = 100 kHz ~ 1 Hz) The same electrochemical parameters (k^0 , C_{dl} , α , D_{Ox} , D_{Red}) were used as in Fig. 1-3.

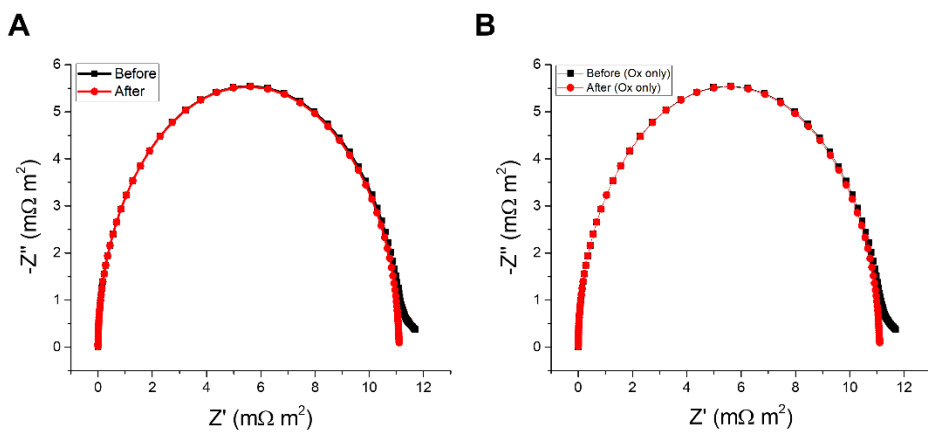


Fig. 1-9. Nyquist plots of ITO microdisk electrode of the model geometries in Figs. 1-4B and 1-8B, computed from COMSOL simulation before (black symbols) and after (red symbols) the etching process is completed, where **(A)** $C_{Ox}^* = C_{Red}^* = 10$ mM, and **(B)** $C_{Ox}^* = 20$ mM, $C_{Red}^* = 0$ mM.

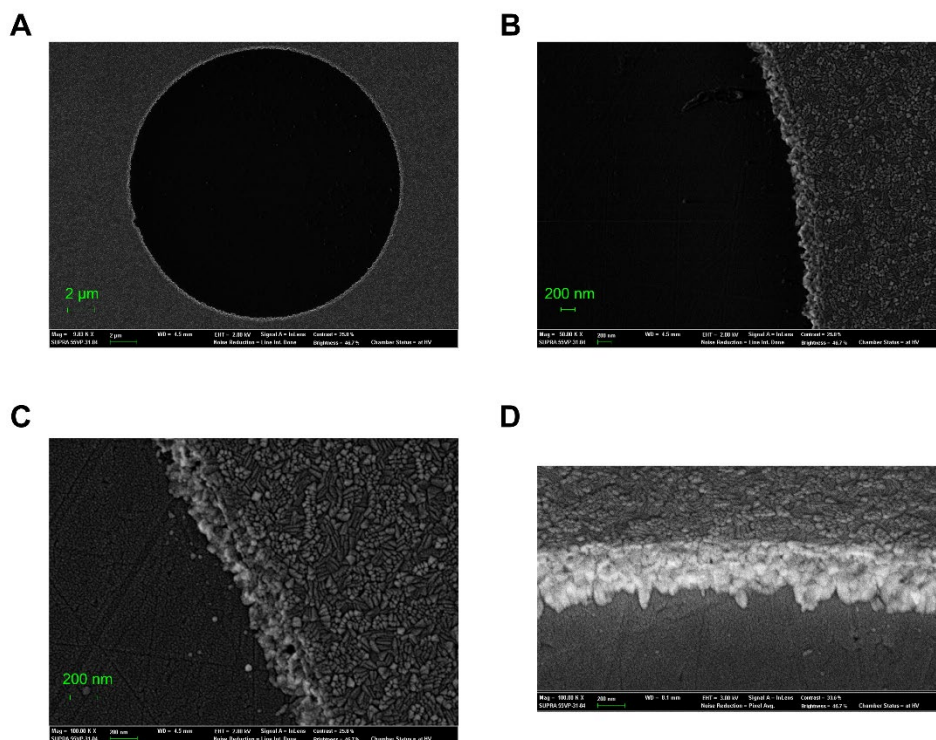


Fig. 1-10. (A) FESEM image of an etched ITO microdisk whose PR layer was removed with acetone after the etching process. FESEM images of the edge area of the same sample with magnification ratio of (B) 50.00kX and (C) 100.00kX. (D) Tilted FESEM image for focusing on the remaining sidewall area.

In consideration of the FT-EIS observations, we exploited this technique for the etching process of ITO interdigitated array (IDA) electrodes as an example of more sophisticated patterns which could be prone to damage during the etching. As displayed in Fig. 1-11A, we designed a micropattern composed of 3 pairs of 5 μm -wide interdigitated ITO microelectrodes, which are situated 10 μm apart from each other. The chemical etching process under the same condition was carried out while the change of $R_{\text{ct}}C_{\text{dl}}$ value was continuously tracked at the same time via FT-EIS measurements (Fig. 1-11B), which allowed us to successfully fabricate the 5 undamaged ITO IDA electrodes as presented in Fig. 1-11C and Fig. 1-12A. It was possible to terminate the etching right after the actual completion of the process because the temporal changes of $R_{\text{ct}}C_{\text{dl}}$ for the samples showed the early electrode activation as well as the completion of the etching process visualized by a sharp increase of $R_{\text{ct}}C_{\text{dl}}$ likewise with Fig. 1-2D. On the contrary, the other 5 IDA samples chemically etched for 10 min^{26,27,60} under the assumption that the optimized etching condition was unknown showed a number of broken, damaged electrode patterns (Fig. 1-11D and Fig. 1-12B). As summarized in Table 1-2, the etching durations of the IDA samples in Fig. 1-11B range from 4.60 to 5.50 min, which suggests the usefulness of FT-EIS in optimizing the etching condition for a given ITO sample and etchant, and screening out abnormalities or sample failures.

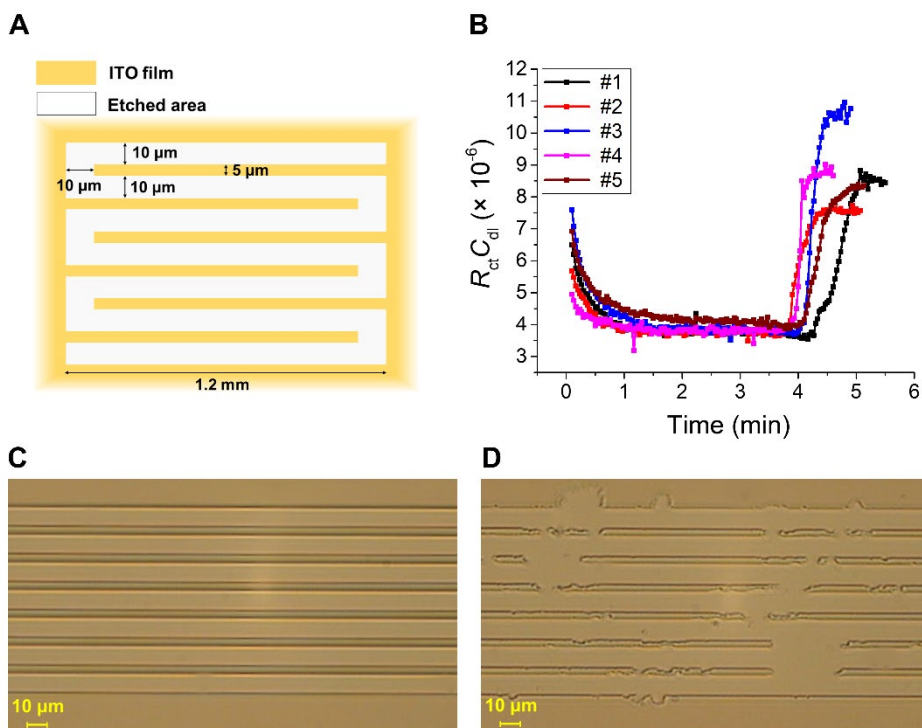


Fig. 1-11. (A) Simplified illustration of the ITO interdigitated array (IDA) electrode. The width and length of each microelectrode was 5 μm and 1.2 mm respectively. The microelectrodes were located 10 μm apart from each other. The aspect ratio of the sketched image is different from the actual one. (B) $R_{ct}C_{dl}$ values of five IDA samples monitored in situ via FT-EIS analyzer during the chemical etching in 3 M FeCl_3 , 1 M HCl solution at 47 $^\circ\text{C}$. The end points of each sample indicate where the etching process was terminated. Optical microscopic images of (C) one of the five IDA sample chemically etched with FT-EIS monitoring, and (D) one of the other five that were chemically etched for 10 min without FT-EIS monitoring. The images in (C) and (D) were taken after removal of photoresist (PR) after the etching process. All the images of two sets of five etched ITO IDA samples with or without FT-EIS monitoring are presented in Fig. 1-12.

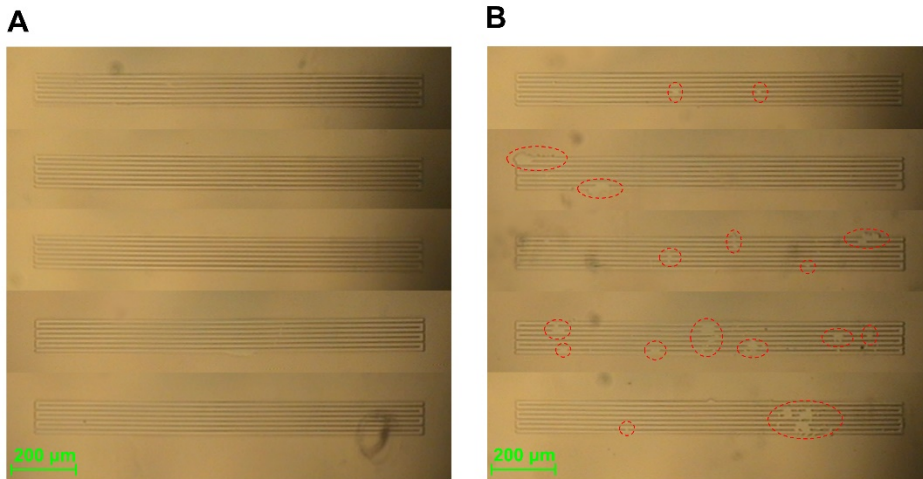


Fig. 1-12. Optical microscopic images of **(A)** the five ITO interdigitated array (IDA) samples chemically etched with simultaneous FT-EIS monitoring, and **(B)** the other five chemically etched for 10 min without FT-EIS monitoring. The etching was carried out with 3 M FeCl₃ with 1 M HCl solution at 47 °C. All the images were taken after removal of photoresist (PR) after the etching process. The red dashed circles indicate the areas with damaged or broken patterns.

Sample No.	#1	#2	#3	#4	#5
Etching duration (min)	5.50	5.07	4.90	4.60	5.13

Table 1-2. Near-surface atomic composition of Sn and In obtained from EDS analysis for ITO films with various etch durations.

1.3.4. Validation of FT-EIS results using conventional electroanalytical techniques

To confirm the observed tendency of electrochemical change of ITO surface under the etching, we obtained CVs using 10 mM ferri- and ferrocyanide solution, including the conventional EIS data near $E^{0'}$ every 30 s from the initial state to the end of the process for the same sample by temporarily pausing the etching with DI water rinsing. The CVs in Fig. 1-13A show an immediate activation by the first 30 s of etchant immersion, and that the ITO electrode appears to maintain its activated state for up to 4 min followed by an abrupt decrease of current level afterwards without a significant shift of $E^{0'}$. As demonstrated in Fig. 1-13B and C, the Nyquist plots and the fluctuation of the fitted R_{ct} , C_{dl} parameters follow a similar trend to that of FT-EIS results in etchant in Fig. 1-2A and C. The increased electrochemical activity of partially etched ITO electrodes was still maintained even after they had been taken out of the etchant, indicating that a slight etching can make ITO surface electrokinetically active. The shape of the obtained Nyquist plots mostly accords with those computed from COMSOL simulation (see Fig. 1-4B and 8B). Likewise, the trend of $R_{ct}C_{dl}$ with the duration of etching in Fig. 1-13D indicates an early activation period (0 ~ 4 min) followed by the rapid transitional period, and the termination of etching process, which consists with the FT-EIS analysis (Fig. 1-2D). The time required to complete the etching was observed as approximately 4 ~ 6 min, and also not affected by the voltage applied to the ITO for FT-EIS analysis, which is plausible because the potential applied was near the onset potential of the Fe^{3+} reduction current on ITO sample (see Fig. 1-1). As reported in the literature, the etch

speed in FeCl₃-HCl-based etchant depends on the surface concentration of Fe³⁺ and [HCl].¹⁸ If the potential applied is higher than the onset potential of Fe³⁺ reduction, the surface concentration of Fe³⁺ is practically identical to the bulk concentration. Although the electrochemical change of our ITO microdisk array was partially examined through cyclic voltammetry and conventional EIS in this section, it would be impossible or extremely time-consuming to implement those conventional electroanalytical methods in order to continuously monitor the etching process under etchants with unknown chemical composition, or to handle the process with much longer time duration, or to detect unexpected abnormal behavior.

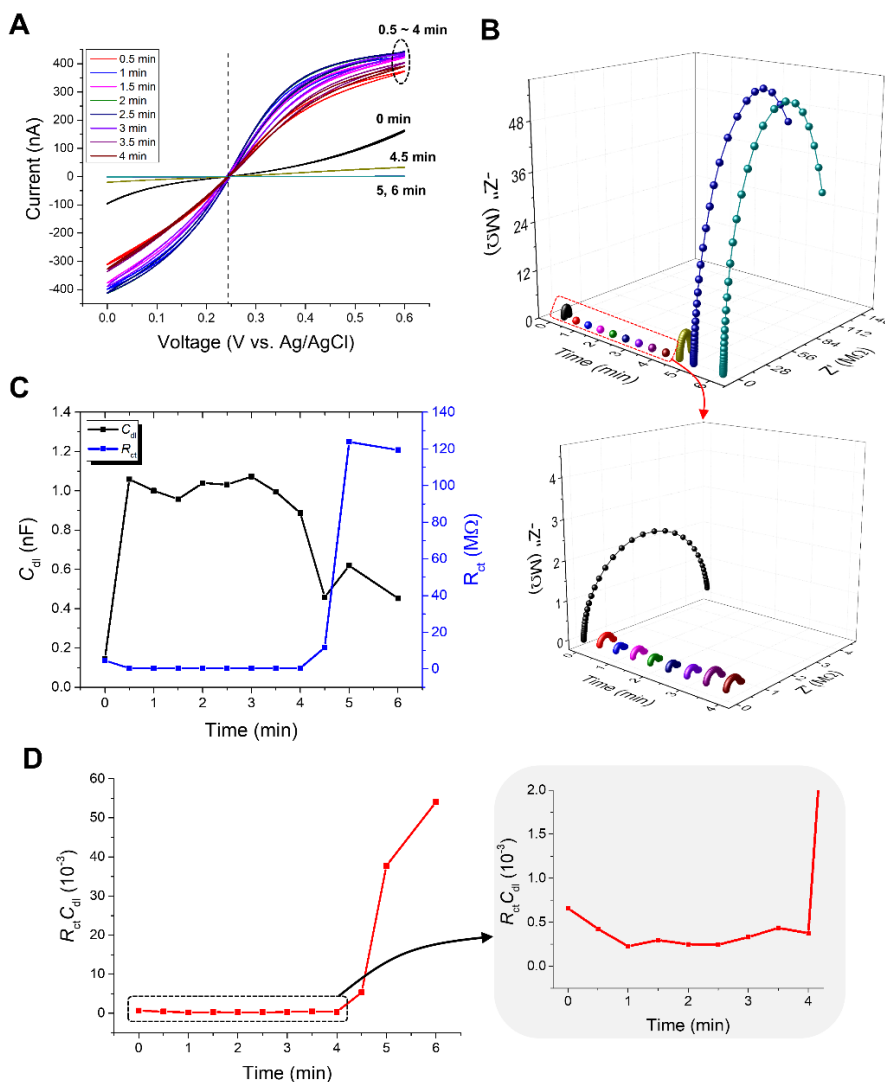


Fig. 1-13. (A) Cyclic voltammograms of the etched ITO samples measured with 30 s of time interval from the initial state. The solution contained 10 mM $K_3[Fe(CN)_6]$, 10 mM $K_4[Fe(CN)_6]$ with 100 mM phosphate buffer (pH = 7.4) as supporting electrolyte. Black dashed vertical line indicates the formal potential of the system. The scan rate was 50 mV/s. (B) Nyquist plots obtained from conventional EIS near E^0 for the same samples, solution in (A). The inset is magnified image of the Nyquist plots for the time range of 0 to 4 min. (C) R_{ct} , C_{dl} parameters fitted from the EIS data

of (B), and **(D)** temporal change of $R_{ct}C_{dl}$ value. The inset shows the magnified version for the time range of 0 to 4 min.

1.3.5. Electrochemical monitoring of ITO etching process using conventional electroanalytical techniques

To verify the usefulness and significance of using FT-EIS for the chemical etching of the ITO film, we conducted several conventional electroanalytical techniques in real-time during the process: chronoamperometry, cyclic voltammetry, and single frequency EIS. First, we applied the continuous square wave to the ITO film as described in Fig. 1-1A. The chronoamperometric response in Fig. 1-14A only shows the termination of etching process. As shown in Fig. 1-14B, the current level rapidly decreased at the time range of 4.1 to 4.3 min, together with a decrease of the amplitude of chronoamperometric response. This signifies a sudden loss of electrode area (C_{dl}) resulted from the etching. However, one cannot measure the degree of electrochemical (de)activation of ITO film during the entire process in an accurate manner, because the current response not only reflects the change in electrokinetics (R_{ct} or k^0), but the one in electrode area (C_{dl}). The continuous cyclic voltammograms in Fig. 1-15 also clearly shows the termination of etching process. The limiting current started to decrease abruptly from the 13th cycle, and continued to gradually decrease, which implies that the completion of etching occurred approximately at 4.4 min. Additionally, the slight shift of cyclic voltammogram toward anodic direction indirectly indicates the electrochemical activation of the electrode at the initial period of the process, as displayed in Fig. 1-16A. Similarly, the normalized CVs of the ITO film before and after etching process imply the electrochemical deactivation of the electrode (see the onset potential shift in Fig. 1-16B). Again, however, the cyclic voltammetry does not fully offer the electrochemical aspect of the changes inflicted upon the ITO film, given that the change in limiting current level comes from that of electrokinetics as well as that of electrode area, which is hard to be accurately extracted. In other words, despite the convenience in usage, the

chronoamperometry and cyclic voltammetry can be limitedly employed to detect the completion of etching process.

On the other hand, single frequency electrochemical impedance spectroscopy (EIS) offers more information than two of the aforementioned techniques. We tracked the change in impedance in real-time during the ITO etching process, as displayed in Fig. 1-17. We then calculated the change in resistance (R_{app}) and capacitance (C_{app}) of the system while we assumed that the equivalent circuit is solely composed of a R-C parallel component (see Fig. 1-18A). Given that the contribution of solution resistance and Warburg element was eliminated from the original equivalent circuit described in Fig. 1-2B, the R_{app} and C_{app} measured are apparent values. The total impedance of the R-C parallel circuit is expressed as eqn (1-6) and (1-7), where ω indicates the signal frequency, Z the total impedance of the system, Z_{Re} its real part, and Z_{Im} its imaginary part.

$$\frac{1}{Z} = \frac{1}{R_{app}} + jC_{app}\omega \quad (1-6)$$

$$Z = Z_{Re} + jZ_{Im} = \frac{R_{app}}{1+(R_{app}C_{app}\omega)^2} - \frac{R_{app}^2C_{app}\omega}{1+(R_{app}C_{app}\omega)^2}j \quad (1-7)$$

Eqn (1-7) can be rearranged so that R_{app} and C_{app} are expressed as equation of Z_{Re} and Z_{Im} (see eqn (1-8) and (1-9)).

$$R_{app} = \frac{Z_{Re}^2 + Z_{Im}^2}{Z_{Re}} \quad (1-8), \quad C_{app} = \frac{Z_{Im}}{\omega(Z_{Re}^2 + Z_{Im}^2)} \quad (1-9)$$

Namely, if the electrochemical system can be regarded as a pure R-C parallel equivalent circuit, those parameters can be monitored temporally via single frequency EIS. As demonstrated in Fig. 1-17, the changes in total system impedance

and phase angle allow us to detect the completion of etching process just as in the FT-EIS analysis (see Fig. 1-2 and 1-11). This can then be converted to the temporal change of R_{app} , C_{app} , and $R_{app}C_{app}$ according to eqn (1-8) and (1-9). Notably, both the early activation of ITO film and the termination of the process were observed from all the sinusoidal frequencies except for 100 Hz-AC signal (see Fig. 1-18B to D). Its deviation from the results obtained from FT-EIS and single frequency EIS using the other frequencies is not unsurprising, because the contribution of Warburg element becomes important at lower frequency. In the cases of the other frequencies, the propensity of parameter changes (i.e. R_{app} and C_{app}) was observed to be in line with that measured via FT-EIS, in spite of the value discrepancy among them. This may also be attributed to the simplification of the equivalent circuit, which implies that the AC frequency to be used should be sufficiently high to neglect the mass transport effect. Together, it would be the most appropriate to use an AC frequency where R_{app} and $C_{app}\omega$ could be similar to each other for accuracy and reproducibility of the analysis. If one chooses only to roughly estimate the electrode activation or the completion of the process, single frequency EIS could be a good choice. By extension, the efficacy of FT-EIS over single frequency EIS becomes prominent when it comes to the system composed of only R-C circuit with negligible mass transport effect.

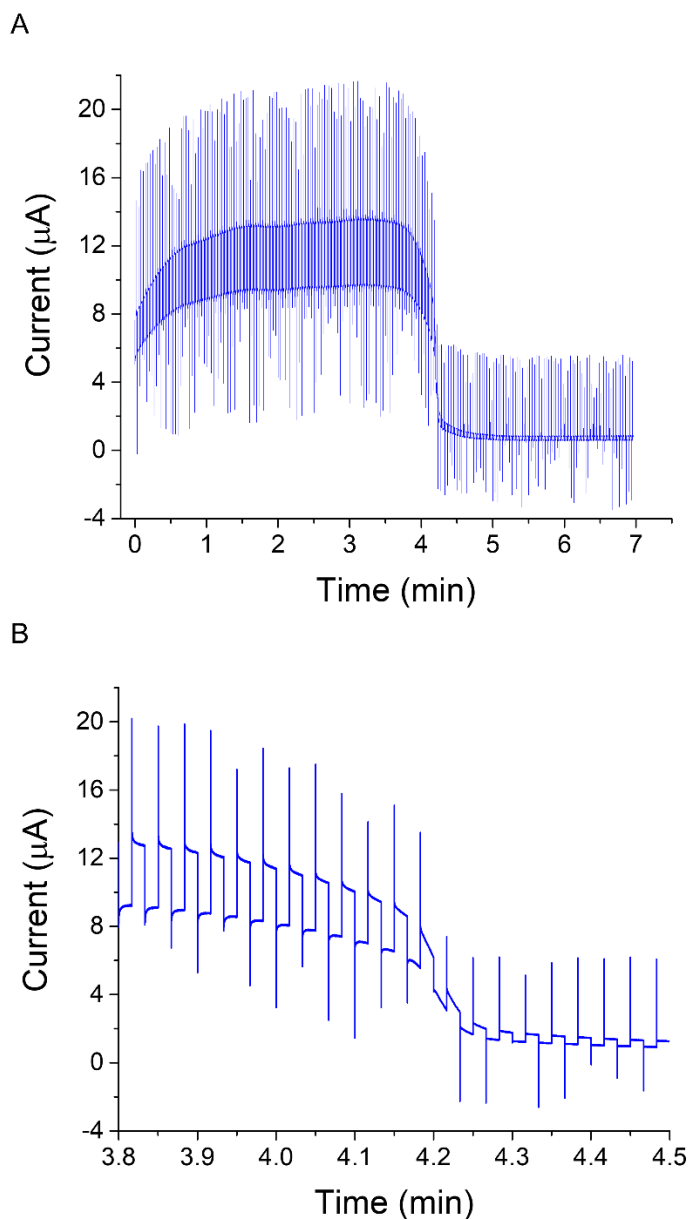


Fig. 1-14. (A) Chronoamperometric response during the ITO etching process under 3 M FeCl_3 , 1 M HCl solution at 47 °C. The continuous square wave applied is described in Fig. 1-1A. The ITO sample used was identical to that in Scheme 1-1. Sampling rate was 2 kS/s. (B) Chronoamperogram for the time range of 3.8 min to 4.5 min from (A).

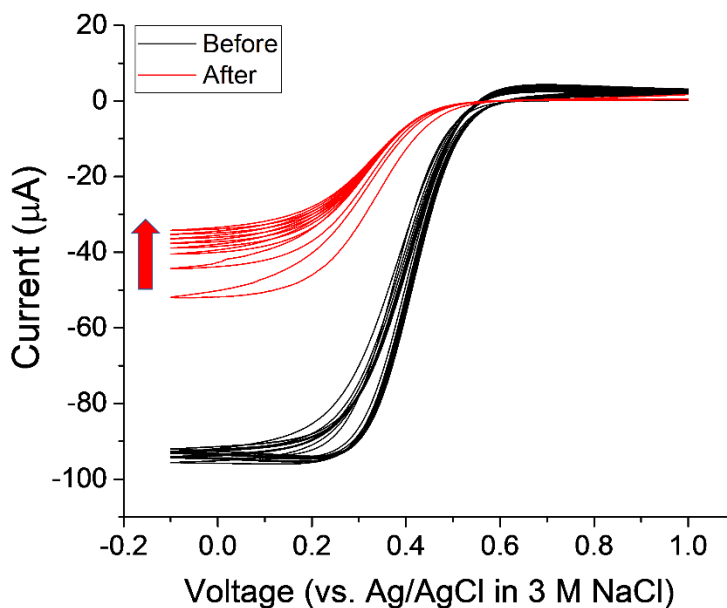


Fig. 1-15. Cyclic voltammograms consecutively accumulated during the ITO etching process using 3 M FeCl₃, 1 M HCl solution at 47°C. The first 12 cycles (black) were measured before the etching completion, and the succeeding cycles (red, from the 13th cycle) after the etching completion. The red arrow indicates that the limiting current of the CV decreased as the etching proceeded. Scan rate was 0.1 V/s. The other experimental conditions were identical to those in Fig. 1-14.

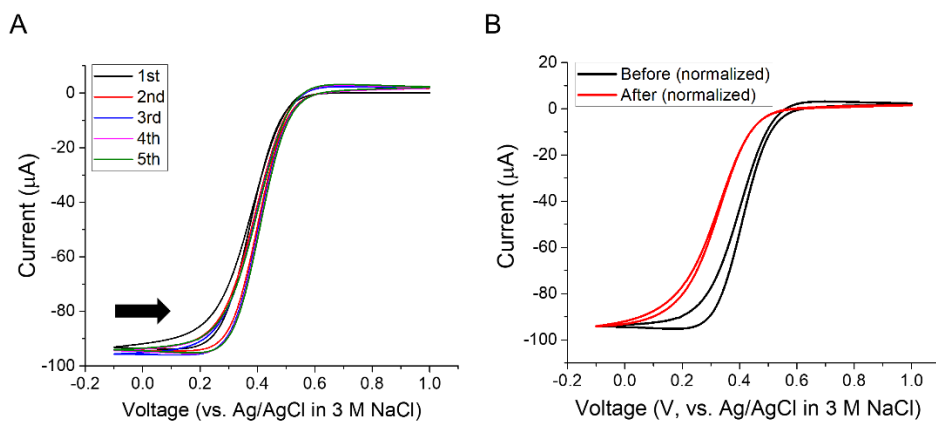


Fig. 1-16. (A) The first 5 CVs from Fig. 1-15, which are marked with black (1st), red (2nd), blue (3rd), magenta (4th), and green (5th) solid line, respectively. The black arrow indicates a slight shift of the onset potential toward positive direction. (B) The 5th (black, before etching) and last (red, after etching) cyclic voltammograms normalized so that their limiting current level would be the same.

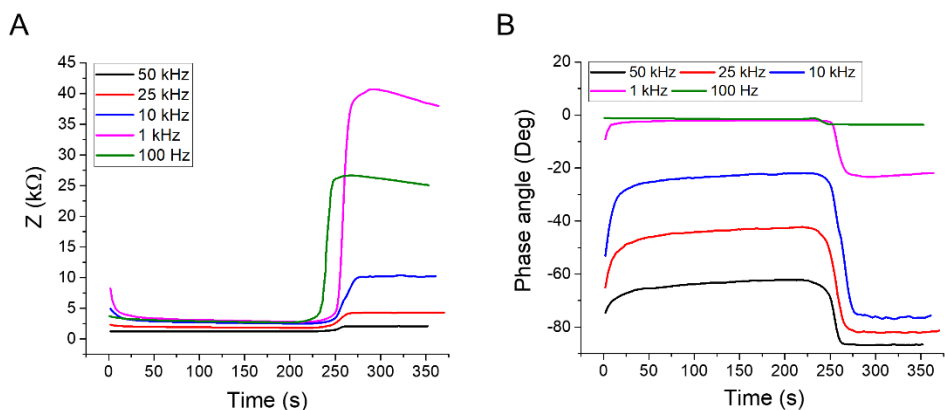


Fig. 1-17. (A) Temporal change of total system impedance and (B) phase shift of the ITO film electrode, recorded by single frequency electrochemical impedance spectroscopy (EIS). The frequencies of AC signal used were 50 kHz (black), 25 kHz (red), 10 kHz (blue), 1 kHz (magenta), and 100 Hz (green), respectively. Sample interval was 2 s for EIS measurements using 50 kHz, 25 kHz, and 10 kHz-sinewaves, or 1 s for those using 1 kHz and 100 Hz-sinewaves. Bias potential was 0.490 V (vs. Ag/AgCl in 3 M NaCl reference electrode)

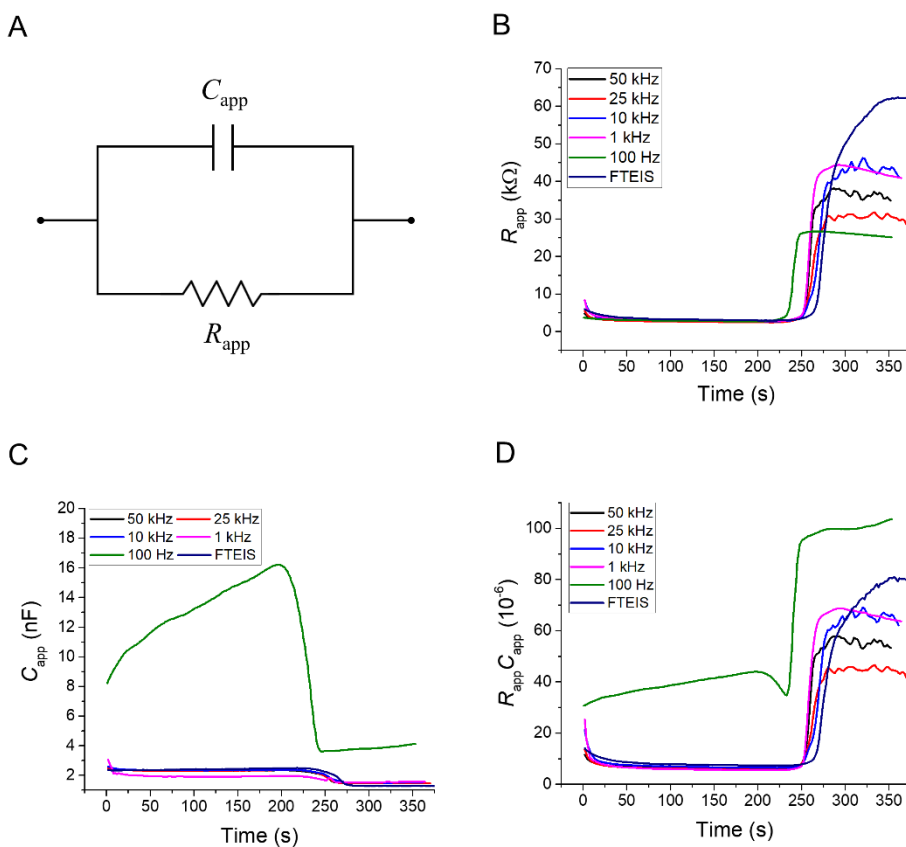


Fig. 1-18. (A) Simplified equivalent circuit of the system with pure R-C parallel component. R_{app} and C_{app} indicate the apparent resistive, and capacitive components. (B) R_{app} , (C) C_{app} , and (D) $R_{app}C_{app}$ values calculated from impedance data of Fig. 1-17. The frequencies of AC signal used were 50 kHz (black), 25 kHz (red), 10 kHz (blue), 1 kHz (magenta), and 100 Hz (green), respectively. Sample interval was 2 s for EIS measurements using 50 kHz, 25 kHz, and 10 kHz-sinewaves, or 1 s for those using 1 kHz and 100 Hz-sinewaves. Bias potential was 0.490 V (vs. Ag/AgCl in 3 M NaCl reference electrode)

1.4. Conclusion

In this dissertation, we demonstrate a real-time electrochemical examination of ITO thin film electrode under chemical etching process in situ via FT-EIS using continuous square wave signal (see Fig. 1-19). By monitoring changes of R_{ct} and C_{dl} obtained from simultaneous fitting of in situ FT-EIS data, we successfully tracked the electrochemical activation phenomenon at the early stage of the process which lasted for several minutes until the termination of the etching represented by a sudden increase of $R_{ct}C_{dl}$. Not only did the COMSOL simulations and additional experiments using ferri- and ferrocyanide accord with the observed electrochemical aspects from FT-EIS analysis, but they also ensured the retention of increased electrochemical activity of ITO film even after removing the etchant. The change of atomic composition and crystallinity at ITO surface obtained from EDS, XRD analyses could be correlated to the electrochemical observation. The huge increase of $R_{ct}C_{dl}$ resulted from the process might imply that the remaining ITO sidewall is somewhat deactivated in comparison to the initial ITO surface. The utilization of FT-EIS in etching interdigitated array (IDA) electrodes with delicate pattern suggested the technique as a powerful tool to prevent an excessive etching for individual samples by optimizing the procedure, or to prepare ITO electrodes with desired activity, and even to screen out abnormalities.

Although the electrochemical monitoring of the ITO etching process via chronoamperometry and cyclic voltammetry demonstrated the capability to detect the completion of the process, those techniques do not offer more electrochemical information than the change of the overall current level, or the onset potential shift

resulted from the change in electrochemical activity. In contrast, single frequency EIS furnishes information about the change that the ITO electrode undergoes in terms of electrochemical aspects, including the termination of the process. We observed that single frequency EIS could be a good electroanalytical tool just for monitoring the systems comprised of an R-C parallel component, or those whose equivalent circuit can be easily regarded as R-C circuit. It is of importance that the signal frequency should be carefully chosen depending on the specificity of the system. The forte of FT-EIS over single frequency EIS is to give a full description of the electrochemical system from electrokinetics to mass transport-related information upon a single measurement. In particular, a real-time impedance analysis focusing on electrochemical information obtained from both low frequency range (i.e. mass transfer) and high frequency region (i.e. electrokinetics) would be the perfect target for FT-EIS. This dissertation lets us rediscover the potential of FT-EIS enabling in situ real-time electrochemical examinations in other constantly changing, transient systems such as electrodeposition, corrosion, surface modification.

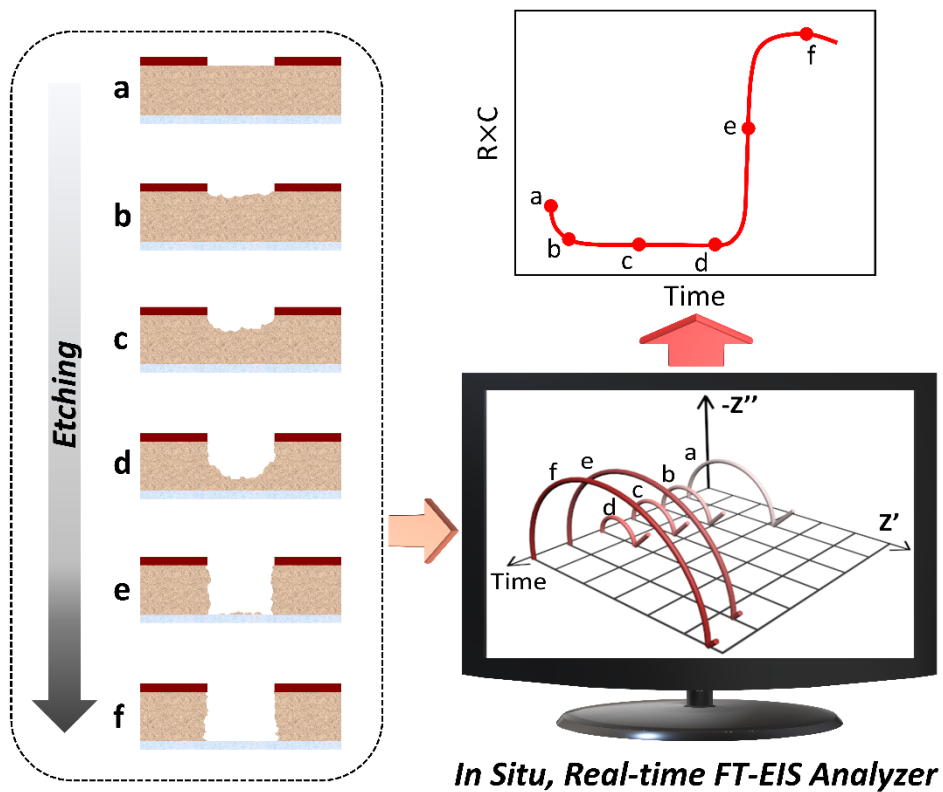


Fig. 1-19. Conceptual illustration of in situ real-time FT-EIS analysis applied to the chemical etching process of ITO film electrode.

1.5. References

- (1) Park, S.-M.; Yoo, J.-S.; Chang, B.-Y.; Ahn, E.-S. *Pure Appl. Chem.* **2006**, *78*, 1069-1080.
- (2) Lasia, A. *Electrochemical impedance spectroscopy and its applications*; Springer, New York, 2014.
- (3) Chang, B. Y.; Park, S. M. *Annu. Rev. Anal. Chem.* **2010**, *3*, 207-229.
- (4) Ha, L. D.; Park, K.; Chang, B.-Y.; Hwang, S. *Anal. Chem.* **2019**, *91*, 14208-14213.
- (5) Chang, B.-Y.; Park, S.-M. *Anal. Chem.* **2006**, *78*, 1052-1060.
- (6) Jurczakowski, R.; Lasia, A. *Anal. Chem.* **2004**, *76*, 5033-5038.
- (7) Yoo, J.-S.; Park, S.-M. *Anal. Chem.* **2000**, *72*, 2035-2041.
- (8) Sawada, M.; Higuchi, M.; Kondo, S.; Saka, H. *Jpn. J. Appl. Phys.* **2001**, *40*, 3332.
- (9) Yan, X.; Mont, F. W.; Poxson, D. J.; Schubert, M. F.; Kim, J. K.; Cho, J.; Schubert, E. F. *Jpn. J. Appl. Phys.* **2009**, *48*, 120203.
- (10) Choi, J.; Koh, T.-W.; Lee, S.; Yoo, S. *Appl. Phys. Lett.* **2012**, *100*, 123.
- (11) Li, S.; Kuo, D.; Liu, C.; Hung, S.; Chang, S.-J. *IET Optoelectron.* **2012**, *6*, 303-306.
- (12) Lee, J.; Kim, J.; Im, S. *Appl. Phys. Lett.* **2003**, *83*, 2689-2691.
- (13) Kim, S.; Ju, S.; Back, J. H.; Xuan, Y.; Ye, P. D.; Shim, M.; Janes, D. B.; Mohammadi, S. *Adv. Mater.* **2009**, *21*, 564-568.
- (14) Armstrong, N. R.; Carter, C.; Donley, C.; Simmonds, A.; Lee, P.; Brumbach, M.; Kippelen, B.; Domercq, B.; Yoo, S. *Thin Solid Films* **2003**, *445*, 342-352.

- (15) Schmidt, H.; Flügge, H.; Winkler, T.; Bülow, T.; Riedl, T.; Kowalsky, W. *Appl. Phys. Lett.* **2009**, *94*, 163.
- (16) Minami, T. *Thin Solid Films* **2008**, *516*, 5822-5828.
- (17) Su, S.-H.; Kong, H.-J.; Tseng, C.-L.; Chen, G.-Y. *Jpn. J. Appl. Phys.* **2017**, *57*, 01AE05.
- (18) Van den Meerakker, J.; Baarslag, P.; Scholten, M. *J. Electrochem. Soc.* **1995**, *142*, 2321-2325.
- (19) Gil, Y.; Kim, H. *Thin Solid Films* **2016**, *603*, 307-312.
- (20) Matsue, T.; Aoki, A.; Abe, T.; Uchida, I. *Chem. Lett.* **1989**, *18*, 133-136.
- (21) Sun, X.; Gillis, K. D. *Anal. Chem.* **2006**, *78*, 2521-2525.
- (22) Choi, C. K.; English, A. E.; Jun, S.-I.; Kihm, K. D.; Rack, P. D. *Biosens. Bioelectron.* **2007**, *22*, 2585-2590.
- (23) Wang, S.; Zhang, Y.; Yu, J.; Song, X.; Ge, S.; Yan, M. *Sens. Actuators B-Chem.* **2012**, *171-172*, 891-898.
- (24) Liu, F.; Zhang, Y.; Yu, J.; Wang, S.; Ge, S.; Song, X. *Biosens. Bioelectron.* **2014**, *51*, 413-420.
- (25) Lei, K. F. *Micro Nano Letters* **2011**, *6*, 157-160.
- (26) Han, D.; Kim, Y.-R.; Kang, C. M.; Chung, T. D. *Anal. Chem.* **2014**, *86*, 5991-5998.
- (27) Lee, D.; Lee, S.; Rho, J.; Jang, W.; Han, S. H.; Chung, T. D. *Biosens. Bioelectron.* **2018**, *101*, 317-321.
- (28) Puri, N.; Sharma, V.; Tanwar, V. K.; Singh, N.; Biradar, A. M.; Rajesh. *Prog. Biomater.* **2013**, *2*, 5.
- (29) Bradshaw, G.; Hughes, A. *Thin Solid Films* **1976**, *33*, L5-L8.

- (30) Ratcheva, T.; Nanova, M. *Thin Solid Films* **1986**, *141*, L87-L89.
- (31) Inoue, M.; Matsuoka, T.; Fujita, Y.; Abe, A. *Jpn. J. Appl. Phys.* **1989**, *28*, 274.
- (32) Hoheisel, M.; Mitwalsky, A.; Mrotzek, C. *Phys. Status Solidi A* **1991**, *123*, 461-472.
- (33) Venkatesan, M.; McGee, S.; Mitra, U. *Thin Solid Films* **1989**, *170*, 151-162.
- (34) Huang, C. J.; Su, Y. K.; Wu, S. L. *Mater. Chem. Phys.* **2004**, *84*, 146-150.
- (35) Tsai, T.-H.; Wu, Y.-F. *Microelectron. Eng.* **2006**, *83*, 536-541.
- (36) Tsai, T.-H.; Wu, Y.-F. *J. Electrochem. Soc.* **2006**, *153*, C86-C90.
- (37) Mammana, S. S.; Greatti, A.; Luiz, F. H.; da Costa, F. I.; Mammana, A. P.; den Engelsen, D.; Calligaris, G. A.; Cardoso, L. P.; IZ, C. *Proc. LatinDisplay* **2012**.
- (38) Mammana, S. S.; Greatti, A.; Luiz, F. H.; da Costa, F. I.; Mammana, A. P.; Calligaris, G. A.; Cardoso, L. P.; Mammana, C. I.; den Engelsen, D. *Thin Solid Films* **2014**, *567*, 20-31.
- (39) Scholten, M.; Van den Meerakker, J. *J. Electrochem. Soc.* **1993**, *140*, 471-475.
- (40) Van den Meerakker, J.; Baarslag, P.; Walrave, W.; Vink, T.; Daams, J. *Thin Solid Films* **1995**, *266*, 152-156.
- (41) Brumbach, M.; Veneman, P. A.; Marrikar, F. S.; Schulmeyer, T.; Simmonds, A.; Xia, W.; Lee, P.; Armstrong, N. R. *Langmuir* **2007**, *23*, 11089-11099.
- (42) Konopka, S.; McDuffie, B. *Anal. Chem.* **1970**, *42*, 1741-1746.
- (43) Yoo, J.-S.; Song, I.; Lee, J.-H.; Park, S.-M. *Anal. Chem.* **2003**, *75*, 3294-3300.
- (44) Chang, B.-Y.; Hong, S.-Y.; Yoo, J.-S.; Park, S.-M. *J. Phys. Chem. B* **2006**, *110*, 19386-19392.
- (45) Chang, B.-Y.; Park, S.-M. *Anal. Chem.* **2007**, *79*, 4892-4899.
- (46) Hong, S.-Y.; Park, S.-M. *J. Phys. Chem. B* **2007**, *111*, 9779-9786.

- (47) Park, J.-B.; Chang, B.-Y.; Yoo, J.-S.; Hong, S.-Y.; Park, S.-M. *Bull. Korean Chem. Soc.* **2007**, *28*, 1523-1530.
- (48) Chang, B.-Y.; Ahn, E.; Park, S.-M. *J. Phys. Chem. C* **2008**, *112*, 16902-16909.
- (49) Park, J.-B.; Park, S.-M. *J. Electroanal. Chem.* **2011**, *656*, 243-251.
- (50) Chang, B.-Y.; Park, S.-M. *J. Phys. Chem. C* **2012**, *116*, 18270-18277.
- (51) Ko, Y.; Park, S.-M. *J. Phys. Chem. C* **2012**, *116*, 7260-7268.
- (52) Yang, C. j.; Ko, Y.; Park, S.-M. *Electrochim. Acta* **2012**, *78*, 615-622.
- (53) Park, J.-Y.; Chang, B.-Y.; Nam, H.; Park, S.-M. *Anal. Chem.* **2008**, *80*, 8035-8044.
- (54) Park, J.-Y.; Lee, Y.-S.; Chang, B.-Y.; Karthikeyan, S.; Kim, K. S.; Kim, B. H.; Park, S.-M. *Anal. Chem.* **2009**, *81*, 3843-3850.
- (55) Orazem, M. E.; Tribollet, B. *Electrochemical Impedance Spectroscopy*; John Wiley & Sons, New Jersey, 2011.
- (56) Fletcher, S.; Horne, M. D. *Electrochem. Commun.* **1999**, *1*, 502-512.
- (57) Bard, A. J.; Faulkner, L. R. *Electrochemical Methods : Fundamentals and Applications*, 2nd ed.; John Wiley: New York, 2001.
- (58) Muzikář, M.; Fawcett, W. R. *Anal. Chem.* **2004**, *76*, 3607-3611.
- (59) Lee, H.-C.; Park, O. O. *Vacuum* **2006**, *80*, 880-887.
- (60) Seo, M.; Yeon, S. Y.; Yun, J.; Chung, T. D. *Electrochim. Acta* **2019**, *314*, 89-95.

2. Development of New Iontronic Platform for Biomimetic Ion-based Information Processing

2.1 Introduction

Iontronics ultimately aims at ion-based signal processing similar to that found in neurological systems, or mimicking of various biological structures such as neuronal plasma membranes, with support of ionic circuits designed to functionally control the ion flow.¹ Han *et al.* named the field iontronics and made pioneering contributions on the integration of an ionic diode on a glass microchip.² Since then, the field has evolved employing microchip devices that comprise ionic circuits based on charge-selective membranes like polyelectrolyte gels (hydrogels), for ionic information processing via diodes²⁻⁷, transistors^{5,8-10}, and logic circuits^{2,6,11}. Such tremendous advances have propelled the scientific community to aspire to the utilization of iontronic devices as replacement or facilitators of certain compromised biofunctions, such as neural circuits.^{6,7,12} Considering the desired advances toward bioinspired and biomimetic application-driven development of iontronics, its current toolbox¹³ of ionic resistors, capacitors, diodes, transistors and several other circuits would be remarkably reinforced with some technical development that could narrow down the gap between the biological system and the artificial iontronic system.

First, there are issues regarding the power source which drives the ionic circuit. As a fundamental biological signal processing unit, the neuron maintains the membrane potential by itself with its inherent chemical energy, which is unimaginable for current iontronic devices based on external electronic power

sources. All the available electronic powers must involve electrodes that should have as low interfacial resistance as possible, e.g. Ag/AgCl and Pt. This entails faradaic reactions at the electrode surface, continuously generating chemical products.² To the best of our knowledge, no entirely ionic circuitry covering electrodeless ionic power source has been reported yet. Secondly, the substrate materials for ionic circuits have been limited to some materials such as glass^{2,3,6-8}, which are quite distant from being utilized for biorelated purposes, including the construction of biomimetic devices or biocompatible interfaces with biological system, and biomimicking.

In this dissertation, we report the first example of ionic circuits driven by a miniaturized reverse electrodialysis (RED) stack without using conventional electronic power sources such as battery or potentiostat, in response to the aforementioned issues. RED provides a direct route to power generation by converting the free energy of mixing two salt solutions in different concentration, e.g. seawater and river water which are inexhaustible resources at estuaries.^{14,15} Assuming perfect permselectivity of an ion-exchange membrane (IEM), ca. 80 mV can result from preferential ion transport from seawater to river water (0.50 M and 0.017 M, respectively) when the IEM is present between those solutions. We operated the ionic diode and logic circuit on a microchip by salinity gradient power from the RED system. The voltage applied to the ionic circuit could be turned on or off, and more precisely controlled by manipulating the plastic connection tube filled with electrolyte, which is reminiscent of a variable resistor.

Subsequently, we report a novel method for the construction of ionic circuits based on charged hydrogels on a polydimethylsiloxane (PDMS) microchip. As a substrate material, PDMS is an attractive candidate due to its superior biocompatibility, optical transparency, chemical inertness, flexibility, stretchability, oxygen permeability, low fabrication cost and ease of manufacturing.¹⁶ While PDMS has been extensively used in various products, such as contact lens^{17,18} and condom lubricants¹⁹, it is a renowned material of choice for the fabrication of versatile microfluidic devices to support academic research on bioassay, bioanalytical studies, diagnostics, and miniaturized capillary electrophoresis (CE).²⁰⁻²⁴ We found a solution to the hydrophobicity and oxygen permeability challenges that strongly inhibit photopolymerization of the hydrogel inside the PDMS microchannel. Not only was the ionic diode successfully fabricated on the PDMS microchip, but it also showed a stable hydrogel-PDMS interface during the operation in electrolyte solutions similar to glass microchips. The prepared PDMS microfluidic ionic diode (PMID) exhibited superior rectifying behavior even under tensile stress, and recovered its initial performance after liberation from the stress. We also constructed an ionic regulator based on the mechanical switch that we integrated on the PDMS microchip by combining the flexibility of PDMS with the ionic circuit. The PDMS microfluidic ionic regulator (PMIR) allowed the supply of several voltage levels to the ionic circuit of interest. We demonstrated the ability of the PMIR to imitate the signal transmission at excitatory and inhibitory synapses, which suggested its potential as an iontronic information processing unit. The developed iontronic systems equipped with fully ionic characteristics and unprecedented versatility coming from the material properties advance toward biomimetic ion-based information processing, as

well as the development of ionic, flexible, and biocompatible platforms, such as wearable devices.

2.2. Experimental Section

2.2.1. Materials

Diallyldimethylammonium chloride (DADMAC), 2-acrylamido-2-methyl-1-propanesulfonic acid (AMPSA), sodium styrenesulfonate (SS), N,N'-methylenebisacrylamide (MBAAm), poly(ethylene glycol) diacrylate (PEGDA, average M_n 250), (3-mercaptopropyl)trimethoxysilane (MPTMS), (3-glycidyloxypropyl)trimethoxysilane (GPTMS), 1,2-ethanedithiol (EDT), 1,8-diazabicyclo[5.4.0]undec-7-ene (DBU), lithium phenyl-2,4,6-trimethylbenzoylphosphinate (LAP), Sylgard 184 silicone elastomer kit, sodium chloride, potassium chloride, 2-hydroxy-4'-(2-hydroxyethoxy)-2-methylpropiophenone, fluorescein sodium salt, 3-(trimethoxysilyl)propyl methacrylate (TMSMA), methanol, and Ag wire (0.5mm thick, 99.9%) were purchased from Aldrich. Selemion CMV and AMV were purchased from Asashi Glass Co., Ltd.

2.2.2. Preparation of RED stack

We manufactured a customized RED stack by mostly following the methods of M. C. Hatzell and B. E. Logan.²⁵ Briefly, silicon gaskets (~1.3 mm in thickness) were cut into a rectangular shape ($2 \times 1 \text{ cm}^2$) to provide flow path between IEMs that had a cross section area of 2 cm^2 . The silicon gaskets and IEMs as prepared were stacked up in a repetitive alternation (i.e. CEM, gasket, AEM and gasket, respectively) and then, two solution chambers for external connection to ionic circuit were attached to

the lateral ends of the stack comprising gaskets and IEMs. Two salt solutions (0.01 and 4.0M NaCl) were introduced into the RED system with a flow rate of 0.71mL/min. Typically, the RED stack generated 2.2V under those conditions.

2.2.3. Microchip fabrication

Corning 2947 precleaned slide glasses (75 mm × 25 mm, 1 mm thick, Corning, USA) were used as substrates. The slide glass was cleaned in a piranha solution (H₂SO₄:H₂O₂ = 3:1, J.T. Baker, USA) for 45 min and then rinsed with deionized (DI) water (NANOpure Diamond, Barnstead, USA) several times. After removing the moisture on the surface with an air blower, the cleaned slide glass was dehydrated on a hot plate at 200 °C for 5 min and then cooled to room temperature. The slide was then spin-coated (YS-100MD, Won Corp., Korea) with hexamethyldisilazane (HMDS; Clariant, Switzerland) at 7000 rpm for 30 s. It was then coated with a photoresist (PR; AZ4620, Clariant, Switzerland) at 7000 rpm for 30 s. After soft baking the PR on a hot plate at 100 °C for 90 s, the slide glass was cooled to room temperature and aligned under a pattern mask. The PR on the slide was exposed to UV light (365 nm) with an intensity of 21 mW cm⁻² for 13 s (MDA-4000, Midas, Korea) at AZ 400 K developer (Clariant, Switzerland) for 120 s. The slide glass was then washed with DI water, and the PR was hard-baked on a hot plate at 200 °C for 15 min. Adhesion tape was attached to the back side of the slide glass in order to protect it from the etching solution. The slide glass was etched with a 6:1 buffered oxide etch solution (J. T. Baker, USA) for 45 min at 25 °C with stirring. The etched glass was then drilled at the positions for the reservoirs with a 2 mm-diameter

diamond drill at 18000 rpm and cleaned in a piranha solution for the same duration. The pair of slide glasses were permanently attached to each other by thermal bonding. DI water between the glasses prevented the formation of air bubbles during the bonding process. The glasses were heated at 600 °C in a furnace (CRF-M15, Ceber, Korea) for 6 h at which time they were slowly cooled in the furnace to room temperature over 10 h.

2.2.4. Fabrication of polyelectrolyte ionic diode on microchip

DADMAC and AMPSA were used as the monomers to create positively and negatively charged polyelectrolytes. Before gelation, the microchannel was coated with 3-(trimethoxysilyl)propyl methacrylate (TMSMA, 0.5 %) in a methanol solution containing acetic acid (0.5 %) for 1.5 h. TMSMA acted as the linker between the polyelectrolyte and the slide glass surface. The microchannel was then cleaned with methanol. The microchannel was aligned under a mask and subsequently exposed to UV light (365 nm) with an intensity of 21 mW cm⁻² for 3.5 s (MDA-4000, Midas, Korea). After photopolymerization, the microchannel was cleaned with KCl (1 M) to remove the remaining DADMAC monomers, photoinitiator, and cross-linker (2 %). The microchip with the pDADMAC gel plug was then filled with a AMPSA (5 M) solution containing a photoinitiator (2%) and a cross-linker (2%). After fine alignment under the mask, the chip was exposed to UV light for 9 s to produce a sharp polyelectrolyte junction. The microchannel was then washed with KCl (1 M). Finally, the polyelectrolyte junction comprising pDADMAC and pAMPSA on the microchip was stored in aqueous NaCl (10 mM).

2.2.5. Connection of RED to the ionic circuit

Cloning cylinder (H 6 mm × 8 mm, Aldrich) was attached through epoxy-resin bonding at each position of reservoirs of the fabricated microchip. An end of the plastic tube (AJK00004, Tygon chemical resistant tubing, Saint-Gobain) filled with electrolyte was then inserted to the bonded cylinders, and the other end was located inside the solution reservoir of RED. The electrolyte employed for connecting and constructing ionic circuit is 10 mM NaCl solution. The whole system was constructed without any air bubble inside the connection tubes.

2.2.6. Voltage and current measurements in RED-powered ionic circuit

The whole system does not include any metallic electrode, nor an electronic instrumentation such as potentiostat for monitoring voltage and current signals in the ionic circuit. Instead, a multichannel basic data acquisition device (USB-6003, National Instruments, USA) of 16-bit resolution was utilized for voltage and current recording. As depicted in Fig. 2-1, each analog input channel was allocated for measuring a electrical potential difference between two arbitrary points. For example, the voltage generated from RED was measured by dipping two Ag/AgCl electrodes in both the reservoirs at each end of the RED. Similarly, the voltage drop across the ionic circuit was measured with the same method at analog channel 1. Meanwhile, the ionic current flowing through the circuit was indirectly calculated from the

potential drop across the electrolyte-filled connection tube whose resistance had been measured in advance. This follows simple Ohm's law (eqn (2-1)),

$$I \text{ (current)} = \frac{V_{diff}}{R_{tube}} \quad (2-1)$$

where V_{diff} and R_{tube} represent the voltage difference between two ends of a tube and its resistance. This current measuring method is possible because the resistance of an electrolyte-filled tube reaches several hundreds of $k\Omega$, whereas the conducting wire in electronic circuits is *de facto* negligible in terms of resistance. These voltage data were simultaneously acquired with sampling rate of 100 samples per second.

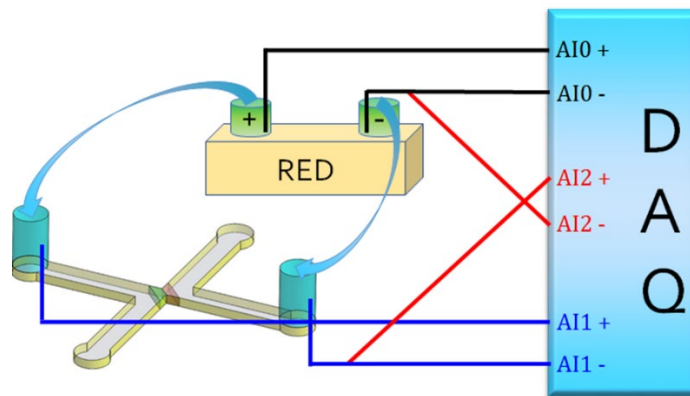


Fig. 2-1. Experimental scheme of voltage and current measurements using data acquisition (DAQ) device. AIs indicate analog input channels of the device, each pair of which is composed of + and – terminals. The electrical potential difference between these two points was recorded constantly during the experiment.

2.2.7. Optical measurement

For light-emission experiment, the fluorescence from the n-type polyelectrolyte gel, pDADMAC, was observed while the ionic circuit was driven by RED. For this purpose, aqueous NaCl solution (10 mM) containing 1 μ M of fluorescein was used as electrolyte in the ionic circuit. The fluorescence intensity was measured by a fluorescence microscope (TE2000U, Nikon, Japan).

2.2.8. PDMS microchip fabrication

PDMS microchips were fabricated by stacking two PDMS substrates, the upper one with micropattern and the lower one without any pattern. These PDMS slabs were constructed by pouring the mixture of PDMS base solution and curing agent in 10 : 1 ratio (Sylgard 184 silicone elastomer kit, Dow Corning, USA) onto the petri dish, and subsequently by curing the mixture at 65 °C for 3 h in oven, while the uncured mixture must be poured on top of the SU-8 mould for micropattern in case of the upper substrate. The SU-8 mould was fabricated by following a general photolithographic procedure on 4-inch silicon wafer (test grade, Wanxiang Silicon-Peak Electronics, China) prior to the PDMS curing step. The silicon wafer was cleaned in a piranha solution (H_2SO_4 (J.T. Baker, USA) : H_2O_2 (Daejung Chemicals & Metals, Korea) = 3 : 1) for 15 min and then rinsed with deionized (DI) water (NANOpure Diamond, Barnstead, USA) for several times. After removing the moisture on the surface with an air blower, the cleaned wafer was dehydrated on a hot plate at 150 °C for 15 min and then cooled to room temperature. The wafer was

then spin-coated (YS-100MD, Won Corp., Korea) with SU-8 (PR; SU-8 3025, Microchem, USA) at 1500 rpm for 30 s. After prebaking the sample at 95 °C for 20 min, the substrate was exposed to UV light (365 nm) with an intensity of 21 mW cm⁻² for 15 s (MDA-400M, Midas, Korea), then baked at 65 °C for 1 min and at 95 °C for 4 min as a part of post exposure bake (PEB) step. The SU-8 mould was completed by developing the wafer for 4 min with developing solution (SU-8 developer, Microchem, USA), and finally rinsing it with isopropyl alcohol (IPA) for several times.

The upper and lower PDMS substrates (thickness ~ 1 mm) were rinsed with acetone, methanol and DI water for several times. After removing the moisture on the surface, the hydrophilic activation was conducted with UV/ozone oxidation (AC6, Ahtech LTS, Korea) for 3 h while the distance between the UV lamp and the substrates was maintained to be less than 3 mm. The activated upper substrate with pattern was then silanized with 5% v/v methanol solution of MPTMS for 2 h, while the lower one with 5% v/v methanol solution of GPTMS for 2 h. After rinsing the chemically modified PDMS slabs with fresh methanol, the bonding process was finalized by pressing them against each other with ca. 40 kPa for 2 days at ambient temperature (~ 20 °C). Lastly, a 3.5% v/v methanol solution of EDT which also contains 2.5% v/v of DBU was injected into the PDMS microchannel to render thiol groups to the GPTMS-coated channel surface. After 2 h of the base-catalyzed thiol-epoxy reaction, the microchannel was rinsed with fresh methanol for several times.

2.2.9. Photopolymerization of hydrogels on PDMS microchip

DADMAC and SS were used as the monomers to create positively (n-type) and negatively (p-type) charged polyelectrolyte gels. The 4 M DADMAC monomer solution containing 2wt% of MBAAm as a cross-linker and 1wt% of LAP as a photoinitiator was used while the 1 M SS monomer solution containing 13wt% of PEGDA as a cross-linker and 1.2wt% of LAP as a photoinitiator was employed. The DADMAC precursor solution was exposed to UV light (365 nm) with an intensity of 21 mW cm^{-2} for 2 s for photopolymerization, while the SS solution 50 s. In case of the photopolymerization inside the closed PDMS microchannel, the channel was aligned under the photomask and subsequently exposed to UV light. After photopolymerization, the microchannel was cleaned with 10 mM potassium chloride (KCl, Aldrich) solution to remove the remaining gel monomers, photoinitiator, and cross-linker. This ionic circuit on PDMS microchip was filled with 10 mM KCl solution for electrical characterization as well as for storage.

2.2.10. Hydrogel stability test on two-dimensional surface under electrolyte solution

We prepared rectangular PDMS slabs ($H 1 \text{ cm} \times 1 \text{ cm}$, thickness $\sim 1 \text{ mm}$) in order to test the robustness of hydrogel-surface interface under aqueous solution. The PDMS slabs were oxidized via hydrophilic activation methods (e.g. air plasma (PDC-32G, Harrick, USA), UV/ozone oxidation), and then chemically modified. For silanization using TMSMA, the solution was prepared as 1:1:1 volume ratio

(TMSMA : AcOH : MeOH). The 10 μ l of gel monomer solution on the surface-treated PDMS slab was photopolymerized through UV exposure (365 nm) with an intensity of 21 mW cm⁻². A detailed explanation of the procedure is explained in Section 1.3.6.

2.2.11. Tensile test of PDMS microfluidic ionic diode (PMID)

The tensile test was proceeded with a tensile machine (3343, Instron, USA) with a load cell of 1 kN. Tensile rate was 0.1 mm/s. The initial length of the PMID was 10 mm as we adopted jaw phases with acrylic plates (10 mm \times 40 mm \times 1 mm) to the sample.

2.2.12. Electrical characterization of PDMS microfluidic ionic circuits

The ionic circuits constructed on PDMS microchip were filled with 10 mM KCl solution for further electrical characterization. Having located the handmade Ag/AgCl wires in the reservoirs, we performed cyclic voltammetry of ionic diode circuit from 1 V to -1 V with 2-electrode configuration, where the positive potential is defined as forward bias potential. When it comes to the demonstration of PDMS microfluidic ionic regulator (PMIR), we employed bipotentiostat (PGSTAT302N with BA module, Metrohm Autolab, Netherlands) in order to apply the two external voltages (V_1 , V_2), and to record the total ionic current (I_{tot}). The voltage applied to

the targeted part of the ionic circuit (V_{out}) was monitored by using an additional data acquisition (DAQ) board (USB-6356, National Instruments, USA) with two Ag/AgCl wires placed at the reservoirs near the part of interest of the circuit. The two voltages from the bipotentiostat were kept constant during the experiment while the change of V_{out} and I_{tot} values was observed at the moment of mechanical pressure made by a fingertip upon the switch buttons.

2.3. Results and Discussion

2.3.1. Electrical characterization of RED

For construction of the system, a miniaturized RED stack was manufactured as an ionic power source.²⁵ The RED stack generated 2.2 V with 25 IEMs, which is 62.6% of theoretical value (3.51 V). This deviation was originated from imperfect permselectivity of the IEMs and additional conducting paths created by the solution feed channels in the RED system.²⁶ A higher RED voltage can be achieved through an optimization process of the stack configuration, e.g. solution paths for feeding, thickness of solution channels between IEMs, and salt concentration ratios. Nevertheless, in this work, we could readily obtain any RED voltage required for the ionic circuit operation.

2.3.2. Ionic diode powered by RED

As shown in Fig. 2-2, we constructed an aqueous ionic diode circuit connected to RED stack through flexible, electrolyte-filled tubes involving no electronics. Both the reservoirs at the ends of the RED, the connection tubes and ionic circuits were filled with 10 mM NaCl solution containing 1 μ M fluorescein to visualize the dynamic ion flow in the ionic diode in real-time. The voltage and current responses with time were measured for forward and reverse bias states of the ionic diode. (Fig. 2-3) The experimental scheme of voltage and current measurement is presented in Fig. 2-1. Under forward bias, a voltage range of 1.4–1.6 V was imposed to the ionic diode with a current range of 0.6–0.7 μ A while the RED voltage was maintained at

2.2 V (Fig. 2-3A). The remaining voltage (0.6–0.8 V) was consumed as an IR drop by the resistive parts such as connection tubes or reservoirs. Conversely, almost entire RED voltage was applied to the ionic diode under reverse bias while the ionic current was less than 0.1 μA (Fig. 2-3B). The results imply that the resistance of ionic circuit is significantly greater under reverse bias than under forward one due to the formation of an ion depletion region.

Fig. 2-4 shows a series of temporal fluorescence images when either of the two biases is applied. Before applying forward bias potential, the n-type pDADMAC region exhibits a strong fluorescence because of the presence of anionic fluoresceins. When the diode is under forward bias, the fluoresceins in pDADMAC are gradually replaced by colorless Cl^- ions from the reservoir which contribute more efficiently to the forward ionic current with simultaneous reduction of fluorescence intensity. In contrast, the darkened pDADMAC gel starts to quickly recover its initial fluorescence intensity under reverse electrical bias as Cl^- ions inside are substituted with larger fluoresceins. We also conducted an additional experiment in order to examine the net effect of the reverse bias over no bias on the recovery of fluorescence intensity in the pDADMAC gel (Fig. 2-5). This comparative experiment under confirms that the fluorescence intensity change is mainly affected by the reverse bias. Although the diode gradually brightens without any electrical bias, the speed of fluorescence recovery is significantly greater in the presence of reverse bias voltage. These results show that the aqueous ionic circuit can be successfully embodied with combination of the ionic power of RED.

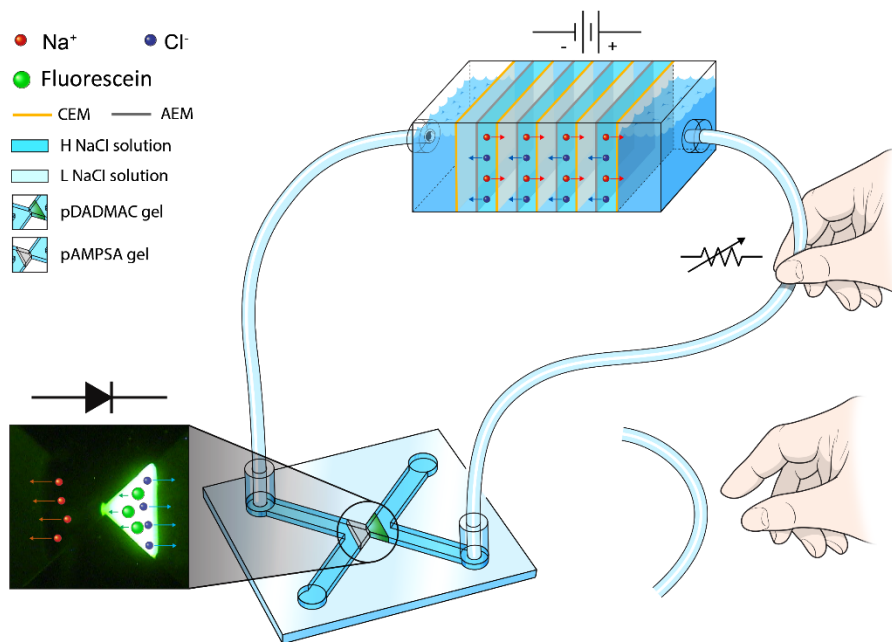


Fig. 2-2. Illustrative schematic of ionic circuit powered by RED. Voltage generated from RED is applied to microfluidic polyelectrolyte diode directly via tubes filled with electrolyte. (CEM: Cation exchange membrane, AEM: Anion exchange membrane, H(L) NaCl solution: High(low) concentration NaCl solution)

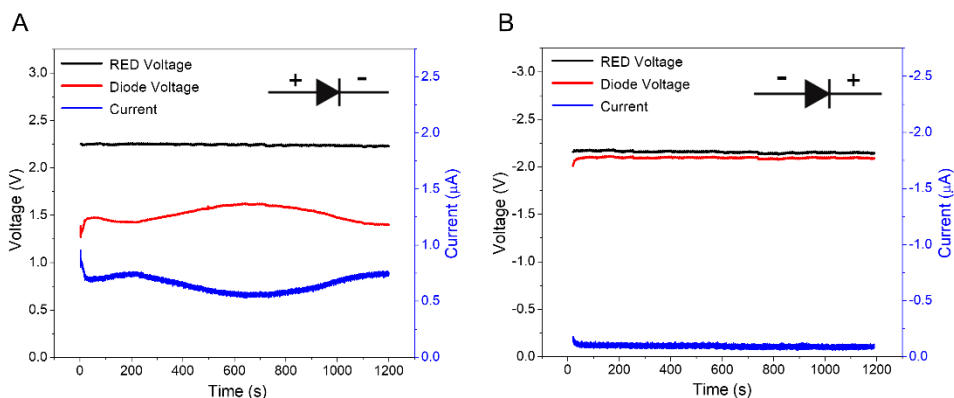


Fig. 2-3. Time vs. voltage and ionic current plot of RED-powered ionic diode under (A) forward bias, and (B) reverse bias voltage. Note that the sign of voltage and current is inversed under reverse bias condition. (Black solid line: voltage generated from RED, Red solid line: voltage drop across the diode, Blue solid line: ionic current)

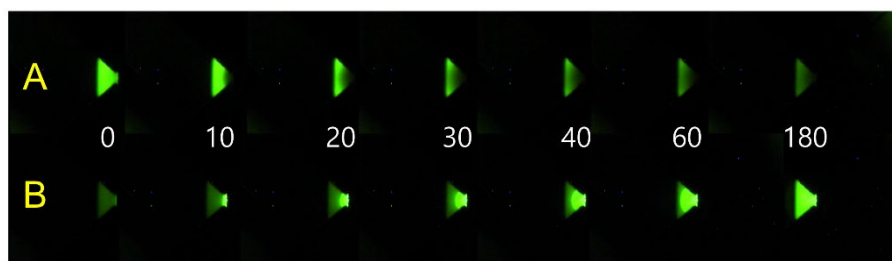


Fig. 2-4. Temporal fluorescence images of n-type pDADMAC gel in ionic diode using anionic fluorescein under (A) forward bias potential, and (B) reverse bias potential. The white numbers in the middle of each pair of images represent the elapsed time in second after connection of RED to the circuit.

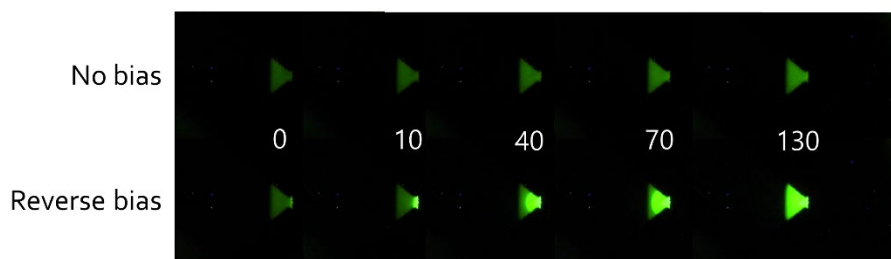


Fig. 2-5. Comparison between temporal fluorescence images of pDADMAC gel under no external bias and reverse bias potential. The white numbers in the middle of each pair of images indicate the elapsed time in second from the initial state.

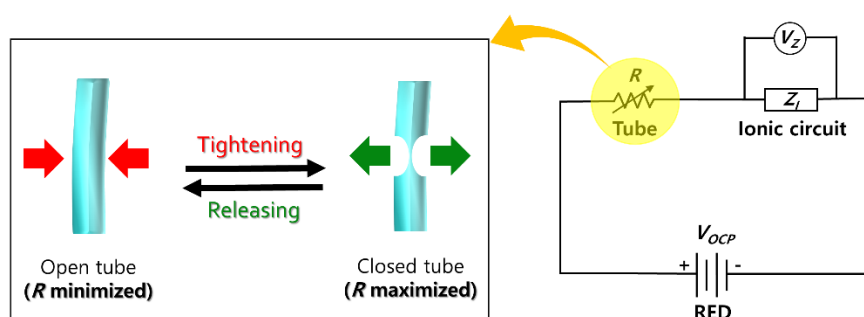


Fig. 2-6. Comparison between temporal fluorescence images of pDADMAC gel under no external bias and reverse bias potential. The white numbers in the middle of each pair of images indicate the elapsed time in second from the initial state.

2.3.3. Voltage switching and regulation upon ionic circuit

The flexible connection tube filled with electrolyte solution plays dual roles: (1) connection of the RED to the ionic circuit, which is analogous to the conducting wire in electronics, and (2) a variable resistor when tightened or released at a specific point as described in Fig. 2-6. Because the material resistance is inversely proportional to its cross section, the resistance of connection tube increases when it is constricted, and decreases when released. Thus, the voltage applied to the circuit is maximized when the tube is completely open whereas almost no voltage is applied when the tube is fully tightened. We measured voltage and current responses upon the pressure imposed to the tube for the forward- and reverse-biased ionic diode while the whole voltage from RED was almost kept constant at approximately 2.5 V (Fig. 2-7). Under forward bias, about 1.7 V was applied to the diode with a distinct current value ($> 1.0 \mu\text{A}$) when the tube was in the released state (Fig. 2-7A). However, when the tube was completely tightened, the applied voltage and current were drastically dropped to nearly zero. This phenomenon was reproducibly observed depending on the tube states. A similar result is shown in Fig. 2-7B for reverse-biased ionic diode. In this case, the majority of the RED voltage (approx. 2.45 V) was applied to the diode while the tube was open, since the resistance of the circuit ($> 20 \text{ M}\Omega$) is extremely higher than the other rest parts in the circuit ($\sim 400 \text{ k}\Omega$) (e.g. reservoirs, electrolyte) by orders of magnitude. However, the applied voltage and ionic current dropped to nearly zero due to the infinitely increased tube resistance when the tube was fully constricted.

An arbitrary potential beyond the only on and off states can be also applied to the ionic diode in a more controlled manner. For example, 6 different potentials including on and off states were applied to forward-biased ionic diode by precisely controlling the magnitude of the pressure onto the tube (Fig. 2-8). The steady-state ionic currents are directly proportional to the voltage drops across the circuit. The corresponding fluorescence images are in good agreement in that the fluorescence intensity gradually decreases with increasing applied voltage. These results demonstrate that we can tune the voltage applied to ionic circuits by using a variable-resistor-like tube filled with aqueous solution. As for reverse bias, only on and off states were allowed regardless of the magnitude of tube pressure. Neither voltage between the two states was stably maintained. The tube resistance should surpass that of the circuit to adjust the potential applied to the diode even under reverse bias, which can reach several hundreds of $M\Omega$ according to the electrochemical impedance spectroscopy (EIS) analysis in the previous report.³ More precise and delicate tools such as automatic micrometers and microvalves would enable finer control of the tube resistance to apply an arbitrary potential to any ionic circuit.

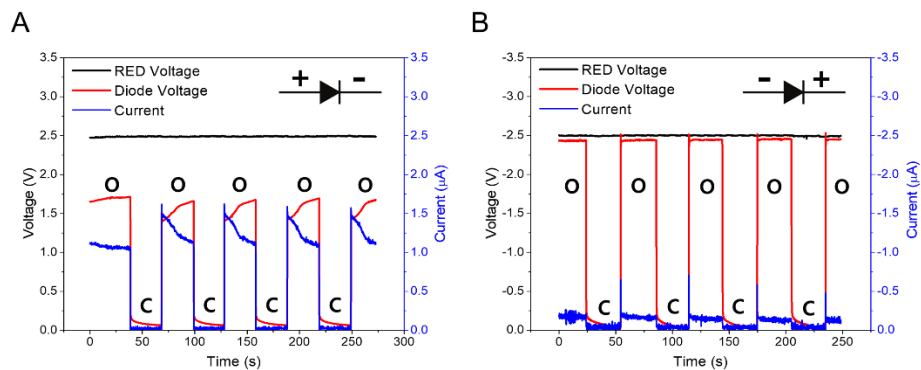


Fig. 2-7. Time vs. voltage and ionic current plot for repetitive voltage switching upon ionic diode through mechanical pressure on flexible connection tube filled with electrolyte under **(A)** forward, and **(B)** reverse bias condition. The bold O and C on the graph indicate the open(on) and closed(off) tube states, Note that the sign of voltage and current is inversed under reverse. (Black solid line: voltage generated from RED, Red solid line: voltage drop across the diode, Blue solid line: ionic current)

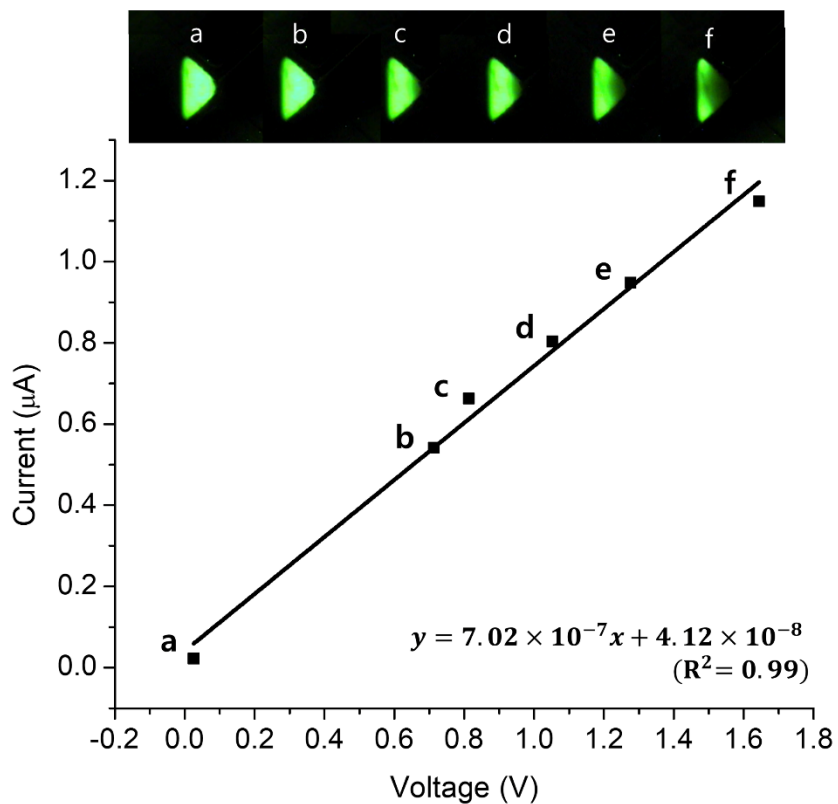


Fig. 2-8. I - V plot for forward-biased ionic diode at steady state with fluorescence images of n-type pDADMAC gel for each state during the voltage adjustment. The voltage drop across the circuit (V) and ionic current (I) were measured 120 s after steady state had been formed.

2.3.4. Ionic OR gate driven by RED

The concept of RED-powered iontronic system can be further expanded to a more sophisticated aqueous ionic circuit. Fig. 2-9A shows an integrated microfluidic OR logic circuit composed of two ionic diodes in parallel. We obtained the truth table (Fig. 2-9B) of the circuit with fluorescence images using fluorescein (Fig. 2-9C), and output voltages for each state. The applied voltage becomes '0' (off-state, low voltage) or '1' (on-state, high voltage) as each tube is tightened or released at a specific point. The experimental results are in accordance with that of general digital OR gate in electronics in that the output voltage, which is defined as a voltage drop upon the circuit, reaches '1' state when either of the two inputs is on '1'. When using anionic fluorescein for imaging the system, the fluorescence intensity in n-type pDADMAC phase markedly decreases in forward-biased ('1' state) state. Consequently, RED in aqueous media can supply power to a more elaborate information processor in microfluidic chip.

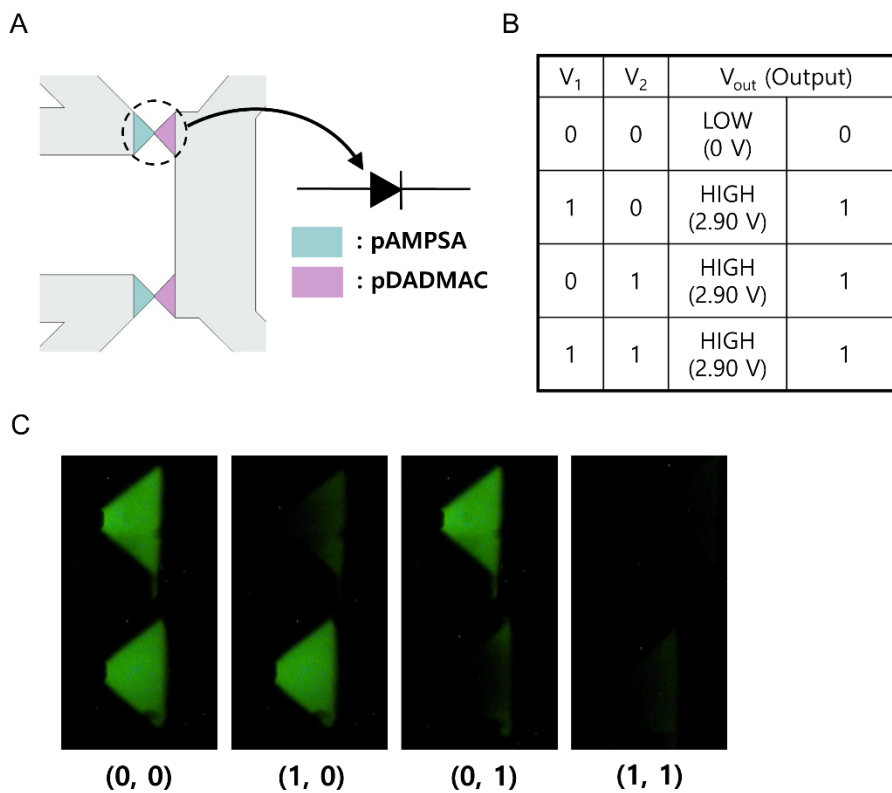


Fig. 2-9. (A) Microchip pattern of ionic OR logic circuit, (B) Truth table of the voltages from RED and output signals from the circuit, (C) Fluorescence images for each state of the logic gate. Input voltage from RED was maintained at 3.1 V.

2.3.5. Preparation of PDMS microchip for subsequent hydrogel formation

Despite its similarity in appearance to glass substrate, the hydrophobicity and oxygen permeability of PDMS greatly hinders the fabrication of hydrogel-based ionic circuits on PDMS microchips. In the case of glass microchip, the hydrogel formed typically by UV photopolymerization can be covalently linked to the microchannel surface chemically treated with 3-(trimethoxysilyl)propyl methacrylate (TMSMA), which is a widely used linker (Fig. 2-10 and 2-11).^{2,3,6-8} Not only do the gel monomers polymerize with each other upon exposure to UV, they can also be linked covalently to the methacrylate groups at the channel surface. In contrast, the robust anchoring of hydrogels on the PDMS-microchannel surface requires certain prerequisites, which are not necessary for such fabrication on the glass microchip. First, the microchannel surface should be sufficiently hydrophilic for the injection of gel monomer solution and electrolyte. On the other hand, the surface should also be chemically modified at the same time to enable the firm attachment of the photopolymerized hydrogel onto the channel via covalent bonds, while mitigating gel swelling or desorption upon filling the channel with the aqueous solution during the device operation. The radical scavenging effect of the oxygen diffused into the PDMS microchannel should also be overcome. In addition, the pair of PDMS slabs, with and without micropattern, must be tightly bonded during the fabrication procedure.

In this work, we introduced thiol groups (-SH) onto the PDMS surface to facilitate subsequent UV-mediated thiol-ene reactions with the double bonds of the gel

monomer molecules, as described in Scheme 2-1. The radical-driven thiol-ene reaction is a well-known click reaction in organic chemistry for more than a century and has been considered as an alternative of the classical photopolymerization reactions based on (meth)acrylates for several applications, including surface coating, material fabrication and photolithography owing to the high sensitivity of the (meth)acrylic monomers to radical inhibition caused by oxygen.²⁷⁻²⁹ To coat the inner channels of the PDMS microchip with thiol groups, we began by performing hydrophilic activation of the PDMS surface by UV/ozone oxidation over a long duration (3 h) (Scheme 2-1A, B). Next, the activated silanol groups of the patterned PDMS slab were treated with (3-mercaptopropyl)trimethoxysilane (MPTMS), while those of the unpatterned PDMS slab with (3-glycidyloxypropyl)trimethoxysilane (GPTMS), for 2 h in methanol (Scheme 2-1B, C). Inspired by the similar bonding method reported by Hoang *et al.*, who had achieved irreversible bonding between Kapton (Dupont, Wilmington DE) and PDMS substrates³⁰, we adopted the novel thiol-epoxy click reaction (epoxide ring-opening) for strong PDMS-PDMS bonding. The two chemically functionalized substrates were mechanically pressed against each other (~ 40 kPa) and left at ambient temperature for 2 days, which yielded a sturdily bonded PDMS microchip reminiscent of the strong PDMS-PDMS adhesion achieved by oxygen plasma treatment (Scheme 2-1C, D). Lastly, we injected a methanol solution containing 1,2-ethanedithiol (EDT) and 1,8-diazabicyclo[5.4.0]undec-7-ene (DBU) into the PDMS microchannel to coat the thiol groups onto the GPTMS-treated bottom substrate (Scheme 1D, E). The base-catalyzed epoxide ring-opening reaction at this stage ensures the presence of the thiol groups on all sides of the PDMS-microchannel surface. The MPTMS-treated

substrate on the top may not be affected by the nucleophilic thiolate owing to the absence of any reactive electrophilic functional group.

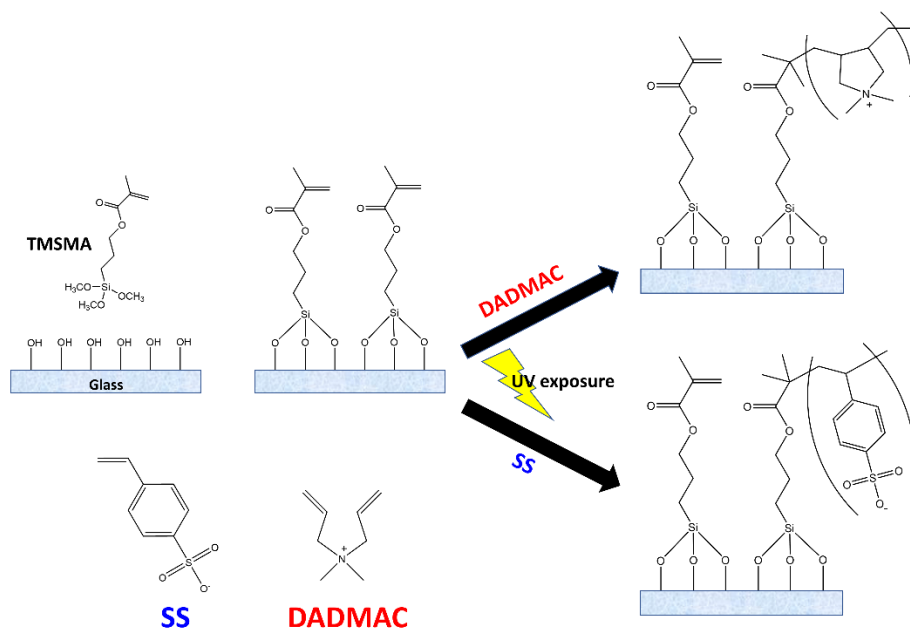


Fig. 2-10. Surface anchoring reaction between the hydrogel monomers and the methacrylate groups on the TMSMA-coated glass substrate with presence of UV illumination.

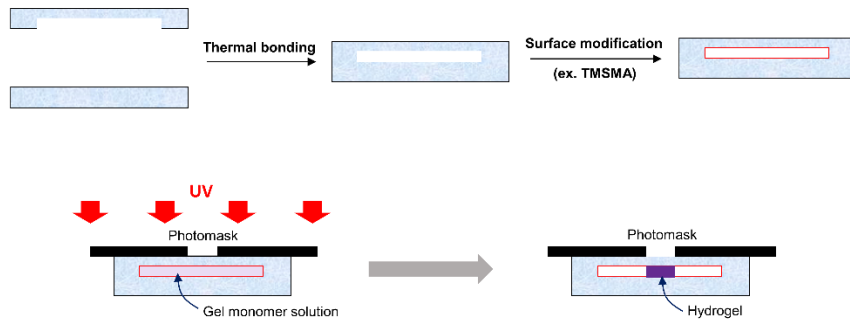
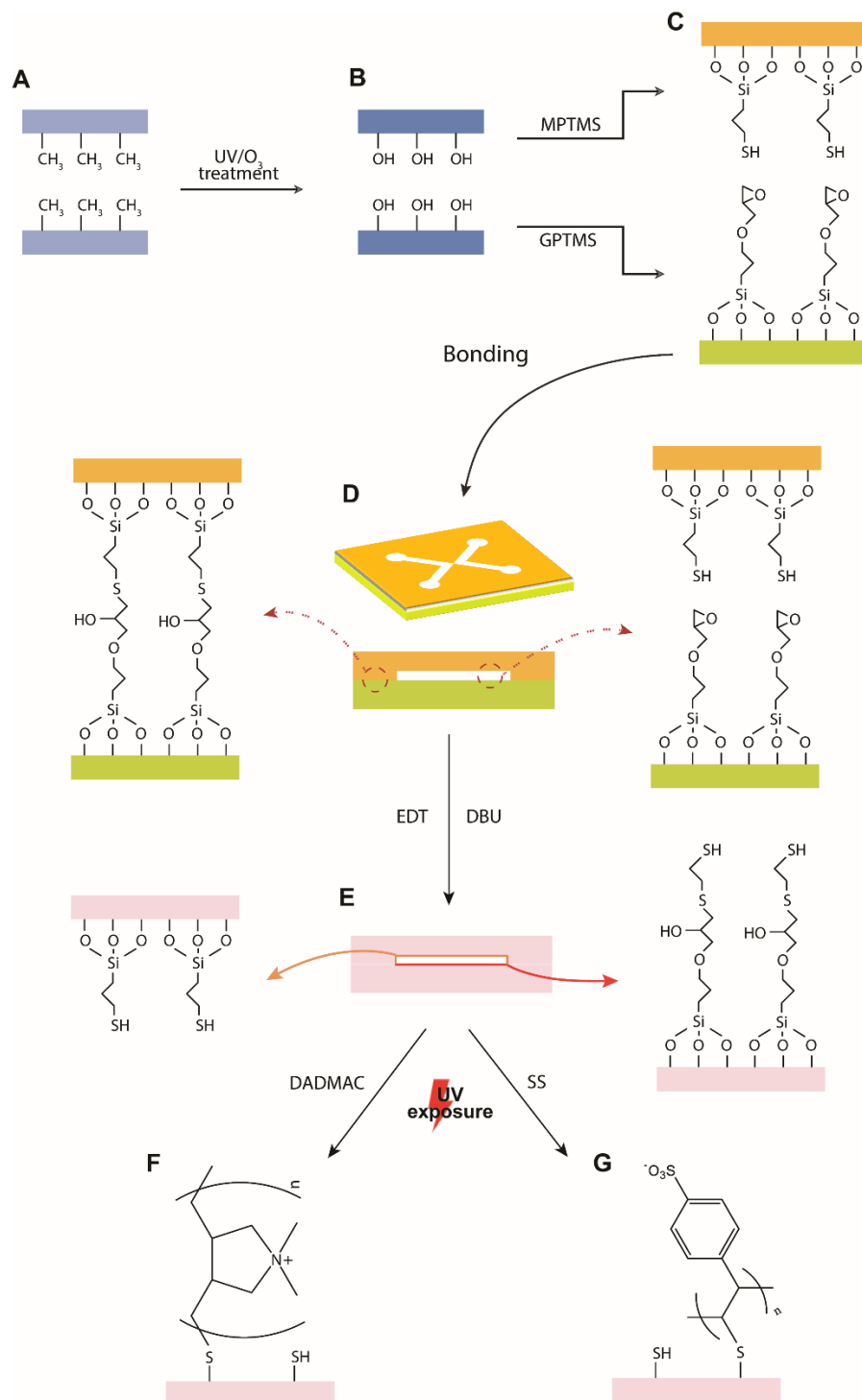


Fig. 2-11. General fabrication procedure of the hydrogel-based ionic circuit in glass microfluidic chip via UV-mediated photopolymerization in combination with a photomask.



Scheme 2-1. Step-by-step reaction scheme for preparation of PDMS microchip. **(A)** Initial pristine PDMS substrates, **(B)** substrates after hydrophilic activation using 3

h of UV/ozone oxidation and **(C)** surface silanizations using MPTMS and GPTMS for the top and the bottom substrates, respectively. **(D)** Robustly bonded PDMS microchip after 2 days of thiol-epoxy click reaction mediated by mechanical pressure. (Inset: Chemical structure of PDMS-PDMS interface and channel surface marked with dashed circle) **(E)** Final PDMS microchip; microchannel surface is entirely modified with thiol functional groups after 2 h of base-catalyzed thiol-epoxy reaction with injection of methanol solution containing 1,2-ethanedithiol (EDT) and 1,8-diazabicyclo[5.4.0]undec-7-ene (DBU). (Inset: Chemical structure of the inner microchannel surfaces) Chemical structures of **(F)** pDADMAC-anchored, and **(G)** pSS-anchored microchannel surfaces.

2.3.6. Validation of robustness of hydrogel-PDMS interface in aqueous environment

Prior to the desired hydrogel formation on the PDMS microchip, as shown in Scheme 2-1E to G, we validated the effectiveness of our surface modification method by performing the hydrogel adhesion test on the two-dimensional PDMS surfaces that were chemically modified. As described in Fig. 2-12A, we first dropped 10 μ l of gel monomer solution on the substrate surface that had been already chemically modified (e.g. hydrophilic activation, silanization, etc). After the gel photopolymerization upon UV exposure, we injected a sufficient amount of 10 mM KCl (aq) on top of the hydrogel. Subsequently, we removed the electrolyte after 3 min of immersion so as to confirm whether the hydrogel formed was firmly attached to the surface without noticeable swelling. If the hydrogel is strongly attached to the surface, the swelling occurs only effectively toward the vertical direction, as depicted in Fig. 2-12B, when immersed in electrolyte. Because the hydrogel is still firmly fixed on the surface even after removing the electrolyte, it cannot move along the surface, which implies the validity of the corresponding surface modification. In contrast, the gel starts to swell into the global direction as soon as placed in electrolyte in the absence of sufficient adhesion between the hydrogel and surface, as displayed in Fig. 2-12C. Due to the lack of interaction between the gel and surface, the swollen gel can freely move along the whole surface, which signifies the ineffectiveness of the surface treatment method used.

Notably, the hydrogels were robustly attached to the PDMS surface that was functionalized according to Scheme 2-1A to E, even under an aqueous environment.

The results depicted in Fig. 2-13 show that the poly(diallyldimethylammonium chloride) (pDADMAC) and poly(styrenesulfonate) pSS gels were stably attached to the surface without noticeable swelling toward the horizontal direction when immersed in the electrolyte. These results signify the validity of our surface functionalization methods employed for the preparation of the PDMS microchip. The attached gels could not move freely along the surface owing to the strong surface adhesion even with the use of an aqueous solution, which is similar to the hydrogel polymerized on the TMSMA-coated glass substrate. The photopolymerized hydrogels tightly bound to the surface were neither destroyed nor fractured even when the PDMS substrate was bent (Fig. 2-14).

Another related approach worthy of consideration is a more facile and straightforward use of oxygen (air) plasma treatment for the robust PDMS-PDMS bonding and hydrophilic activation of PDMS surface, followed by the chemical modification of the silanol groups for a stable hydrogel anchoring.^{23,31-33} However, the hydrogels photopolymerized on the PDMS surface in such an approach of plasma treatment followed by chemical modifications (e.g. TMSMA, MPTMS), exhibited swelling in the electrolyte because of their poor adhesion (Fig. 2-15). It should be noted that the swollen gels were displaced from their initial center positions in the electrolyte owing to their facile movement on the surface due to the lack of adhesion. As displayed in Fig. 2-16, we also found that the hydrogels formed on the PDMS substrate obtained from relatively short duration (< 1 h) of UV/ozon oxidation and the subsequent chemical modification did not display strong adhesion to the surface under aqueous environment, and were similar to the results presented in Fig. 2-15. This is not surprising considering that a hydrophilic silica-like (SiO_x) layer, the

thickness of which is in the order of tens of nm, starts to form near the PDMS surface owing to the prolonged UV/ozone treatment which lasts for more than 1~2 h.³⁴⁻³⁷ This SiO_x layer has been reported to resist water and gas permeation, which could be additionally beneficial for overcoming the radical inhibition by oxygen diffused into the PDMS channel. We verified a strong hydrogel-PDMS surface linkage just as shown in Fig. 2-13 by using the PDMS substrates prepared over the long duration (> 3 h) of UV/ozone oxidation followed by surface silanization with TMSMA and MPTMS (Fig. 2-17). Nevertheless, this method is only viable for attaching hydrogels to open (two-dimensional) PDMS surfaces due to the absence of adequate PDMS-PDMS bonding during the surface modification procedure. Once fabricated by certain PDMS-PDMS bonding methods, it is difficult to further modify the inner microchannel surfaces of PDMS microchip by UV/ozone oxidation, because both the 254 and 185 nm wavelengths of the UV/ozone photochemical reaction hardly penetrate the PDMS substrate.^{38,39}

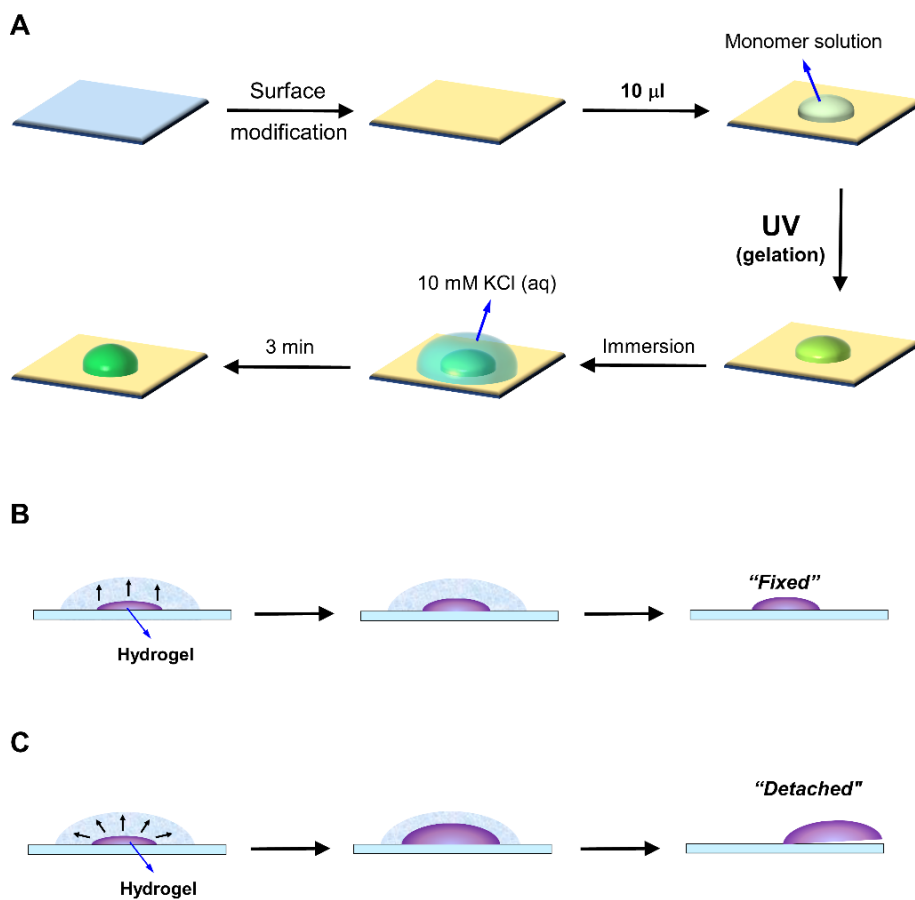


Fig. 2-12. (A) Brief scheme of hydrogel stability test under aqueous condition of the hydrogel photopolymerized on the open PDMS surface, which is chemically modified. Volume of gel monomer (precursor) solution was controlled at 10 µl. As fabricated hydrogel was immediately immersed in 10 mM KCl (aq) for 3 min. Simplified illustration of (B) hydrogel robustly attached onto the surface, and (C) hydrogel without effective adhesion to the surface, in electrolyte solution.

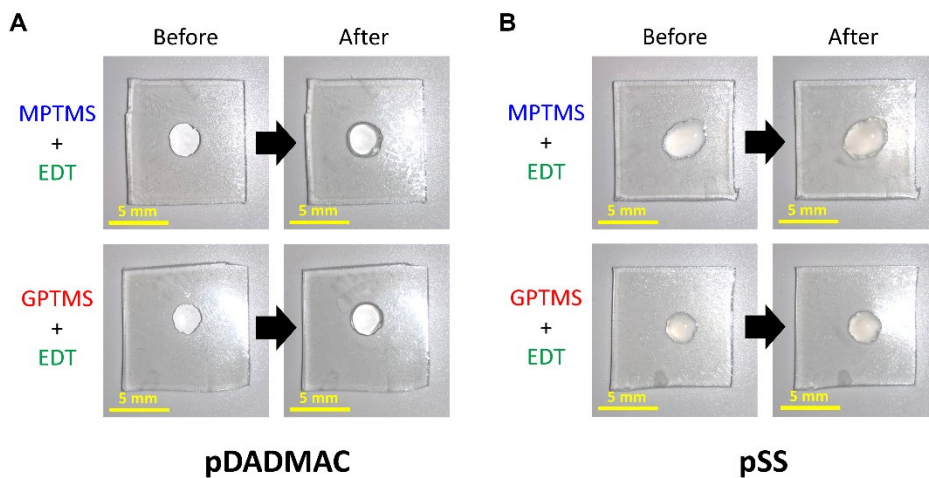


Fig. 2-13. Photographs of (A) pDADMAC and (B) pSS gels formed on PDMS substrates prepared by following the surface modification procedures depicted in Scheme 2-1A to E. Top and bottom rows indicate whether the PDMS substrate was treated with MPTMS or GPTMS after the UV/ozone oxidation stage in Scheme 2-1A and B. (left column: hydrogels as photopolymerized, right column: after the gel stability test procedure)

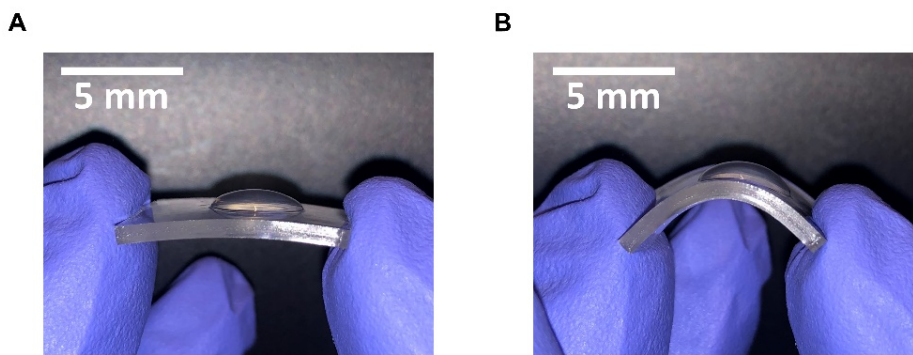


Fig. 2-14. (A) Photograph of the pDADMAC gel photopolymerized on the PDMS surface that was chemically modified by following the consecutive procedures enumerated in Scheme 2-1A to E; i) UV/ozone oxidation 3 hr, ii) MPTMS (in MeOH) treatment 2 hr, iii) 2 days at room temperature, and iv) EDT/DBU (in MeOH) treatment 2 hr. (B) Photograph of the bended hydrogel-PDMS hybrid in (A).

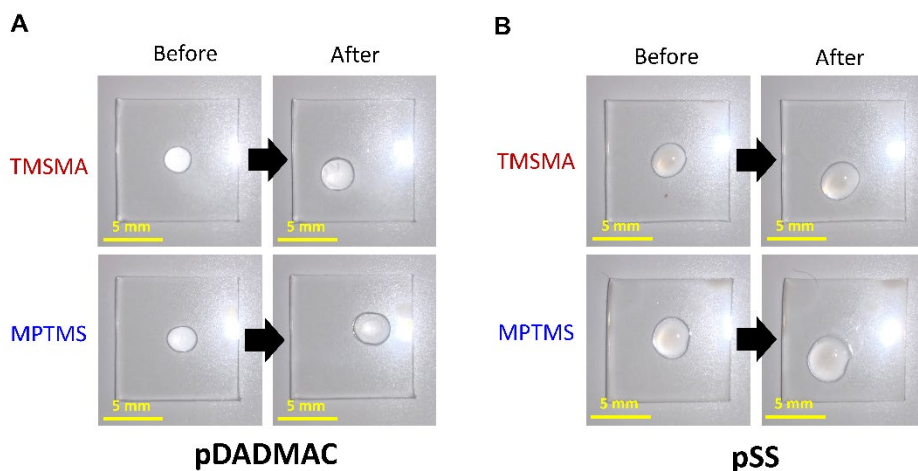


Fig. 2-15. Photographs obtained from the hydrogel stability test of **(A)** the pDADMAC and **(B)** pSS gels formed on PDMS substrates prepared by following the series of treatments: i) air plasma 1.5 min, and ii) silanization (TMSMA or MPTMS) 2 hr. The top and bottom rows indicate whether the PDMS substrate was treated with TMSMA or MPTMS after the plasma treatment. (left column: hydrogels as photopolymerized, right column: after the gel stability test procedure)

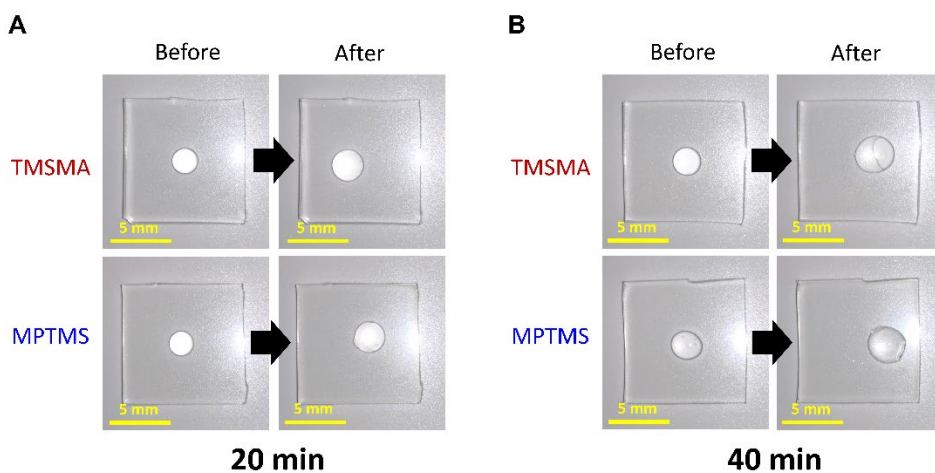


Fig. 2-16. Photographs obtained from the hydrogel stability test of the pDADMAC gels formed on PDMS substrates prepared by following the series of treatments: i) UV/ozone oxidation (**A**) 20 min or (**B**) 40 min, and ii) silanization (TMSMA or MPTMS) 2 hr. The top and bottom rows indicate whether the PDMS substrate was treated with TMSMA or MPTMS after the UV/ozone oxidation. (left column: hydrogels as photopolymerized, right column: after the gel stability test procedure)

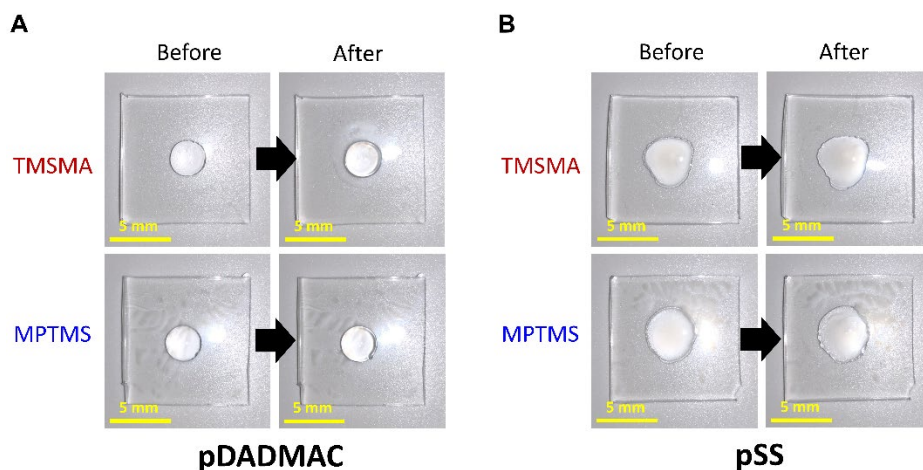


Fig. 2-17. Photographs obtained from the hydrogel stability test of **(A)** the pDADMAC and **(B)** pSS gels formed on PDMS substrates prepared by following the series of treatments: i) UV/ozone oxidation 3 hr, and ii) silanization (TMSMA or MPTMS) 2 hr. The top and bottom rows indicate whether the PDMS substrate was treated with TMSMA or MPTMS after the UV/ozone oxidation. (left column: hydrogels as photopolymerized, right column: after the gel stability test procedure)

2.3.7. Flexible and stretchable ionic diode on PDMS microchip

The procedure described in Scheme 2-1 allowed us to successfully fabricate the ionic diode circuit on a PDMS microchip through UV-assisted photopolymerization of pDADMAC and pSS hydrogels, as depicted in Fig. 2-18A. This X-shaped design is identical to that reported in our previous works, and the bipolar membrane composed of the p-type (pSS) and n-type (pDADMAC) polyelectrolytes conducts the ionic current primarily in one direction under forward bias potential.^{2,3,6,7} The performance of the prepared PMID was equivalent to that on the glass microchip in terms of hysteresis, and a superior current rectification ratio of 16.10 was obtained (Fig. 2-18B), where the rectification ratio is defined as a ratio of the two current values at the end potentials, which were 1 V and -1 V in this case. The cyclic voltammograms of the PMID with different scan rates were acquired (Fig. 2-18C) to verify the predicted characteristics of the diode. With the increase of the scan rate, the position of the reverse peak potential gradually moved toward the negative potential because of the time required for the depletion of the previously accumulated ions at the junction under forward bias³, which caused the low rectification ratio. In addition, we confirmed the long-term storage stability of our PMID by observing the shape of the CV, and that the rectification ratio was satisfactorily retained for more than a month, as presented in Fig. 2-19.

Next, we examined the performance of our PMID under uniaxial stretching as well as that after recovery from the applied strain. As displayed in Fig. 2-20A, the PMID was subjected to tensile stress by mounting the PMID on the tensile machine. The

strain was applied at a constant rate of 0.1 mm/s until the device fractured. The stress-strain curve in Fig. 2-20B shows that the fracture occurred when the strain level reached approximately 35% after a smooth increase of the tensile stress. As shown in Fig. 2-21, the device fracture originated across the reservoir holes, indicating that the mechanical properties of the perforated PDMS substrate are the limiting factors that affect the device durability rather than those of the hydrogels. We acquired the cyclic voltammograms of the PMID that was subjected to the 10, 20, and 30% strain, and that after recovery (no applied strain) (Fig. 2-20C) to examine their electrical characteristics. As shown in Figure 2-20D, the initial rectification ratio decreased with increasing tensile strain, and the device regained its initial performance immediately after liberation from the applied strain. The magnitude of the ionic current upon reverse bias around -1 V increased with the tensile strain (Fig. 2-20C). The decreased rectification ratio upon stretching is due to the deformation of the hydrogels at the junction, which could bring about the attenuation of the ion depletion effect. However, it appears that this level of tensile stress is negligible and insufficient to cause permanent destruction of hydrogels or desorption from the channel surface to prevent the remediation of the device performance.

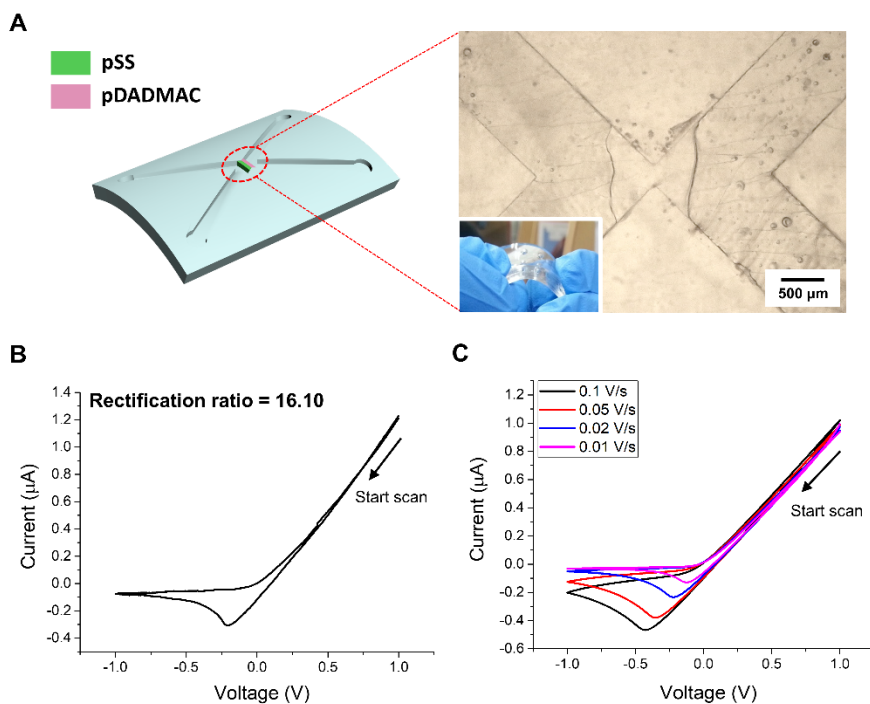


Fig. 2-18. (A) Schematic illustration of a PDMS microfluidic ionic diode (PMID) composed of pSS and pDADMAC hydrogels. (Inset: optical microscope image of the diode junction with a photograph of the bended PMID) (B) Cyclic voltammogram of the PMID as fabricated. (scan rate = 10 mV/s, rectification ratio = 16.10) (C) Cyclic voltammograms of the PMID with varying scan rates; 0.1, 0.05, 0.02 and 0.01 V/s. Black arrows in (B) and (C) indicate that the voltage sweep started from 1.0 V toward negative potential. Solution filled inside the PMID was 10 mM KCl (aq).

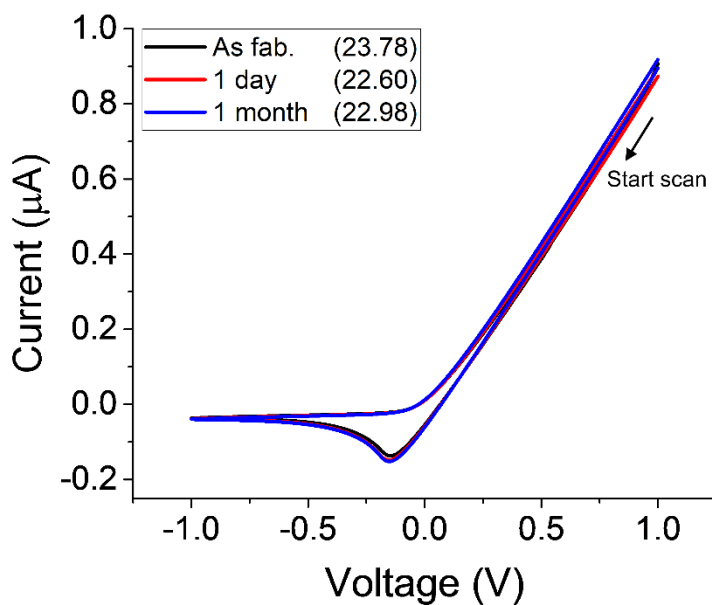


Fig. 2-19. Cyclic voltammograms of a PMID measured immediately (black solid line), 1 day (red solid line), 1 month (blue solid line) after the fabrication. The rectification ratios were 23.78, 22.60, 22.98, respectively. The solution filled inside the PMID was 10 mM KCl (aq). (Scan rate = 10 mV/s)

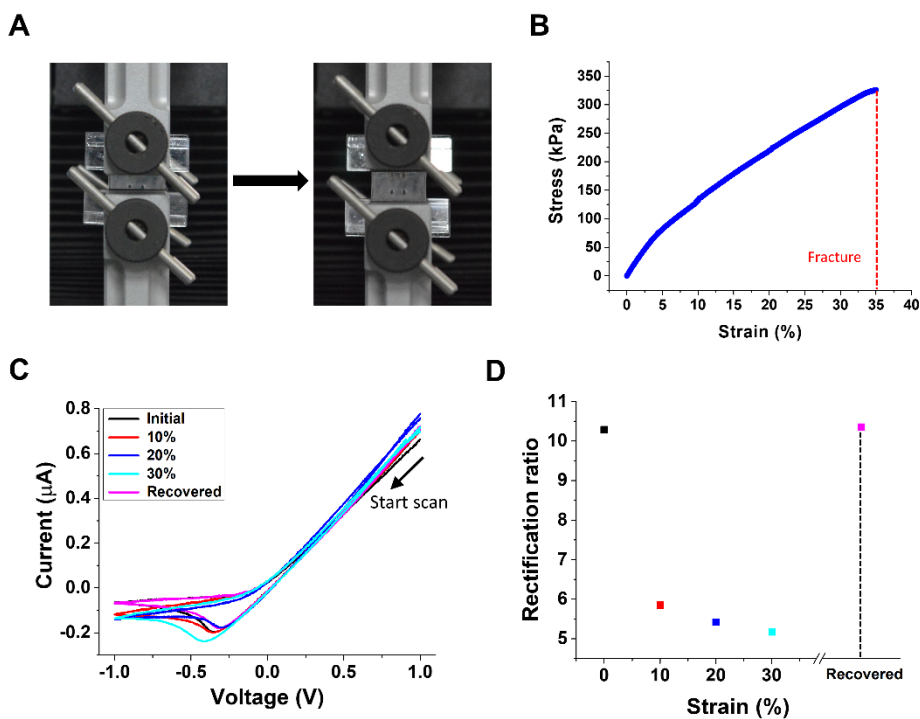


Fig. 2-20. (A) Photographs of the PMID before and after elongation, and (B) PMID stress-strain curve. (C) Cyclic voltammograms measured at several stretched states of the PMID; initial (0%), 10%, 20%, 30%, and recovered state. (D) Rectification ratio values for each diode CV in (C); 10.29 (initial, black), 5.85 (10%, red), 5.42 (20%, blue), 5.17 (30%, cyan), and 10.35 (recovered, magenta). Solution filled inside the PMID was 10 mM KCl (aq). (Scan rate = 20 mV/s)

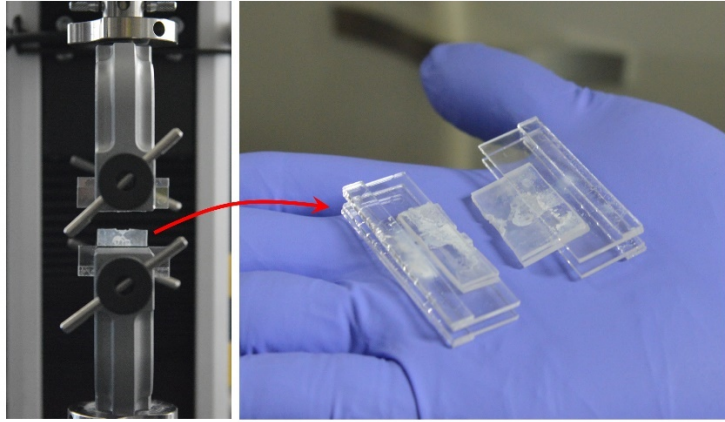


Fig. 2-21. Photographs of the ruptured PMID after the tensile test.

2.3.8. PDMS microfluidic ionic regulator (PMIR) based on mechanical switch

The elasticity and flexibility of the PDMS suggest opportunities for expanding the potentiality of the hydrogel-based PDMS microfluidic ionic circuits (PMI). To investigate such a possibility, we designed an ionic device that can regulate the voltage level applied to an ionic circuit of interest via mechanical switching without the need to vary the input voltages. First, we constructed a push-button type switch on the PDMS microchip, as depicted in Fig. 2-22A. The round button connected to the microchannel is hollow due to its enclosed structure with no reservoir holes. Thus, air can be pushed into the microchannel by pressing the switch button, which renders the ionic circuit electrically open. Fig. 2-22B shows that the ionic current flowing through PDMS microchannel filled with the electrolyte can be reproducibly turned on or off with the elastic switch, which is reminiscent of the switching function of the electrolyte-filled plastic tube reported in our previous work.⁶ We then integrated this mechanical air-switch onto the PDMS microchip to fabricate the PDMS microfluidic ionic regulator (PMIR) (Fig. 2-23A). The V_{out} generated from the combination of the two external voltages (i.e. V_1 and V_2) and the switch state of S_1 and S_2 is to be applied to the ionic circuit marked with dashed blue rectangle, which can be also seen as the total output load for the PMIR.

Having fabricated the PMIR, we investigated its ability to mimic the characteristics of signal transmission at the biological synaptic junctions in an iontronic manner (Fig. 2-23B). In the nervous system, the external stimulus causes depolarization of the neuronal membrane potential, which propagates the action

potential to the presynaptic bouton.⁴⁰ The identical presynaptic action potential triggers excitatory postsynaptic current and potential (EPSC and EPSP, respectively) at the excitatory synapses, whereas the inhibitory postsynaptic current and potential (IPSC and IPSP, respectively) are created at the inhibitory synapses. The total summation of those PSPs exceeding the threshold level yields an action potential in the postsynaptic neuron. In this hydrogel-based mimicry on the PDMS microchip, a mechanical pressure imposed upon the switches S_1 and S_2 on PMIR acts as the input stimulus. The resulting voltage and current output are delivered to the pair of antiparallel diodes, which serve as the ionic circuitry that mimics the postsynaptic bouton. The diodes are intended to prevent the mixing of the ionic species between the presynaptic and postsynaptic areas at the resting state or when the device is turned off. Again, their antiparallel arrangement is of great importance in that it can express both the positive (excitatory) and negative (inhibitory) outputs to the postsynaptic circuitry. The use of a single diode would not enable the postsynaptic response under reverse bias potential, but would act to just block the current, which could be problematic in terms of postsynaptic signal summation or subtraction. The signals, such as the postsynaptic response recorded during the PMIR operation in Fig. 2-23C, show that the V_{out} and I_{tot} were nearly zero at the resting state without any pressure upon S_1 and S_2 when V_1 and V_2 were 1 V and -2 V, respectively. This is ascribed to the symmetrical design of the two microchannels connected to S_1 and S_2 (see Fig. 2-24 and Table 2-1). Upon pressing down S_1 to open it, we observed an instant outcome in V_{out} and I_{tot} of approximately -0.3 V and -0.4 μ A, respectively, which is reminiscent of the inhibitory operation on the postsynapse, similar to the IPSP and IPSC in neural systems. In contrast, the PMIR gave the excitatory responses with the

same intensity of V_{out} and I_{tot} of positive polarity at the moment when S_2 was opened, which resonates with EPSP and EPSC. The voltages supplied to the PMIR, V_1 and V_2 , could also be regarded as a synaptic weight in respect of synaptic plasticity because the magnitudes of V_{out} and I_{tot} are proportional to them when $V_2 = -2V_1$ (see Fig. 2-24 and Table 2-2).⁴¹ One can thus even aspire to the construction of an array of PMIRs bearing neuromimetic features, as basic hardware units for ionic information processing. The interconversion between several voltage levels across the targeted ionic circuit resembles the neuronal plasma membrane, whose membrane potential originates from the electrochemical equilibrium between the intracellular and extracellular concentrations of the ionic species on the basis of their discriminative membrane permeabilities.⁴⁰ The membrane potential fluctuates between the negative resting state and positive depolarized state because the permeability of K^+ and Na^+ ions can rapidly and functionally change owing to the ion channels and active transporters. Similarly, the output voltage level from the PMIR in this study varies instantaneously with switch operations. If an electrical potential generated from the PMIR is to be applied across an ionic circuitry with extremely high resistance, such as the biological lipid bilayer membrane, the V_{out} will be independent of other resistive components in the device, i.e. channel resistance, and could be maintained with negligible ionic current leakage (see Fig. 2-24 and Table 2-1). Likewise, the PMIs offer rich possibilities for materializing iontronic analogs of biological systems once the corresponding circuit is designed and constructed appropriately.

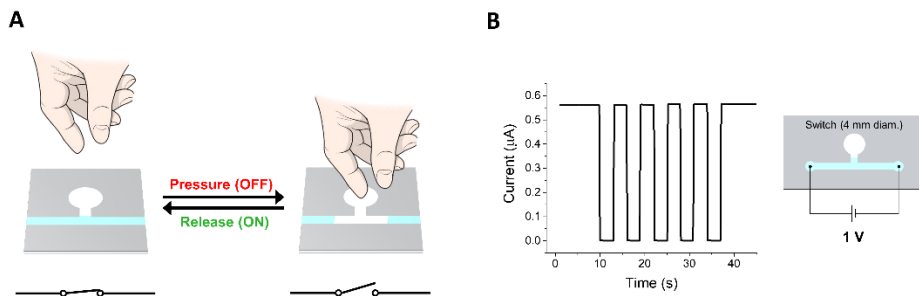


Fig. 2-22. (A) Schematic illustration of the working principle of mechanical pressure-based switch integrated on PDMS microchip. (B) Ionic current recorded under constant voltage (= 1 V) applied to the PDMS microchannel with ca. 3 s of five switch actions. The microchannel was filled with 10 mM KCl solution. The channel length and width were 16 mm and 1.3 mm, respectively. The inset image represents the PDMS microchip used for the test.

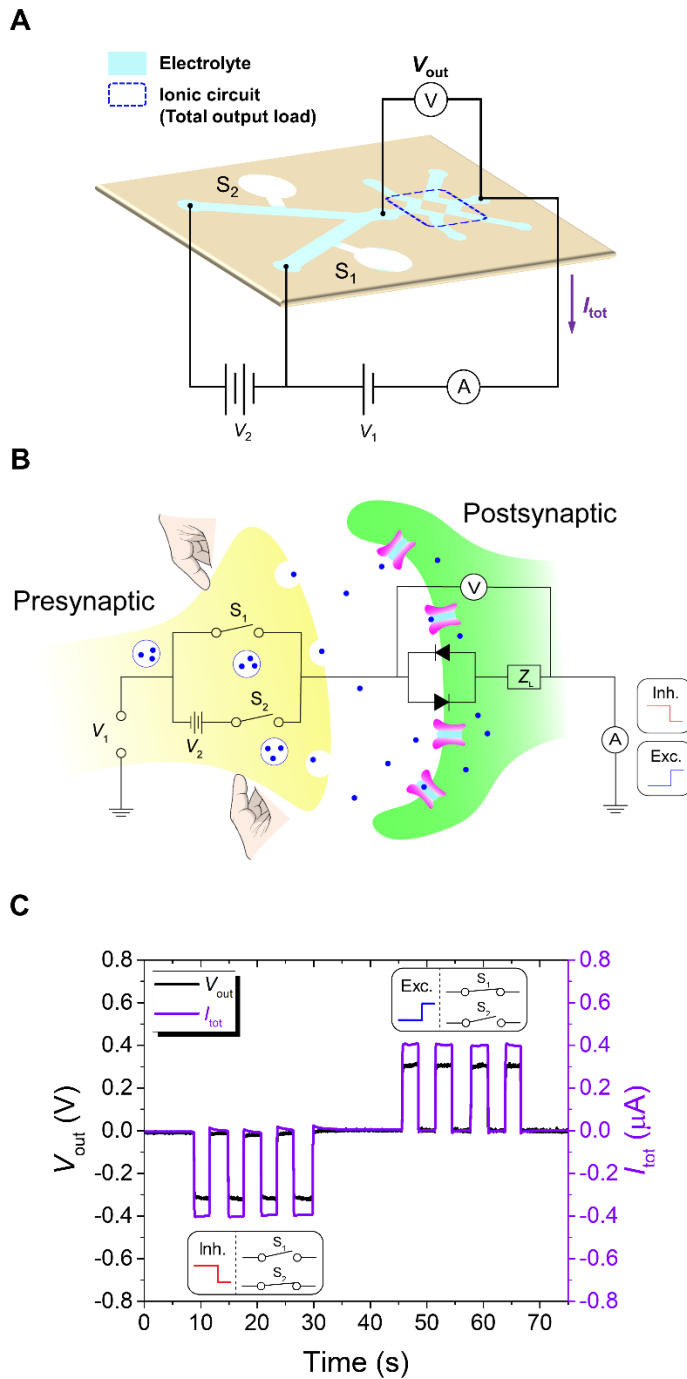


Fig. 2-23. (A) Schematic illustration of the PDMS microfluidic ionic regulator (PMIR) device. Area marked with blue dashed rectangle indicates an ionic circuit of interest to be driven by PMIR. S_1 and S_2 represent the ionic switch for each

corresponding microchannel. V_1 and V_2 are two external voltages, V_{out} the voltage applied to the targeted ionic circuit, and I_{tot} the total ionic current. **(B)** Conceptual illustration of iontronic synaptic signal transmission triggered by external mechanical pressure imposed upon switches S_1 and S_2 on PMIR. Circuit diagram represents the antiparallel diodes and succeeding output load (Z_L) driven by PMIR. **(C)** V_{out} and I_{tot} recorded with individual switch operation. Duration of each switch action was approximately 3 s. V_1 and V_2 were maintained at 1.0 V and -2.0 V, respectively.

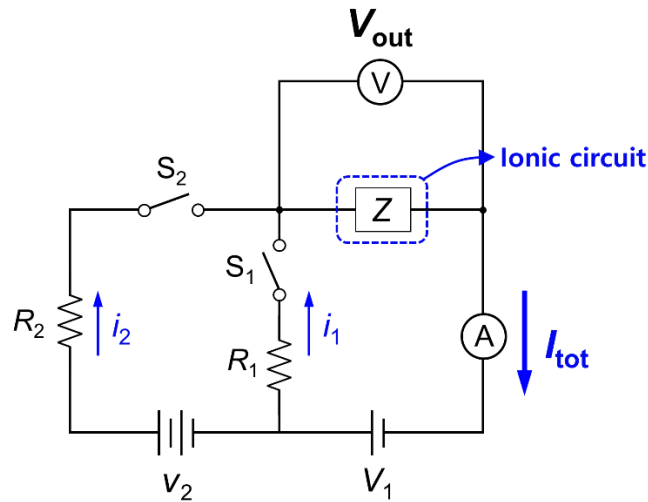


Fig. 2-24. Full equivalent circuit diagram of the PMIR device presented in Fig. 2-23A. R_1 and R_2 indicate the resistances of the two microchannels connected to each input voltage, respectively. S_1 and S_2 represent the mechanical ionic switches, Z the total resistive component of the ionic circuit of interest, V_{out} the voltage drop across Z , i_1 and i_2 the partial ionic currents flowing through R_1 and R_2 , respectively, I_{tot} the total ionic current flowing through Z .

(S ₁ , S ₂)	(1, 1)		(0, 1)		(1, 0)	
	$R_1 = R_2 = R$	$Z \gg R$	$R_1 = R_2 = R$	$Z \gg R$	$R_1 = R_2 = R$	$Z \gg R$
V_{out}	$\frac{Z}{R + 2Z}(2V_1 + V_2)$	$V_1 + \frac{1}{2}V_2$	$\frac{Z}{R + Z}(V_1 + V_2)$	$V_1 + V_2$	$\frac{ZV_1}{R + Z}$	V_1
I_{tot}	$\frac{2V_1 + V_2}{R + 2Z}$	0	$\frac{V_1 + V_2}{R + Z}$	0	$\frac{V_1}{R + Z}$	0

Table 2-1. V_{out} and I_{tot} values when $R_1=R_2=R$, or Z is excessively greater than R ($=R_1=R_2$) in Fig. 2-24.

(S ₁ , S ₂)	(1, 1)		(0, 1)		(1, 0)	
	$R_1 = R_2 = R$					
	$V_2 = nV_1$	$V_2 = -2V_1$	$V_2 = nV_1$	$V_2 = -2V_1$	$V_2 = nV_1$	$V_2 = -2V_1$
V_{out}	$\frac{(n + 2)ZV_1}{R + 2Z}$	0	$\frac{(n + 1)ZV_1}{R + Z}$	$\frac{-ZV_1}{R + Z}$	$\frac{ZV_1}{R + Z}$	
I_{tot}	$\frac{(n + 2)V_1}{R + 2Z}$	0	$\frac{(n + 1)V_1}{R + Z}$	$\frac{-V_1}{R + Z}$	$\frac{V_1}{R + Z}$	

Table 2-2. V_{out} and I_{tot} values when $R_1=R_2=R$, and $V_2=nV_1$ in Fig. 2-24.

2.4. Conclusion

In this dissertation, we report significant advances in the development of iontronic devices that render them even more versatile, biofriendly, and more relevant than ever. We actualized the iontronic system composed of aqueous ionic circuits powered by an ionic power source, the RED, without any metallic compound. For demonstration, we fabricated the ionic diode and OR logic circuit connected to the RED through electrolyte-filled plastic tubes. This new, fully ionic platform is of importance in that this can make sensing and stimulating perfectly free from faradaic reaction at electrode surface. Being a proof-of-concept without much sophistication yet, the proposed system would suggest various applications where an aqueous, ionic, and non-metallic power source are required such as a bioinspired information processor just like the neuron. With regard to our newly developed PDMS microfluidic ionic circuit (PMI), it allows us to realize an ion-based signal processing device on soft elastomeric material with many advantageous properties, such as biocompatibility, flexibility, and transparency. Having exploited prolonged UV/ozone oxidation, a series of chemical treatments involving silanization and thiol-ene click reaction, and a novel PDMS-PDMS bonding method, we successfully fabricated the stretchable PMID, which showed superior rectification performance and long-term stability. We also accomplished the fabrication of a mechanical pressure-driven ionic switch on PDMS microchip and designed a PMIR, that was capable of driving the ionic circuit of interest with several voltage and current levels. The PMIR proved to be a suitable hardware unit for mimicking biological signal processing by demonstrating its ability to serve as an iontronic analog of the synaptic

transmission at the excitatory and inhibitory synapses, which was initiated from the external pressure on the switches as the input stimulus. Besides applications to ionic devices, our novel PDMS surface functionalization method of PDMS surface could also be beneficial for achieving a rigid hydrogel-PDMS interface under an aqueous environment for applications relevant to material chemistry or engineering. The proposed hydrogel-based iontronic system on PDMS microchip is an excellent example of the convergence of ionic circuits and soft materials for enabling unprecedented advances.

The researches in iontronics during the past decades have been too immature to be conceived as an ‘information processor’ that conforms to the ultimate directionality of the field, which leaves us a lot to achieve. The Venn diagram displayed in Fig. 2-25 shows the primary features that constitute the current iontronics: ionic circuitry composed of hydrogels, iontronics powered by RED, and various options for device material. It is expected that new ion-based devices or platforms equipped with information processing ability could appertain to the overlapped areas of the Venn diagram. The RED part of the Fig. 2-2 could be integrated onto the microchip to be an active iontronic device just like the neuron, which could further be constructed with PDMS taking advantage of its biocompatibility. Apart from the ionic power or material variation, the ionic circuit itself would evolve developing its non-linearity (i.e. memristive behavior, device plasticity) in combination with signal processing features (i.e. signal summation). Further, those kinds of ‘iontronic’ neural circuits could be interfaced to the actual biological system allowing bilateral communication and replacement of certain neurological functions.

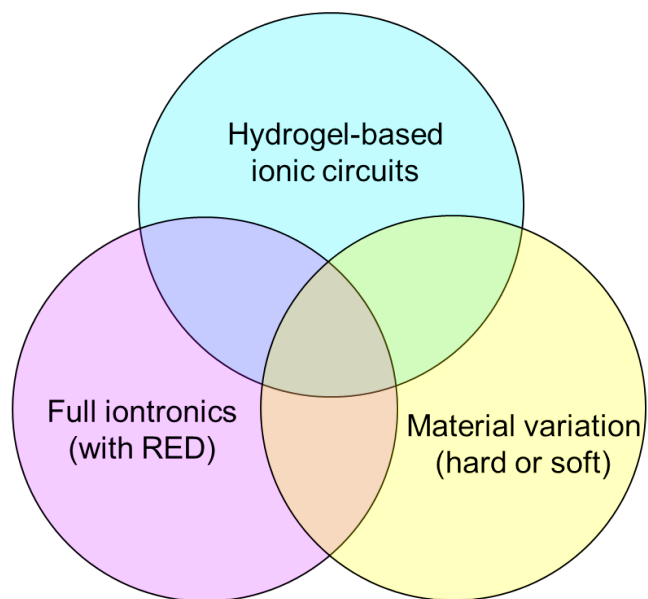


Fig. 2-25. Primary features of current iontronics expressed as a Venn diagram.

2.5. References

- (1) Chun, H. G.; Chung, T. D. *Annu. Rev. Anal. Chem.* **2015**, *8*, 441-462.
- (2) Han, J. H.; Kim, K. B.; Kim, H. C.; Chung, T. D. *Angew. Chem. Int. Ed.* **2009**, *48*, 3830-3833.
- (3) Han, J. H.; Kim, K. B.; Bae, J. H.; Kim, B. J.; Kang, C. M.; Kim, H. C.; Chung, T. D. *Small* **2011**, *7*, 2629-2639.
- (4) Gabrielsson, E. O.; Janson, P.; Tybrandt, K.; Simon, D. T.; Berggren, M. *Adv. Mater.* **2014**, *26*, 5143-5147.
- (5) Sun, G.; Senapati, S.; Chang, H. C. *Lab Chip* **2016**, *16*, 1171-1177.
- (6) Han, S. H.; Kwon, S.-R.; Baek, S.; Chung, T.-D. *Sci. Rep.* **2017**, *7*, 14068.
- (7) Lim, S.-M.; Yoo, H.; Oh, M.-A.; Han, S. H.; Lee, H.-R.; Chung, T. D.; Joo, Y.-C.; Sun, J.-Y. *Proc. Natl. Acad. Sci. U.S.A.* **2019**, *116*, 13807-13815.
- (8) Kim, K. B.; Han, J.-H.; Kim, H. C.; Chung, T. D. *Appl. Phys. Lett.* **2010**, *96*, 143506.
- (9) Tybrandt, K.; Larsson, K. C.; Richter-Dahlfors, A.; Berggren, M. *Proc. Natl. Acad. Sci. U.S.A.* **2010**, *107*, 9929-9932.
- (10) Tybrandt, K.; Gabrielsson, E. O.; Berggren, M. *J. Am. Chem. Soc.* **2011**, *133*, 10141-10145.
- (11) Tybrandt, K.; Forchheimer, R.; Berggren, M. *Nat. Commun.* **2012**, *3*, 871.
- (12) Arbring Sjöström, T.; Berggren, M.; Gabrielsson, E. O.; Janson, P.; Poxson, D. J.; Seitanidou, M.; Simon, D. T. *Adv. Mater. Technol.* **2018**, *3*, 1700360.
- (13) Janson, P.; Gabrielsson, E. O.; Lee, K. J.; Berggren, M.; Simon, D. T. *Adv. Mater. Technol.* **2019**, *4*, 1800494.

- (14) Veerman, J.; Saakes, M.; Metz, S.; Harmsen, G. *J. Membr. Sci.* **2009**, *327*, 136-144.
- (15) Post, J. W.; Veerman, J.; Hamelers, H. V.; Euverink, G. J.; Metz, S. J.; Nijmeijer, K.; Buisman, C. J. *J. Membr. Sci.* **2007**, *288*, 218-230.
- (16) McDonald, J. C.; Duffy, D. C.; Anderson, J. R.; Chiu, D. T.; Wu, H.; Schueller, O. J.; Whitesides, G. M. *Electrophoresis* **2000**, *21*, 27-40.
- (17) Nicolson, P. C.; Vogt, J. *Biomaterials* **2001**, *22*, 3273-3283.
- (18) Kim, J.; Kim, M.; Lee, M.-S.; Kim, K.; Ji, S.; Kim, Y.-T.; Park, J.; Na, K.; Bae, K.-H.; Kyun Kim, H.; Bien, F.; Young Lee, C.; Park, J.-U. *Nat. Commun.* **2017**, *8*, 14997.
- (19) Tottey, L. S.; Coulson, S. A.; Wevers, G. E.; Fabian, L.; McClelland, H.; Dustin, M. *J. Forensic. Sci.* **2019**, *64*, 207-217.
- (20) Ng, J. M.; Gitlin, I.; Stroock, A. D.; Whitesides, G. M. *Electrophoresis* **2002**, *23*, 3461-3473.
- (21) Sia, S. K.; Whitesides, G. M. *Electrophoresis* **2003**, *24*, 3563-3576.
- (22) Fujii, T. *Microelectron. Eng.* **2002**, *61*, 907-914.
- (23) Duffy, D. C.; McDonald, J. C.; Schueller, O. J.; Whitesides, G. M. *Anal. Chem.* **1998**, *70*, 4974-4984.
- (24) Makamba, H.; Kim, J. H.; Lim, K.; Park, N.; Hahn, J. H. *Electrophoresis* **2003**, *24*, 3607-3619.
- (25) Hatzell, M. C.; Logan, B. E. *J. Membr. Sci.* **2013**, *446*, 449-455.
- (26) Vermaas, D. A.; Saakes, M.; Nijmeijer, K. *Environ. Sci. Technol.* **2011**, *45*, 7089-7095.
- (27) Hoyle, C. E.; Bowman, C. N. *Angew. Chem. Int. Ed.* **2010**, *49*, 1540-1573.

- (28) Posner, T. *Berichte der Deutschen Chemischen Gesellschaft* **1905**, *38*, 646-657.
- (29) Cramer, N. B.; Bowman, C. N. *J. Polym. Sci. Pol. Chem.* **2001**, *39*, 3311-3319.
- (30) Hoang, M. V.; Chung, H.-J.; Elias, A. L. *J. Micromech. Microeng.* **2016**, *26*, 105019.
- (31) Owen, M. J.; Smith, P. J. *J. Adhes. Sci. Technol.* **1994**, *8*, 1063-1075.
- (32) Duffy, D. C.; Schueller, O. J.; Brittain, S. T.; Whitesides, G. M. *J. Micromech. Microeng.* **1999**, *9*, 211.
- (33) Zhou, J.; Ellis, A. V.; Voelcker, N. H. *Electrophoresis* **2010**, *31*, 2-16.
- (34) Oláh, A.; Hillborg, H.; Vancso, G. J. *Appl. Surf. Sci.* **2005**, *239*, 410-423.
- (35) Ouyang, M.; Yuan, C.; Muisener, R.; Boulares, A.; Koberstein, J. *Chem. Mater.* **2000**, *12*, 1591-1596.
- (36) Ouyang, M.; Muisener, R.; Boulares, A.; Koberstein, J. *J. Membr. Sci.* **2000**, *177*, 177-187.
- (37) Hillborg, H.; Tomczak, N.; Oláh, A.; Schönherr, H.; Vancso, G. J. *Langmuir* **2004**, *20*, 785-794.
- (38) Quici, N.; Vera, M. L.; Choi, H.; Puma, G. L.; Dionysiou, D. D.; Litter, M. I.; Destailats, H. *Appl. Catal. B-Environ.* **2010**, *95*, 312-319.
- (39) Lee, J.; Kim, J.; Kim, H.; Bae, Y. M.; Lee, K.-H.; Cho, H. J. *J. Micromech. Microeng.* **2013**, *23*, 035007.
- (40) Purves, D. *Neuroscience*, 3rd ed.; Sinauer Associates, Sunderland, Massachusetts, 2004.

(41) Brunel, N.; Hakim, V.; Richardson, M. J. *Curr. Opin. Neurobiol.* **2014**, *25*, 149-155.

국문초록

전기화학은 기본적으로 용액 내의 화학종과 전극 간의 전하 전달과 그로 인해 발생하는 일련의 화학적 변화를 다루는 학문이다. 뿐만 아니라 물리적, 전기적, 혹은 구조적인 변화이더라도 관심 대상의 시스템에 어떠한 방식으로든 전기화학적 영향을 주는 현상들이라면 전기화학의 탐구 대상이 될 수 있다. 이러한 이유로 전기화학은 센서, 배터리, 연료 전지, 부식, 도금 등의 분야 뿐 아니라 외견상으로 그다지 화학적이지 않은 현상들까지도 폭넓게 연관 지어질 수 있다. 본 논문에서는 상당히 이질적인 두 가지의 연구에 대해 보고함으로써 상기 언급된 범용성과 다양성을 지닌 전기화학이라는 학문의 잠재력을 조금이나마 논해보고자 한다. 먼저, Part 1에서는 푸리에 변환 전기화학 임피던스 분광법을 실시간 및 *in situ* 분석법으로 활용한 사례에 대해 보고한다. Part 2는 전하를 띤 하이드로젤 기반으로 작동하는 이온트로닉스 시스템 및 소자의 비약적인 발전과 그를 통한 차세대 생체 모방 정보 처리 소자로서의 가능성에 대해 서술한다.

Part 1: 푸리에 변환 임피던스법의 전기화학적 분석법으로의 활용

전기화학 시스템의 실시간, *in situ* 분석을 위한 새로운 접근법으로서, 우리는 스텝-전위를 사용하는 푸리에 변환 전기화학 임피던스 분광법 (이하 FT-EIS)을 활용하였다. 본 연구에서는 염화제이철-염산 기반의

식각액에 의한 인듐-주석 산화물 박막의 화학적 식각 과정을 분석 대상으로 채택하였으며, 이 과정은 실제로 수많은 리소그래피 공정에서 널리 사용되기도 한다. 전하 전달 저항과 축전 성분과 같은 등가 회로 파라미터들을 FT-EIS 분석을 통해 성공적으로 추적함으로써, 식각 과정 중의 일시적인 활성화 현상 및 식각 과정의 종료 등을 모니터링 하였다. FT-EIS 측정 데이터들은 추가적으로 헥사시아노철(II 및 III)산칼륨을 이용한 전기화학 분석, FESEM 이미징, 에너지 분산형 X 선 분광법, X 선 회절 분석법 등을 통해 뒷받침되었다. 추가적으로 위 기법을 통해 보다 섬세한 구조의 교차형 마이크로패턴을 보다 고품질, 그리고 재현적으로 얻어내는데 활용하였다. FT-EIS 는 매순간 전극의 전기화학적 순간 이미지들을 포착할 수 있다는 기법이라는 점에 그 의의가 있다. 따라서 본 연구는 비단 전극의 식각 과정 뿐 아니라 지속적이고 급격하거나 예측되지 않는 변화를 보이는 수많은 현상들에 모두 유용하게 쓰일 수 있는 FT-EIS 의 가능성을 제고시키는 중요한 사례로 볼 수 있을 것이다.

Part 2: 생체모방형 이온 기반 정보 처리를 위한 새로운 이온트로닉스 플랫폼의 개발

‘Ion (이온)’과 ‘Electronics (전자 공학)’으로부터 새로이 만들어진 Iontronics (이하 이온트로닉스)는 수용액 기반 이온 회로를 통해 생체 시스템과 같이 이온 기반으로 이루어지는 정보 처리 방식을 궁극적으로 지향한다. 하지만, 이온 다이오드, 축전기, 트랜지스터 및 논리 회로를

포함하는 현재까지의 이오닉(이온트로닉) 소자들은 실제 생체 시스템과 여러 차이가 존재했으며, 소자 제작에 쓰이는 재료 측면에서도 그 한계점이 존재하였다. 본 논문에서, 우리는 위 한계점을 효과적으로 극복한 두 가지의 기술적 진보에 대해 다룬다. 첫째로는, 역전기투석 소자를 전원으로 사용하여 최초로 어떠한 금속 전극, 외부 배터리 등을 사용하지 않고 이온 회로를 구동하였다. 이는 실제 생체 시스템은 물과 이온만으로도 스스로 에너지를 생산하며, 그를 이용해 전기 신호를 처리한다는 사실에 착안한 것이다. 우리는 역전기투석 소자를 활용하여 성공적으로 이온 다이오드를 구동하였고, 회로와 전원을 연결하는 전해질 튜브를 조작하여 스위치 혹은 가변 저항으로 활용할 수 있음을 보였다. 더 나아가, OR 논리 회로를 완전히 이온과 전해질로만 구동함으로써 보다 정교한 이온트로닉 소자로서의 가능성을 확인했다. 더 나아가, 저항이나 다이오드와 같은 수동형 이오닉 소자 뿐 아니라 그 자체로 에너지를 지닌 능동형 이오닉 소자의 구현 및 차후 생체 모방형 정보 처리 소자로서의 발전 가능성을 확인하였다. 두 번째로, 본 논문에서는 하이드로젤 기반의 이오닉 소자를 Polydimethylsiloxane (이하 PDMS)로 이루어진 마이크로칩 기판에 구성하는 방법을 최초로 보고한다. 장시간의 자외선/오존 산화법, 화학적 실란화를 통한 PDMS 기판 표면 처리법, 그리고 싸이올-에폭시 반응을 통한 새로운 PDMS 기판 간의 본딩법을 사용하여 성공적으로 하이드로젤과 PDMS 기판 간의 안정적인 결합을 얻어낼 수 있었다. 이렇게 제작된 하이드로젤은

마이크로칩 내에 수용액과 함께 존재할 때에도 부풀거나 탈착되지 않고 장시간 안정적으로 유지되어 이온닉 소자로 작동할 수 있음을 확인하였다. PDMS 마이크로칩 기판에 형성한 이온 다이오드는 훌륭한 정류 성능을 보였으며, 소자 신축성과 함께 장기간의 보관 가능성까지도 확인하였다. 다음으로, 우리는 PDMS 마이크로칩 상에 스위치를 구현하고, 이를 기반으로 이온 레귤레이터 회로를 구성하였다. 이 소자를 통하여 우리는 최초로 실제 생체 내의 흥분성 및 억제성 시냅스에서 나타나는 신호 전달 양상을 이온트로닉 플랫폼에 모방할 수 있었다. 본 연구를 통해 우리는 투명성, 신축성, 생체적합성 등을 위시한 여러 PDMS 의 유용한 재료적 성질과 마이크로칩 상에 구현된 이온트로닉 소자를 성공적으로 융합하였으며, 생물학적 시스템과 연계되는 여러 관련 분야들에 있어 수많은 가능성과 영감을 만들어낼 수 있는 새로운 기회를 제시하였다.

주요어: 푸리에 변환 전기화학 임피던스 분광법 (FT-EIS), 인듐-주석 산화물 (ITO), 화학적 식각, 이온트로닉스, 하이드로젤, 이온 회로, 역전기투석, 생체모방형 정보 처리

학번: 2014-22416